Universidad Autónoma de Madrid (UAM)
Departamento de Física Teórica

Energy Reconstruction in the ATLAS Electromagnetic End-Cap Calorimeter with Calibration Hits

PhD Candidate: Eduardo Nebot del Busto
Supervisor: Dr. Jose Del Peso Malagón

Contents

Agradecimientos

Me gustaria aprovechar esta oportunidad para dar mi mas sincero agradecimiento a todas las personas que me han estado apoyando durante mi formación.

En primer lugar quiero agradecer a Jose del Peso por haberme acogido como su estudiante y por todo el conocimiento que me ha permitido adquirir el estar bajo su supervisión. El trabajo que se presenta aqui, asi como muchas otras tareas, no hubiesen sido posibles sin su orientacion, comentarios y entusiasmo por mejorar.

Mi presencia en el grupo de altas energías se la debo también a Fernando Barreiro. Le quiero agradecer el interés que ha mostrado tanto por mi trabajo, en el que ha contribuido compartiendo sus conocimientos, como por mi bienestar en todo momento.

A Luis Labarga, primera persona que conocí en la Universidad Autónoma, le tengo que agradecer su acogida y el tiempo que me ha dedicado siempre que he solicitado su ayuda.

No quiero olvidarme de agracer al resto del grupo: Juanjo, Juan, Claudia, Mara, Theodota, Luis Fernando, Pablo y Pachi, que siempre estan dispuestos a echar una mano en lo que se necesite. Y a los que se marcharon: Matti y Conchi.

A Carolina, que ha sido compañera de licenciatura, de doctorado y con la que he estado trabajando codo con codo durante los dos últimos años. Ella siempre ha estado ahí para mi y se que segirá estando si la necesito.

Y a los nuevos amigos, *the Geneva family*. En epecial Louise, que ha sido quien mas me ha empujado en los momento finales y con la que voy a poder discutir durante muchos años sobre cual es el mejor calorímetro de argón líquido.

Dejo para el final lo que pienso ha sido mas importante en mi formación como físico y como persona, mis padres. Ellos siempre han estado a mi lado e incluso ahora, separados por unos cuantos miles de kilómetros, todavía siento su apoyo como si estuviesen conmigo. Nunca estaré lo suficientemente agradecido a mis padres por haber tenido una vida de sacrificio para que yo haya podido llegar hasta aquí.

Introducción

El LHC (Large Hadron Collider) es el colisionador hadrónico mas potente conocido hasta la fecha y produjo sus primeras colisiones durante los meses de Noviembre y Diciembre de 2009. La alta energía en el centro de masas, la alta luminosidad y ciertos procesos físicos esperados en las colisiones protónicas del LHC imponen una serie de requerimientos en el funcionamiento del detector ATLAS, en particular en su calorímetro electromagnético. El calorímetro electromagnético de argón líquido de ATLAS es utilizado para la medida de energía y posición de electrones y fotones. Este deispositivo es de vital importancia en ATLAS ya que la mayoría de los procesos físicos provenientes de colisiones protón-protón en el LHC se manifiestan como estados finales fotónicos y electrónicos. Este trabajo de tesis se concentra en la parte end-cap del calorímetro de ATLAS (EMEC). Dicho subdetector ha sido instalado y puesto a punto en la caverna de ATLAS desde verano de 2006. Antes de su instalación, la respuesta de un cierto número de módulos del calorímetro (3 módulos de los 16 que forman el EMEC) fue comprobada empleando electrones de energía conocida.

Sin embargo, la situación del EMEC en las condiciones nominales de ATLAS es muy diferente a las que se dieron en los test con haces. Particulas provenientes del punto de interacción pasan a través de cables, tarjetas de lectura, criostatos, etc antes de alcanzar el calorímetro. Ademas, si dichas particulas son cargadas, interactuan con el campo magnetico central viendose su trayectoria modificada. Todas estos efectos condicionan la reconstrucción de la energía haciendo que el funcionamiento del calorímetro se degrade respecto a lo observado en tests con haces.

Un nuevo método para la reconstrucción de la energía fue ideado para el análisis de test con haces e inmediatamente despues se aplicó a la parte barrel del calorímetro EMB. El autor de esta tesis ha adaptado y testeado dicho método de reconstrucción en el EMEC, implementando nuevas técnicas para tener en cuenta las peculiaridades de este detector.

El método calibration hits recibe su nombre de una simulación Monte Carlo específica en la que se almacena la información de los depósitos de energía tanto en las partes activas como pasivas del calorímetro, asi como en el material muerto. Esto permite establecer correlaciones entre cantidades medibles (energía en presampler y en los tres compartimentos del calorímetro, baricentro en ángulo polar y baricentro en profundidad) y las perdidas de energía en el propio calorímetro así como delante y detrás del mismo.

En el capítulo 2 se da una breve descripción del modelo estandar de la física de partículas. Unicamente los aspectros estrictamente necesarios para la comprensión del posterior trabajo son tratados en cierto detalle. Capítulo 3 es un resumen de las principales características del LHC así como de los principales componentes del detector ATLAS. Capítulo 4 describe las interacciones de partículas cargadas y fotones con la materia, prestando atención a la escala de energías en la que cada uno de los procesos es dominante. Particularizando al caso de altas energías se introducen los principios de calorimetría electromagnética. Capítulo 5 describe en detalle las caracteristicas del EMEC relevantes para este trabajo de tesis. Capítulo 6 detalla el método para la reconstrucción de la energía desarrollado en esta tesis mientras que el capítulo 7 muestra los resultados obtenidos al aplicar dicho método sobre muestras de electrones y fotones aislados. Finalemte, el capítulo 8 muestra los resultados obtenidos al aplicar el método Calibration Hits sobre sucesos $pp \rightarrow Z/\gamma \rightarrow e^+e^-$.

Chapter 1

Introduction

The Large Hadron Collider, the most powerfull proton-proton collider existing so far, produced its first collisions during the months of November and December of 2009 and it is currently starting its first year of running.

The high center of mass energy, high luminosity and several physic channels present at the LHC put a set of requirements in the expected performance of the ATLAS detector.

The Liquid Argon Electromagnetic End-cap Calorimeter (EMEC), which is basically used to identify and measure the energy and direction of electrons and photons, will be very important on the LHC since many of the physic events have electrons and photons in their final states. The LAr Calorimeter has been mounted and commissioned since 2006 in the ATLAS cavern and some problems have been encountered and solved already. Furthermore, previous tests with electron beams of known energy showed that the different calorimeter requirements were fulfilled for the few modules tested (3 out of 16 modules for the EMEC). However, the nominal ATLAS set-up it is different compared to the one at the beam tests. Electrons and photons coming from the interaction point will go through the inner detector, cables, boards, cryostat walls, etc, before reaching the electromagnetic calorimeter. In addition, they will feel the effect of a 2 Tesla magnetic field, which may bend the trayectory, specially of the low energetic electrons, making miss the calorimeter cell cluster. These conditions in ATLAS will affect the energy reconstructed in the calorimeter for incident electrons and photons as well as the energy resolution with respect to the Beam Tests. The correction for this energy loss was done in the past using some weighting procedure in the different calorimeter compartments. It was shown that this procedure was not satisfactory to reconstruct the energy at the level required for particles of low energy.

A new method to reconstruct the energy of electrons and photons, called Calibration Hits Method (CHM), was devised almost four years ago and has been developed and tested for the Electromagnetic Barrel calorimeter (EMB) thereafter [32]. Simultaneously, the author of this thesis has adapted and tested the method for the Electromagnetic End-Cap Calorimeter (EMEC) and perform some further developments to the method demanded by some peculiarities of the EMEC.

The Calibration Hits Method is named after a special Monte Carlo simulation which records not only the energy depositions in the active parts of the calorimeter

but also in the inactive parts and death materials. This allows to compute correction functions for all the different sources of energy loss independently. The parameters of these functions depend on the following measurable quantities: the energies deposited in the 3 calorimeter compartments and in the presampler, and both the barycenter in depth and along the direction of the polar angle.

Chapter 2 will give and overview of the LHC and ATLAS detector. Chapter 3 gives a very brief introduction of the Standard Model of particle physics going into some detail only in a few concepts necessary for the understanding of this work. Chapter 4 introduces the basics of electromagnetic calorimetry paying special attention to sampling calorimeters. In Chapter 5 a description of the Endcap electromagnetic Calorimeter is given, with emphasis in the topics of interest for this thesis. In Chapter 6 a description of the Calibration Hits method and the work to obtain the different corrections is presented. Chapter 7 presents the achieved results by the method in terms of energy resolution, energy scale and linearity. The last chapter tries to study the effect of the CHM on electrons coming from Z decays.

Chapter 2

Theoretical background

In this chapter, the theoretical aspects of the Standard Model (SM) of particle physics which will be used in the following chapters are explained in some detail. The chapter begins with a general description of the SM. A few more details about the electroweak theory and the Z boson production at hadron colliders are described.

2.1 The Standard Model

The Standard Model [1] of particle physics is the theory that describes the interaction between elementary particles. It is a quantum field theory based in a gauge symmetry $SU_C(3) \otimes SU_L(2) \otimes U_Y(1)$. The symmetry group $SU_C(3)$ describes the strong interactions, and $SU_L(2) \otimes U_Y(1)$ describes the electroweak interactions.

The type of elementary particles entering the Standard Model may be classified in two groups, namely: bosons which transmit the force and fermions which make matter: Fermions are classified as quarks and leptons depending on wether or not they experience the strong interaction. The known leptons are the electron e^-, the muon μ^- and the tau τ^- all of them carrying charge $Q = -1$ (charge is given in units of the electron charge) and the corresponding chargeless neutrinos ν_e, ν_μ and ν_τ. Leptons undergo the electroweak interaction, which decreases strongly with the distance. Quarks are classified into six flavours: u, c and t with charge $Q = -2/3$ and d, s and b with charge $Q = 1/3$. The quarks have an extra quantum number, the colour, which is the charge asociated with the strong interaction. The nature of the strong interactions is such that quarks are not found as isolated particles, but they combine in colourless combinations called hadrons. These colourless combinations are classified as mesons (fermions made of pairs quark-anty quark $q\bar{q}$) and barions (fermions made of a group of three quarks qqq).

The fermion component of the SM is listed in table 2.1. Leptons, as well as quarks, are arranged in three generations of particles formed by particles with the same characteristics except for their masses. Hence, particles from the second and third generation are unstable and decay to particles from the first generation, which form ordinary matter.

[1] For more details on the Standard Model see for instance [1]

Family	Quark	M (GeV)	Q (q_e)	Leptons	M (GeV)	Q (q_e)
1	d	0.003-0.007	$-1/3$	e	$0.51099892 \pm 0.00000004$	-1
	u	0.0015-0.0030	$+2/3$	ν_e	< 0.002	0
2	s	0.095 ± 0.025	$-1/3$	μ	105.658369 ± 0.000009	-1
	c	1.25 ± 0.09	$+2/3$	ν_μ	< 0.19	0
3	b	4.20 ± 0.07	$-1/3$	τ	1776.99 ± 0.28	-1
	t	174.2 ± 3.3	$+2/3$	ν_τ	< 18.2	0

Table 2.1: *Fermionic component of the standard model*

Being the SM based on a gauge symmetry, the interactions are mediated by vector bosons. The interaction will have as many "boson interaction carriers" as generators has the symmetry group is based on. Hence, the strong interaction has 8, called gluons, and the electronweak interaction has 4 ($\gamma, Z, W^{\pm}$).

The last piece of the SM is a scalar field that generates the particle' masses, via The Higgs mechanism. The measurements related to the W and Z bosons to date are in agreement with the higgs mechanism. However, the spin 0 particle arising from such mechanism has yet to be observed.

2.2 Quatum chromodynamics

Quantum ChromoDynamics (QCD) is the theory that describes strong interactions within the SM and it is based on the lagrangian;

$$\mathcal{L}_{QCD} = -\frac{1}{4} F^i_{\mu\nu} F^{i\mu\nu} + \sum_r i\bar{\Psi}_r \gamma_\mu D^\mu \Psi_r \tag{2.1}$$

The first part of the equation describes the dynamics of the gluons where

$$F^i_{\mu\nu} = \partial_\mu G^i_{nu} - \partial_\nu G^i_\mu - g_s f_{ijk} \lambda^k$$

is the gluonic tensor, g_s the strong the gauge coupling constant and f_{ijk} are the structure constant, arising from the relation between the SU(3) generators

$$[\lambda_i, \lambda_j] = 2i f_{ijk} \lambda^k \;\; i, j, k = 1, ..., 8$$

The second part of the equation describe the interaction between quarks by interchanging gluons. The fields Ψ represents a colour triplet and D_{mu} represents the covariant derivative:

$$D_\mu = \partial_\mu + i g_s \sum_{i=1}^{8} \lambda_i G_i$$

which is introduced in order to make the theory invariant under the SU(3) transformation:

$$\Psi \rightarrow exp(-ig_s \sum_{i=1}^{8} \lambda_i \theta_i(x))\Psi$$

with $\Theta_i(x)$ arbitrary functions of space time.

2.3 Electroweak theory

The electroweak interactions are based on a $SU_Y(2) \otimes U_Y(1)$ symmetry described in the lagrangian:

$$\mathcal{L}_{EW} = \mathcal{L}_{gauge} + \mathcal{L}_{Higgs} + \mathcal{L}_f + \mathcal{L}_{Yuk} \tag{2.2}$$

The gauge part of the lagrangian characterizes the dynamics of the gauge bosons and it is given by:

$$\mathcal{L}_{gauge} = -\frac{1}{4} W^i_{\mu\nu} W^{i\mu\nu} - \frac{1}{4} B_{\mu\nu} B^{\mu\nu} \tag{2.3}$$

the two different terms account for the three fields associated with the $SU_L(2)$ (W^i with $i = 1, 2, 3$) and $U_Y(1)$ (B) respectively and they can be written as:

$$W^i_{\mu\nu} = \partial_\mu W^i_\nu - \partial_\nu W^i_\mu - g\epsilon_{ijk} W^i_\mu W^i_\nu$$

$$B_{\mu\nu} = \partial_\mu B_\nu - \partial_\nu B_\mu$$

The coupling constants g' and g are associated with hypercharge and Isospin and ϵ_{ijk} are the structure constants of the $SU(2)$ group:

$$[\sigma_i, \sigma_j] = 2i\epsilon_{ijk}\sigma_k$$

with σ_i the Pauli matrices.

The fermionic part of the lagrangian is given by:

$$\mathcal{L}_f = i\Psi^\dagger_L \gamma^\mu \mathcal{D}_{\mu L} \Psi_L + ii\Psi^\dagger_R \gamma^\mu \mathcal{D}_{\mu R} \Psi_R \tag{2.4}$$

where $\Psi_{L(R)} = (1 \mp \gamma^5)\Psi/2$ are the lefr (right) chiral projections of the fermion and γ_μ the Dirac matrices. The left handed fermions are $SU_L(2)$ doublets and they are represented by:

$$\Psi = \begin{pmatrix} \nu_{eL} \\ e_L \end{pmatrix}, \begin{pmatrix} u_L \\ d_L \end{pmatrix}$$

whereas the right projections e_R, u_R and d_R are $U_Y(1)$ singlets. Hence, the covariant derivatives act differently over the right and left handed fermions:

$$\mathcal{D}_{\mu L} = \partial_\mu + i\frac{g'}{2} Y B_\mu + ig\vec{\sigma}\vec{W}_\mu$$

$$\mathcal{D}_{\mu R} = \partial_\mu + i\frac{g'}{2} Y B_\mu$$

Symmetry breaking

Whereas the boson B_μ could be responsible for the electromagnetic interactions, the three bosons $\vec{W}_\mu$ can not explain the weak force since they are massless and including a mass term in the lagrangian breaks the $SU(2) \otimes U(1)$ symmetry. The solution [2, 3, 4] is found by including a $SU(2)$ doublet scalar field:

$$\Phi = \begin{pmatrix} \frac{1}{\sqrt{2}}(\Phi_1(x) + i\Phi_2(x)) \\ \frac{1}{\sqrt{2}}(\Phi_3(x) + i\Phi_4(x)) \end{pmatrix}$$

This field is included in the lagrangian with a quartic term:

$$\mathcal{L}_{Higgs} = \mathcal{D}_{L\mu}\Phi^\dagger\mathcal{D}_L - V(\Phi^\dagger\Phi) = \mathcal{D}_{L\mu}\Phi^\dagger\mathcal{D}_L - \mu^2\Phi^\dagger\Phi - \lambda(\Phi^\dagger\Phi)^2 \tag{2.5}$$

For $\mu^2 > 0$ and $\lambda < 0$ the minimum of the potential $\Phi^\dagger\Phi = -\mu^2/2\lambda$ is degenerated. This gives rise to four Goldstone bosons, three of which can be eliminated by a suitable choice of the gauge. The remaining Goldstone boson is the Higgs field $H(x)$. Now, the Φ fiels may be rewritten as:

$$\Phi = \begin{pmatrix} 0 \\ \frac{1}{\sqrt{2}}(v + H) \end{pmatrix} \tag{2.6}$$

with $v = \sqrt{-\mu^2/2\lambda}$. Substituting equation 2.7 in equation 2.5 and using the covariant derivatives we obtain:

$$\begin{aligned} \mathcal{L}_{Higgs} = \tfrac{1}{2}\begin{pmatrix} 0 & v \end{pmatrix}\left[\tfrac{g}{2}\vec{\sigma}\vec{W}_\mu + \tfrac{g'}{2}B_\mu\right]^2\begin{pmatrix} 0 \\ v \end{pmatrix} + H\ terms \\ \rightarrow M_W^2 W^{+\mu}W_\mu^- + \tfrac{M_Z^2}{2}Z_\mu Z^\mu + H\ tems \end{aligned} \tag{2.7}$$

with

$$W^\pm = \frac{1}{\sqrt{2}}(W^1 \mp iW^2)$$

$$Z = -sin\theta_W B + cos\theta_W W^3$$

and the photon field

$$A = cos\theta_W B + sin\theta_W W^3$$

remaining massless. The angle θ_W, such that $tan\theta_W = g'/g$ accounts for the mixing between W^3 and B. Finally, the coupling to the physical bosons $W^\pm$, Z and γ to fermions can be obtained by substituting the above equations in 2.4. The bosons $W^\pm$, like $W^{1,2}$ only couple to left handed fermions with coupling constant g related to the Fermi constant by:

$$\frac{G_F}{\sqrt{2}} = \frac{g^2}{8M_W^2}$$

The experimentally determined values of the main electroweak parameters are shown in table 2.3.

Quantity	Value
M_Z	$(91.1876 \pm 0.0021)\ GeV$
M_W	$(80.398 \pm 0.005)\ GeV$
$sin^2\theta_W$	(0.23119 ± 0.00014)
$G_F/(\hbar c^3)$	$(1.16637 \pm 0.00001) \times 10^{-5}\ GeV^{-2}$

Table 2.2: *Experimental measurements [5] ot the main electroweak parameters*

The photon couples to both letf and right handed fermions with a coupling constant e well known from QED and related to the couplings g and g' by :

$$e = gsin\theta_W = g'con\theta_W$$

The Z also couples to both Fermionic chiral projections but with different strength C_z related to the electric charge and third component of the isospin by:

$$c_Z = I_3 - Q \cdot sin^2\theta_W$$

the charge and isospin values for fermion of the first generation are listed in table 2.3.

Particle	Q (e)	I_3	c_Z
ν_L	0	1/2	1/2
e_L	-1	-1/2	$-1/2 - sin^2\theta_W$
e_R	-1	0	$-sin^2\theta_W$
u_L	2/3	1/2	$-1/2 + 2/3\ sin^2\theta_W$
u_R	2/3	0	$-2/3\ sin^2\theta_W$
d_L	-1/3	-1/2	$-1/2 + 1/3\ sin^2\theta_W$
d_R	-1/3	0	$1/3\ sin^2\theta_W$

Table 2.3: *Coupling of the fermions to photon, W and Z as defined in the text.*

2.4 Vector Boson production at the LHC

In high energy hadron colliders, such as the LHC , Z bosons on the mass shell may be produced, being the dominant productionprocess the Drell-Yan [6]:

$$q\bar{q} \rightarrow Z/\gamma^* \rightarrow f\bar{f}$$

The cross section at the partonic level can be calculated via the electroweak theory and is given by [5]:

$$\begin{aligned}\sigma_{q\bar{q}\to ee} &= \sigma_\gamma + \sigma_{\gamma/Z} + \sigma_Z = \\ &= \frac{4\pi\alpha^2}{3s}\cdot Q^2 N_c \\ &- \frac{2\sqrt{2}\alpha}{3}\cdot Q_q G_F N_C c_Z^e c_Z^q \cdot \frac{(s-M_Z^2)M_Z^2}{(s-M_Z^2)^2 + s^2\Gamma_Z^2/M_Z^2} \\ &+ \frac{12\pi}{M_Z^2}\cdot\frac{\Gamma(ee)\Gamma(f\bar{f})}{\Gamma_Z^2}\cdot\frac{s\Gamma_Z^2}{(s-M_Z^2)^2 + s^2\Gamma_Z^2/M_Z^2}\end{aligned} \tag{2.8}$$

where Q is the charge of the quark $N_c = 3$ is the number of colours and $c_Z = c_Z^R + c_Z^L$ is de sum of the couplings of the two chiral projections of the fermion to the Z boson defined in the previous section. For values of s around M_Z^2 the photon term is negligible.

Note that the interference between the Z boson and the off-shell γ is a consequence of the mixing between the electroweak bosons W^3 and B to form γ and Z. In proton-proton collisions the Drell Yan is possible at the partonic level. In the parton model, the proton contains not only the valence quarks (u, u, d) but also a parton "sea" formed of quarks, antiquarks and gluons carrying only a small fraction of the proton momentum. In order to estimate the fraction of the momentum carried by partons at the LHC lets consider the center of mass energy $\sqrt{s}$. The energy available for collisions will be, if the two partons are carrying a fraction x_1 and x_2 of the proton momentum:

$$s_{AV} = x_1 x_2 s$$

For a real Z production, $s_{AV} \sim M_Z^2$. Hence, the fraction of momentum carried by partons at the LHC is typically $M_Z/14\ TeV \sim 6.5 \cdot 10^{-3}$.

However, in order to compute the Z production cross section at proton-proton collisions we must consider the probability of finding a quark or antiquark with momentum fraction x, which is described by the Parton Density Functions (PDFs) $f_q(x, \mu_F)$. These depend on an energy scale (μ_F, the factorisation scale) with a value not fixed by the theory although usually chosen to be near a characteristic energy momentum . A parameterization of the PDFs provided by the CTEQ collaboration is shown in figure 2.1. The valence quark (u, d) contribution can be noticed as a small peak around $x \sim 0.1$. However, at x values relevant for Z production the "sea" dominates. Although the gluon contribution is substantially larger, it does not contribute to the Drell-Yan process until higher order QCD corrections.

Once a parameterization of the PDFs is determined $pp \to Z/\gamma \to ee$ cross section can be computed as:

$$\sigma_{pp\to Z/\gamma\to ee}(s) = \sum_i \sum_j \int\int dx_i dx_j f(x_i, \mu_R) f(x_j, \mu_R) \sigma_{q\bar{q}\to Z/\gamma\to ee}(x_i, x_j, s) \tag{2.9}$$

where i, j run over all possible flavours of the incoming partons.

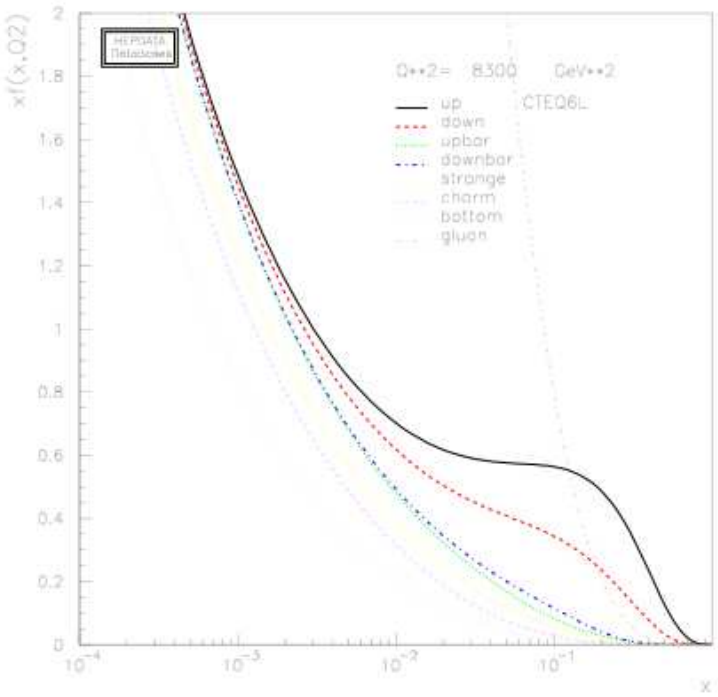

Figure 2.1: Proton PDFs versus x at $\mu_F = M_Z$. Figure is taking from [7]

Chapter 3

The ATLAS detector

In this chapter the motivation and the main characteristics of the Large Hadron Collider (LHC) as well as the ATLAS detector are discussed. In the first section the most important accelerator parameters are reviewed. In the second section a brief overview of the ATLAS detector is presented.

3.1 The Large Hadron Collider

The LHC [8, 9] is a proton-proton collider capable of accelerating protons up to 7 TeV and lead ions up to 2.8 TeV per nucleon. The accelerator, being mounted in the $\sim$ 27 km circular tunnel previously hosting LEP, is currently operating and it did produce its first proton-proton collisions at energy of center of mass 2.6 TeV during November and December of 2009.

The LHC was designed to reach a center of mass energy and luminosity that maximizes the potential for discovering new physics. Achieving beam energies of 7 TeV requires a large magnetic field to bend the protons around the LHC beam. Such magnetic field (8.4 T) is provided by 1232 superconducting dipoles cooled with liquid helium at 1.9 K. The luminosity $\mathcal{L}$ is a function of the beam shape and the currents circulation on the magnets and determines the expected number of events produced for a process with a given cross section σ by:

$$N = \sigma \int \mathcal{L} dt = \sigma L$$

with L the so-called integrated luminosity. The LHC is expected to operate at a luminosity of $2 \times 10^{33} cm^{-2} s^{-1}$ in its first stages which will be increased afterwards to its nominal value of $10^{34} cm^{-2} s^{-1}$ equivalent to an integrated luminosity of 100 fb^{-1} a year.

Bunches of protons separated by $25ns$ will intersect at the four interaction points where the four different detectors are placed. The ATLAS detector, described in subsequent section, is a general purpose detector designed with a large sensitivity to the processes that may occur at the LHC. In addition to ATLAS, other three major experiments are hosted by the LHC. The CMS experiment [10] is the most similar

to ATLAS being a general purpose experiment as well. The presence of these two experiments doubles the number of recorded event and allow to both experiments, having different technologies, to cross check each other. LHCb [11] is a fixed target experiment designed to precisely measure the properties of B mesons in order to better understand quark flavour mixing. Finally, ALICE [12] is optimized for heavy ion collisions, to investigate complex strongly interacting systems and the quark gluon plasma. The positions of all four experiments along the LHC is presented in figure (3.1).

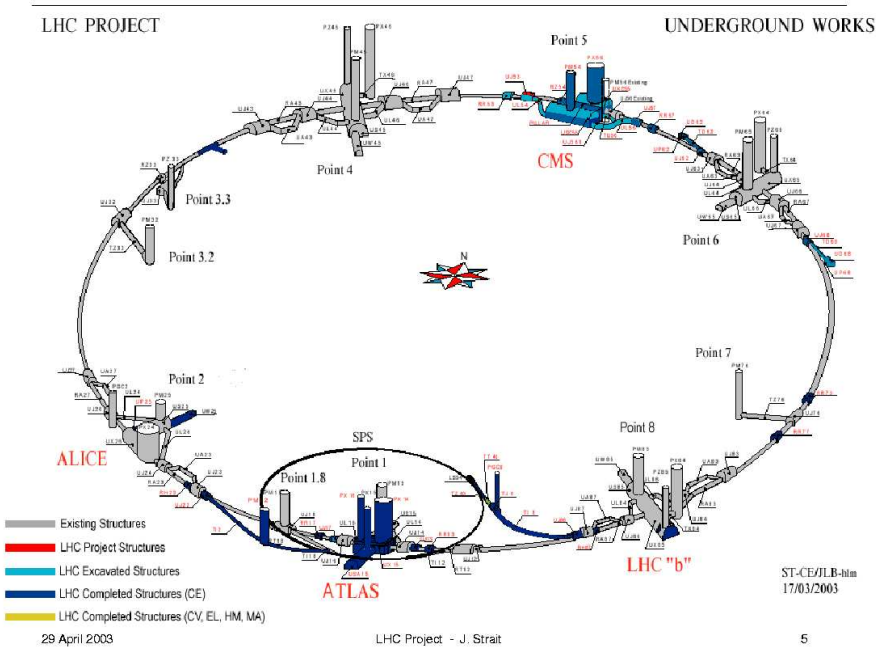

Figure 3.1: Diagram of LHC ring.

In addition, the LHC hosts two smaller experiments (LHCf [13] and TOTEM [14]), which provide complementary physics measurement in the forward regions, using the same collisions as the general purpose experiments.

The design of the LHC makes it possible to explore an unprecedented physical region, where new physics phenomena may appear.

3.2 The ATLAS detector

The ATLAS (A ToroidaL ApparatuS) is a multi-purpose detector designed to exploit the physics potential of the LHC. The detector, figure 3.2, is a cylinder 44 meter long, 12.5 meters radius and an overall weight of 7000 tons [15].

The ATLAS detector is nominally forward-backward symmetric with respect to the interaction point, which is defined as the origin of the coordinate system. The beam lines defines the z axis whereas the $x - y$ plane is perpendicular to it. The positive direction of the x axis is defined as pointing from the interaction point to

the LHC center while the positive y direction is chosen to be pointing upwards. The azimuth angle ϕ is measured around the beam axis and the polar angle θ is the angle from the beam axis. Variations in the polar direction are typically measured in terms of the pseudo-rapidity defined as:

$$\eta = -ln(tan\left(\frac{\theta}{2}\right))$$

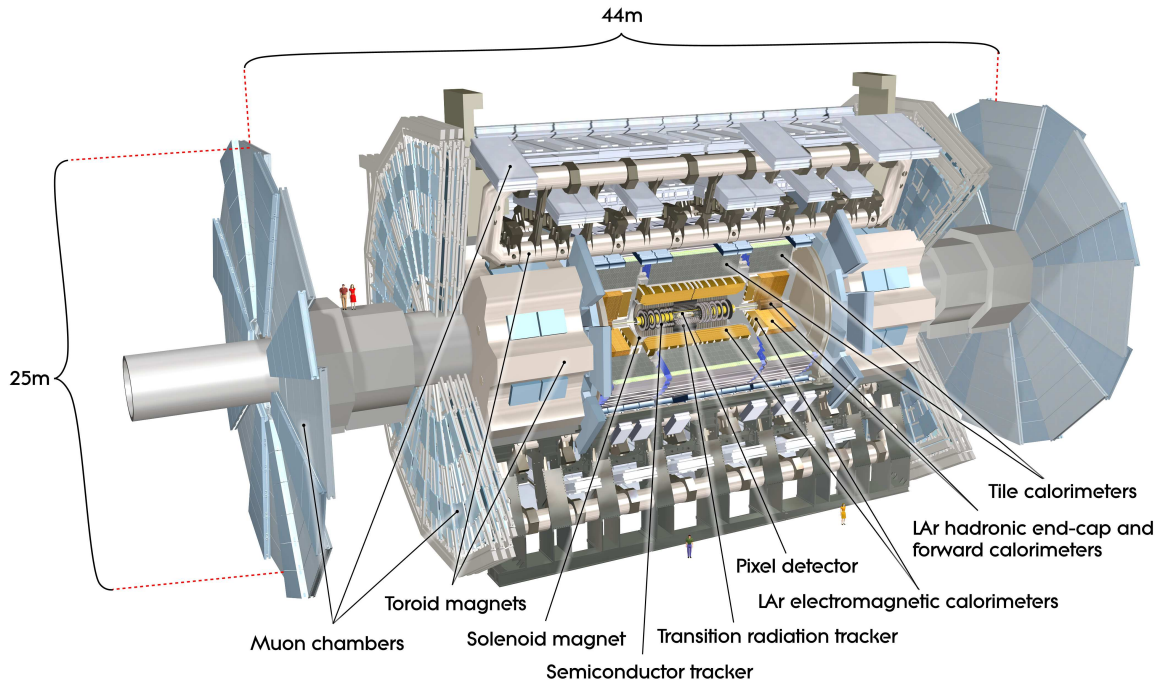

Figure 3.2: View of the atlas detector.

3.2.1 Physics requirements

The LHC will provide a large variety of physics studies ranging from Standard Model precision measurements to discovery of new physics phenomena. Requirements on the performance of the ATLAS subsystems have been defined using a set of processes expected to be seen, namely:

- High luminosity and production cross section at LHC energies will allow high precision test of QCD, electroweak interactions and flavour physics. A large number of top quarks will be produce , providing the opportunity to measure its coupling and spin.

- Search for Standard Model Higgs impose tight constrains in EM calorimetry. For a low mass higgs ($M_H < 2M_Z$) its natural width is predicted to be of the order of a few MeV, and hence dominated by instrumental resolution.

- New heavy gauge bosons will be accessible for masses of the order of a few TeV. Hence, high resolution and charge identification are needed at the TeV scale.

- Events predicted by supersymmetric models, or theories predicting particles escaping in extra dimension will produce large amounts of missing transverse momentum.

The nominal conditions of the LHC and the nature of these benchmark channels reflect in a set of requirements for the ATLAS detector:

- Radiation-hard and fast electronics and sensor elements.

- High detector granularity in order to handle large particle fluxes and avoid as much as possible the overlap of events.

- Large acceptance in pseudo-rapidity and hermeticity (full ϕ coverage).

- Good charge and particle momentum resolution and reconstruction efficiency in the inner detector with vertex detectors close to the interaction point for τ-lepton and b-jet tagging.

- Good muon identification and momentum resolution from a few GeV up to a few TeV.

- High efficiency triggering low transverse momentum objects with good background rejection.

The main performance goals for the different ATLAS subsystems are summarized in table 3.1.

Detector	Required resolution	η coverage
Tracking	$\sigma/p_t = 0.05\% p_t \oplus 1\%$	± 2.5
EM Calo	$\sigma/E = 10\%\sqrt{E} \oplus 0.7\%$	± 3.2
Had Calo	$\sigma/E = 50\%\sqrt{E} \oplus 3\%$	± 3.2
Forward Calo	$\sigma/E = 100\%\sqrt{E} \oplus 10\%$	$3.1 < \lvert\eta\rvert < 4.9$
Muon spectr	$\sigma/p_t = 10\%$ at 1 TeV	± 2.7

Table 3.1: *Performance goals for the different ATLAS subsystems.*

3.2.2 Tracking

The Inner detector (ID) is a tracking detector located in the most inner part of ATLAS, which is enclosed within a cylinder that has a length of $76.2m$ and a radius of $1.05m$ (see figure 3.3). It is designed to measure the trajectory (track) of charged particles with a very good efficiency in the coverage range $-2.5 < \eta < 2.5$. It is immersed in an axial magnetic field of 2 T for the measurement of the momentum of charged particles. It consists, from inner to outer volume, of three parts: two types of Silicon semiconductor (Pixel and SCT) and straw-tube tracking detectors (TRT). The combination of Pixel and SCT allows for the reconstruction of particle decay length for unstable particles, while the TRT implements an identification of electrons through the transition radiation effect.

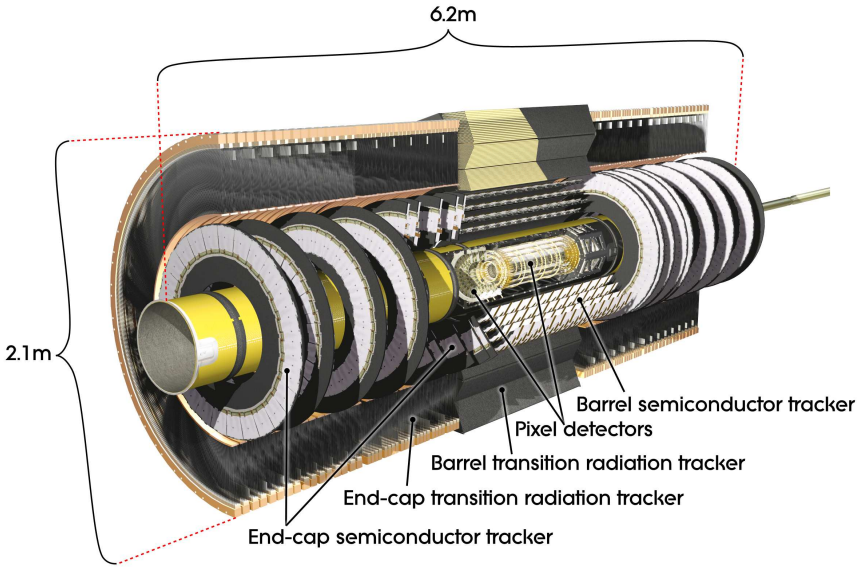

Figure 3.3: View of the Inner detector.

The pixel and SCT sub-detectors cover the region $|\eta| < 2.5$ and they are arranged on concentric cylinders around the beam axis in the barrel region, while they are located on discs perpendicular to the beam axis in the end-cap regions. A large number of hits is provided by straw tubes which provide coverage up to $|\eta| = 2.0$. In the barrel region, the straws are parallel to the beam axis whereas in the end-caps they are arranged radially in wheels.

3.2.3 Calorimeter

Figure 3.4. shows a schematic view of the different ATLAS calorimeters. These calorimeters cover the range $|\eta| < 4.9$ using various techniques depending on the physics process of interest and the differences on the radiation environment over η. The different calorimeters may be classified as electromagnetic and hadronic.

The Electromagnetic (EM) Calorimeter is used to identify electrons and photons, and to measure their energy and direction. It is also part of the hadronic calorimeter

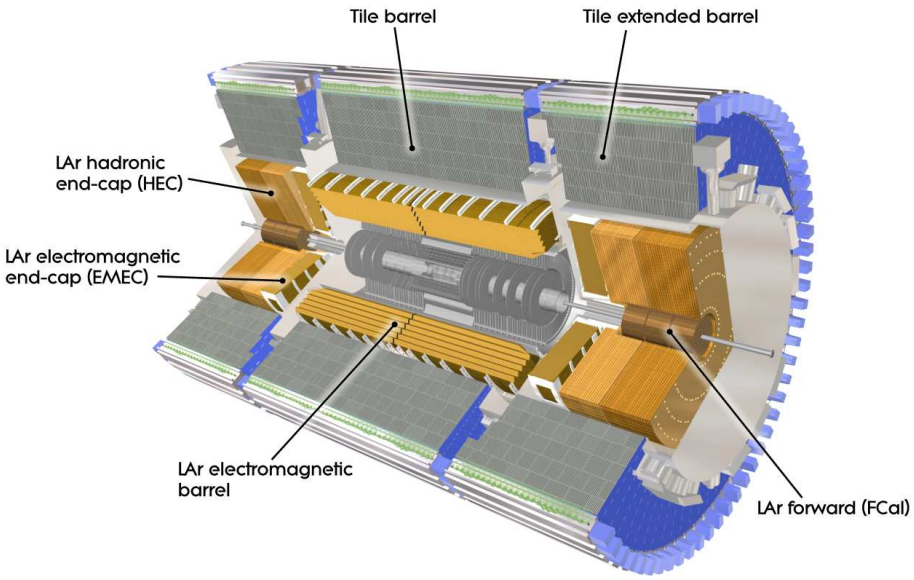

Figure 3.4: Schematic view of the ATLAS calorimeters.

when measuring the energy of jets and the missing transverse energy (E_T^{miss}) of some processes. The EM calorimeter is a lead - liquid Argon sampling calorimeter with fine granular cells, which covers a pseudo-rapidity range $-3.2 < \eta < 3.2$ and the whole range along the azimuthal (ϕ) direction. It is divided in one barrel ($-1.475 < \eta < 1.475$) and two end-caps ($-3.2 < \eta < -1.375$, $1.375 < \eta < 3.2$) [16]. The ElectroMagnetic Endcap Calorimeter (EMEC) is a fundamental part of this thesis work and it is largely described in chapter 5.

The Hadronic calorimeter is also sub-divided in three subsystems:

- The Tile Calorimeter is a sampling calorimeter with steal as passive material and scintillating tiles as active material. It is placed directly outside the EM calorimeter and it is formed by a barrel covering $|\eta| < 1.0$ and two extended barrels covering $0.8 < |\eta| < 1.7$.

- The Hadronic Endcap Calorimeter (HEC) is a sampling calorimeter using Liquid argon as active material and copper as absorber. It is composed by two independent wheels placed directly behind the EMEC wheels and hosted in the same cryostat. The HEC cover the region $1.5 < |\eta| < 3.2$.

- The forward calorimeter is realized to achieve a good hermeticity in ATLAS, hence to provide an excellent resolution in the measurement of missing transverse energy. It covers the region in pseudo-rapidity $-4.9 < \eta < -3.2$ and $3.2 < \eta < 4.9$. It is a sampling calorimeter, with liquid Argon as sensitive material, segmented longitudinally in three compartments: FCAL1, FCAL2 and FCAL3. As absorber material the first one uses copper while the last two use tungsten inside copper tubes.

3.2.4 Muon Spectrometer

The muon spectrometer, figure 3.5 is a tracking detector for precise measurements of muon trajectory and transverse momentum and it is based on the magnetic deflection of muon tracks in the large superconducting air-core toroid magnets. For $|\eta| < 1.4$ the magnetic field is provided by the large barrel toroid whereas for $1.6 < |\eta| < 2.7$ tracks are curved by two end-cap magnets inserted at the the end of the barrel toroid.

Muon tracks a measured by using gas proportional chambers which surrounds the calorimeter. There two types of chambers: MDT in the barrel location (arranged in three layers around the beam axis) and CSC in the End-Caps (arranged in three layers perpendicular to the beam). Additionally there are fast response chambers to trigger on muons, which are called RPC in the barrel region and TGC in the End-Caps. Both chamber types for trigger purposes are capable of delivering the response in a short time, between 15 ns and 20 ns, shorter than the crossing time of LHC beam proton bunches. The chambers extend to the ATLAS dimensions, for the barrel part to a radius of 11 m and for the the End-Caps to a length of 23 m from the nominal interaction point.

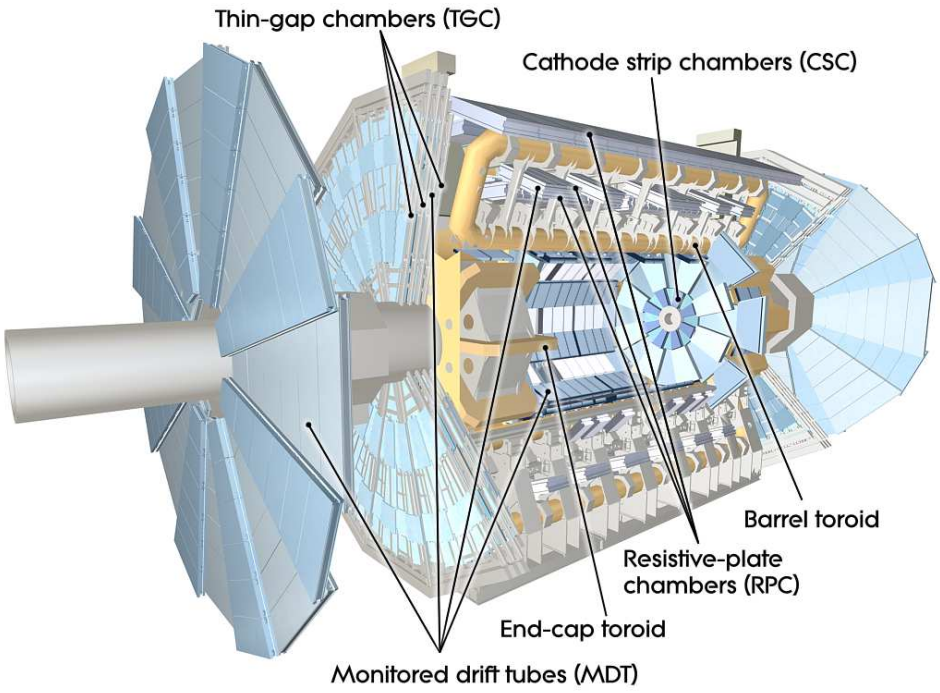

Figure 3.5: View of the muon system.

Chapter 4

Review of calorimetry

Particle detection is possible due to the interaction of these particles with matter. In this section, the different processes taking place on this interactions (with special attention to those happening at high energies) are described. Once the main interaction processes are reported, a few concepts on electromagnetic shower development and principles of calorimetry will be introduce. Finally, the primary features of sampling calorimeters will be discussed.

4.1 Interaction of charged particles with matter

Charged particles traversing a certain material will interact via electromagnetic force with the nuclei and electrons of the atoms forming the media. The incoming particle will undergo several processes, depending on the energy range, losing a fraction of its original energy. Namely:

- Ionization. The incoming particle interacts with an electronic atom in its bound initial state and transfers to it enough energy to produce a free electron.
- Bremsstrahlung. The incoming particle is decelerated by interacting with the (mostly nuclear) Coulomb field, radiating photons.

Hence, the energy loss per unit length can be written as follows:

$$\left(\frac{dE}{dx}\right)_{TOT} = \left(\frac{dE}{dx}\right)_{ion} + \left(\frac{dE}{dx}\right)_{brem} \tag{4.1}$$

As we will discuss in subsequent sections, the ionization is the dominant process at low energy whereas bremsstrahlung contributes at higher energies.

Charged particles also undergo multiple scattering processes. These processes, considering the mass of the incoming particle much lower that the nucleus mass, could be contemplated as elastic processes: the nuclei energy recoil are so small that could be neglected. Hence, multiple scattering will only affect the trajectory of the particle.

4.1.1 Energy loss by ionization

For an incoming particle of mass $M >> m_e$, charge ze and velocity v, the energy loss by unit o length was computed by Bethe and Bloch:

$$-\frac{dE}{dx} = \frac{2\pi n z^2 e^4 \rho Z N_a}{AMv^2} \cdot \left\{ ln\left(\frac{2Mv^2 W_m}{I^2(1-\beta^2)}\right) - 2\beta^2 \right\} \tag{4.2}$$

where:
E: incident energy
x: path length
N_a Avogadro's number ($6.023 \times 10^{23} mol^{-1}$)
A, Z: atomic weight and atomic number of the absorbing material
ρ: density of the absorbing material
β: v/c of the incident particle
I: mean excitation potential
$W_m = \frac{2m_e c^2 \beta^2 \gamma^2}{1+2\frac{m_e}{M}\sqrt{1+\beta^2\gamma^2}+(\frac{m_e}{M})^2}$: Maximum energy transfer to the atomic electron

In practice, two more corrections are needed, the so-called density effect and shell effect:

$$-\frac{dE}{dx} = \frac{2\pi n z^2 e^4 \rho Z N_a}{AMv^2} \cdot \left\{ ln\left(\frac{2Mv^2 W_m}{I^2(1-\beta^2)}\right) - 2\beta^2 - \delta - U \right\} \tag{4.3}$$

δ: density effect correction arises from the fact that the electric field of the particle also tends to polarize the atoms along his path.

U: Shell effect correction accounts for effects happening when the energy of the incoming particle is comparable with the energy of the atomic electrons.

As an example, dE/dx is shown in figure 4.1. For low values of energy the term $1/\beta^2$ is dominant and dE/dx strongly decreases up to a minimum at $\beta\gamma \sim 3$. Particles traveling with this energy are known as Minimum ionizating particles. Beyond the minimum, the logarithmic term dominates producing a growing behaviour of the energy-loss (relativistic raise) which will be compensated at high energy by the density effect (Fermi plateau).

Electrons and positrons

When the ionizing particles are electrons or positrons the energy-loss formula must be recomputed. In this particular case the mass of the incoming particle cannot be neglected in comparison with the atomic electron. Moreover, now we are considering spin 1/2 particles so we have to consider Fermi statistics. This simplifies the maximum transferable energy to the atomic electron $W_m = T_e/2$ with T_e the kinetic energy of the incoming electron. With this considerations the energy loss is expressed as:

$$-\frac{dE}{dx} = 2\pi N_a r_e^2 m_e c^2 \rho \frac{Z}{A}\frac{1}{\beta^2}\left\{ ln\frac{\tau^2(\tau+2)}{2(I/m_e c^2)^2} + F(\tau) - \delta - U \right\} \tag{4.4}$$

whit τ the kinetic energy of the incoming electron in units of $m_e c^2$ and

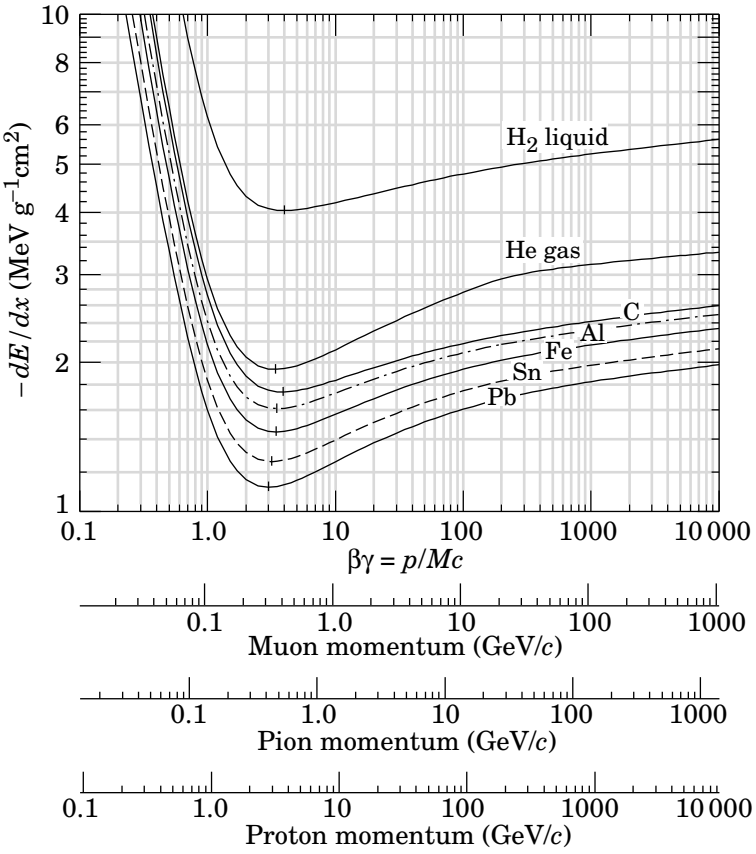

Figure 4.1: Mean energy loss by unit of length as a function of the energy of the incoming particle for muons, pions and protons in different materials. The figure was taken from [17]

$$F(\tau) = 1 - \beta^2 \frac{\tau^2/8 - (2\tau+1)ln2}{(\tau+1)^2}$$

for e^- and

$$F(\tau) = 2ln2 - \frac{\beta^2}{12}\left(23 + \frac{14}{\tau+2} + \frac{10}{(\tau+2)^2} + \frac{4}{(\tau+2)^3}\right)$$

for e^+.

4.2 Enery loss by radiation

The principal feature of Bremsstrahlung radiation, photon emission due to a coulomb scattering of an incoming charged particle with the nucleus (figure 4.2), is the dependence of its probability with m^{-2} (mass of the incident particle). This implies that radiation loss by a muon, second lightest particle, is 40000 times smaller than

for electrons. Hence, we will consider only electrons and photons in the following arguments.

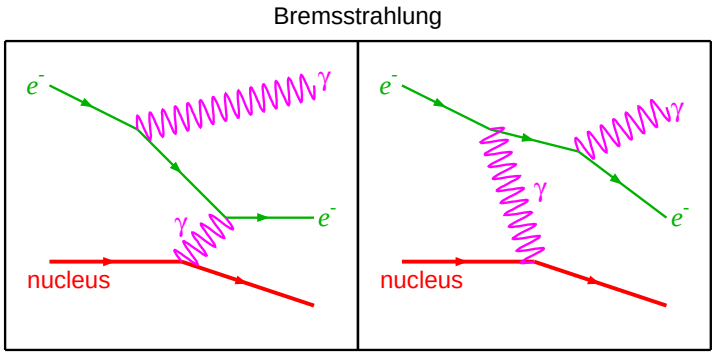

Figure 4.2: Feynman diagram for Bremsstrahlung.

Bremsstrahlung also depends on the strength of the coulomb field felt by the incoming particle and therefore, it depends on the amount of screening from the atomic electron the the nucleus. The effect of the screening can be parameterized by the quantity

$$\xi = \frac{100 m_e c^2 h\nu}{E_0 E Z^{1/3}}$$

with E_0 and E initial and final energy of the electron (positron) and $h\nu = (E_0 - E)$ energy of the radiated photon. This parameter is related to the radius of Thomas-Fermi atom and is small ($\xi \sim 0$) for total screening an large ($\xi >> 1$) for no screening. In the frame of the Born approximation and for relativistic electrons (E_0 bigger that a few MeV) the bremsstrahlung cross section is given by:

$$\frac{d\sigma}{d\nu} = \frac{4\sigma_0}{\nu}\left\{(1+\epsilon^2)\left(\frac{\phi_1(\xi)}{4} - \frac{1}{3}lnZ - f(Z)\right) - \frac{2}{3}\epsilon\left(\frac{\phi_2(\xi)}{4} - \frac{1}{3}lnZ - f(Z)\right)\right\}$$

where $\epsilon = E/E_0$, $\sigma_0 = \alpha Z^2 r_e^2$ and $\alpha = 1/137$. The function $f(Z)$ is a small correction to the Born approximation which takes into account the coulomb interaction of the outgoing electron with the field of the nucleus. It can be parameterized as:

$$f(Z) \simeq a^2\left((1+a^2)^{-1} + 0.20206 - 0.0369a^2 + 0.0083a^4 - 0.002a^6\right)$$

with $a = Z/137$. Considering only the limits of no screening and total screening the function ϕ_1 and ϕ_2 are given by:

$$\xi \to 0: \quad \phi_1(0) = \phi_2(0) + 2/3 = 4ln(183)$$

$$\xi \to \infty: \quad \phi_1(\infty) = \phi_2(\infty) = 19.19 - 4ln\xi$$

From now on we will restrict ourselves to the case of full screening ($\xi \sim 0$), This happens for high Z which is the case for calorimeters. Hence, in the full screening case the cross section for bremsstrahlung is given by:

$$\frac{d\sigma}{d\nu} = \frac{4Z^2 r_e^2 \alpha}{\nu}\left\{\left(1+\epsilon^2-\frac{2\epsilon}{3}\right)\left\{ln(183Z^{-1/3})-\frac{1}{2}-f(Z)\right\}+\frac{\epsilon}{9}\right\}$$

The energy loss can be calculated now integrating the cross section times the energy of the photon.

$$-\left(\frac{dE}{dx}\right)_{brem} = N\int_0^{\nu_0} h\nu\frac{d\sigma}{d\nu}(E_0,\nu)d\nu = N\cdot E_0\cdot\phi_{rad}$$

where N is the number of atoms per unit volume and

$$\phi_{rad} = \frac{1}{E_0}\int_0^{\nu_0} h\nu\frac{d\sigma}{d\nu}d\nu$$

Since $\frac{d\sigma}{d\nu} \sim \nu^{-1}$, the quantity ϕ_{rad} will be independent of ν and a function of the material traversed by the incoming electron. Hence the energy loss is proportional to the energy and its dependence with the path length can be writen as:

$$E = E_0 e^{-N\phi_{rad}x} = E_0 e^{-x/X_0}$$

Thus, we define the radiation length X_0 as the distance over which the electron energy has been reduced by a factor e^{-1}. Note that this quantity is exclusively dependent on the material traversed by the electron. For complex materials (compounds of several materials), the radiation lenght is computed by means of Bragg's rule:

$$\frac{1}{X_T} = \sum\frac{w_i}{X_i}$$

where w_i is the fraction by weight of each material.

Critical energy

As discussed before electrons and positrons suffer both ionization and bremsstrahlung. The former increases logarithmically with energy, whereas the latter is proportional to the incoming energy. Hence ionization dominates at low energy while bremsstrahlung is the main process a high energy. The energy for which both energy losses equals is called critical energy E_c . An aproximate formula by Bethe-Hither reads:

$$E_c = \frac{1600mc^2}{Z}$$

Table 4.1 shows values of critical energies for several materials.

Material	$E_c(MeV)$	$X_0(cm)$
Air	102	30050
Argon	45.6	14.0
Al	51	8.9
Pb	9.51	0.56

Table 4.1: *Critical energy and radiation lengths for several materials.*

4.2.1 Multiple scattering

A charged particle traversing matter will fill the coulomb potentials of electrons and nuclei and it will suffer a large number of scattering processes. If we ignore spin and screening effects the cross section of a single scattering is given by the Rutherford formula:

$$\frac{d\sigma}{d\Omega} = Z^2 z^2 r_e^2 \frac{m_e c}{4\beta p sin^2\theta/2}$$

Due to the $sin^2\theta/2$ the majority of the particles will be slightly deflected. Assuming $M >> m$ (with M and m the masses of the nucleus and the incoming particle) the energy transfer to the nuclei is negligible and the trajectory of the incoming particle is a random zig zag with a small deflection angle due to the accumulative effect (figure 4.3).

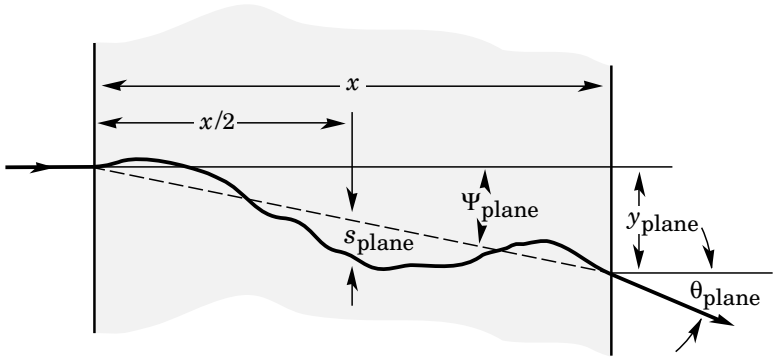

Figure 4.3: Multiple scattering of a charged particle.

If we consider a large number of interactions the problem can be treated statistically . For small angles ($\theta < 30^0$) the Moliere approximation can be used. where the polar angle distribution is expressed as:

$$P(\theta)d\Omega = \eta d\eta \left(2e^{-\eta^2} + \sum_{i=1}^{\infty} \frac{F_i(\eta)}{B_i} \right)$$

where $\eta = \theta/(\theta_1\sqrt{B})$ and B and θ_1 depending on the thickness of the scatterer, its atomic number and on the momentum and change of the incident particle. The function F_k is defined by the integral:

$$F_k(\eta) = \frac{1}{k!}\int J_0(\eta y)e^{-y^2/4}\left[\frac{y^2}{4}ln\frac{y^2}{4}\right]^k ydy$$

At small angles, the angle distribution is close to a gaussian. For larger angles the deflections are mostly due to one single , large angle coming Coulomb scattering rather than the accumulative effect of many small deflections. Hence at large angles the distribution follows the $1/sin^4\theta/2$ typical of the Rutherford distribution.

4.3 Interaction of photons with matter

In contrast with the behaviour of charged particles, in every photon interaction the photon is totally absorbed or scattered at relatively large angles. The former case is due to photoelectric effect and pair production whereas the latter correspond to the Comptom effect. This section briefly describes these processes.

4.3.1 The photoelectric effect

When a photon of energy $E_\gamma = h\nu$ traverses a block of matter, it could be absorbed liberating an atomic electron if $E_\gamma > B_e$, being B_e the bending energy of the corresponding electron. Hence, the energy of the free electron is:

$$E_e = h\nu - B_e$$

The computation of the cross section is complicated due to the discontinuities associated to the different bending energies. For energies relatively large ($h\nu/m_ec^2 >>$ 1, i.e , a few MeV) the cross section may be approximated by:

$$\sigma_{ph} = 4\pi r_e^2 Z^5 \alpha^4 \frac{m_e c^2}{E_\gamma}$$

The $1/E_\gamma$ dependence makes this process negligible at the scale of energies of interest in this work.

4.3.2 The Comptom effect

It is known as Comptom effect the interaction of photons with quasy-free atomic electrons. The differential cross section of this process is given by the Klein-Nishina formula:

$$\frac{d\sigma}{d\Omega} = \frac{r_e^2}{2\left[1+\gamma(1+cos\theta)\right]^2}\left(1+cos^2\theta+\frac{\gamma^2(1+cos\theta)^2}{1+\gamma(1-cos\theta)}\right)$$

with r_e the classical electron radius and $\gamma = h\nu/m_ec^2$. Integrated over the solid angle, the cross section is:

$$\sigma_{comp} = 2\pi r_2^2 \left(\frac{1+\gamma}{\gamma^2} \left[\frac{2(1+\gamma)}{1+2\gamma} - \frac{ln(1+\gamma)}{\gamma} \right] + -\frac{ln(1+\gamma)}{2\gamma} - \frac{1+3\gamma}{(1+2\gamma)^2} \right)$$

The Comptom cross section, being higher that the photoelectric cross section at the energies of interest, decreases with energy and it is also negligible for the interest of this thesis work

4.3.3 Pair creation

This process corresponds to the absorption of a photon (by an atomic nucleus or an atomic electron) producing a pair e^+e^-. For kinematic reasons this process will only occur for photons of energy $E_\gamma > 2m_0c^2$ ($4m_0c^2$ if its produce in the field of an atomic electron). Hence, the pair productions only contributes at high energies and it is the main contributing process for energies above a few MeV. This effect is also parameterized in terms of a creening variable:

$$\xi = \frac{100 m_0 c^2 E_\gamma}{E_+ E_- Z^{1/3}}$$

with E_- (E_+) the energy of the outgoing electron (positron) and $E_\gamma = E_+ + E_-$ the energy of the incoming photon.

In the case of full screening, i.e, $\xi \to 0$:

$$\left(\frac{d\sigma}{dE_+} \right) = \frac{4\alpha Z^2 r_e^2}{E_\gamma} \left((w_+^2 + w_-^2 + \frac{2}{3} w_+ w_-) \left[ln \left(\frac{183}{Z^{1/3}} \right) - f(Z) \right] - \frac{w_+ w_-}{9} \right)$$

where $w_\pm = E_\pm / E_\gamma$ and $f(Z)$ defined was defined when describing bremsstrahlung. Integrated over the energy of the outgoing positron, the cross section is given by:

$$\sigma_{pair} = 4\alpha Z^2 r_e^2 \left[\frac{7}{9} \left(ln \frac{2E_\gamma}{m_0 c^2} - f(Z) \right) - \frac{109}{54} \right]$$

The mean free path $\lambda_{pair} = 1/N\sigma_{pair}$ is usually defined as the distance a photon traveld before converting into a par e^+e^-. This quantity is only material dependent and related to the radiation length by $\lambda_{pair} \approx 9/7 X_0$.

As a summary figure 4.4 shows a break down of the total photon cross section as a function of the energy in carbon and lead. The photoelectric cross section σ_{pe} is the largest contribution at low energy where the discontinuities due to the different bending energies can be seen. The central part is dominated by the Comptom process whereas at very high energy the pair production dominates (κ_{nucl} and κ_e for pair production in the field of the nucleus and electron respectively). Note that for very high energy the cross section reaches a plateau where it can be considered energy independent.

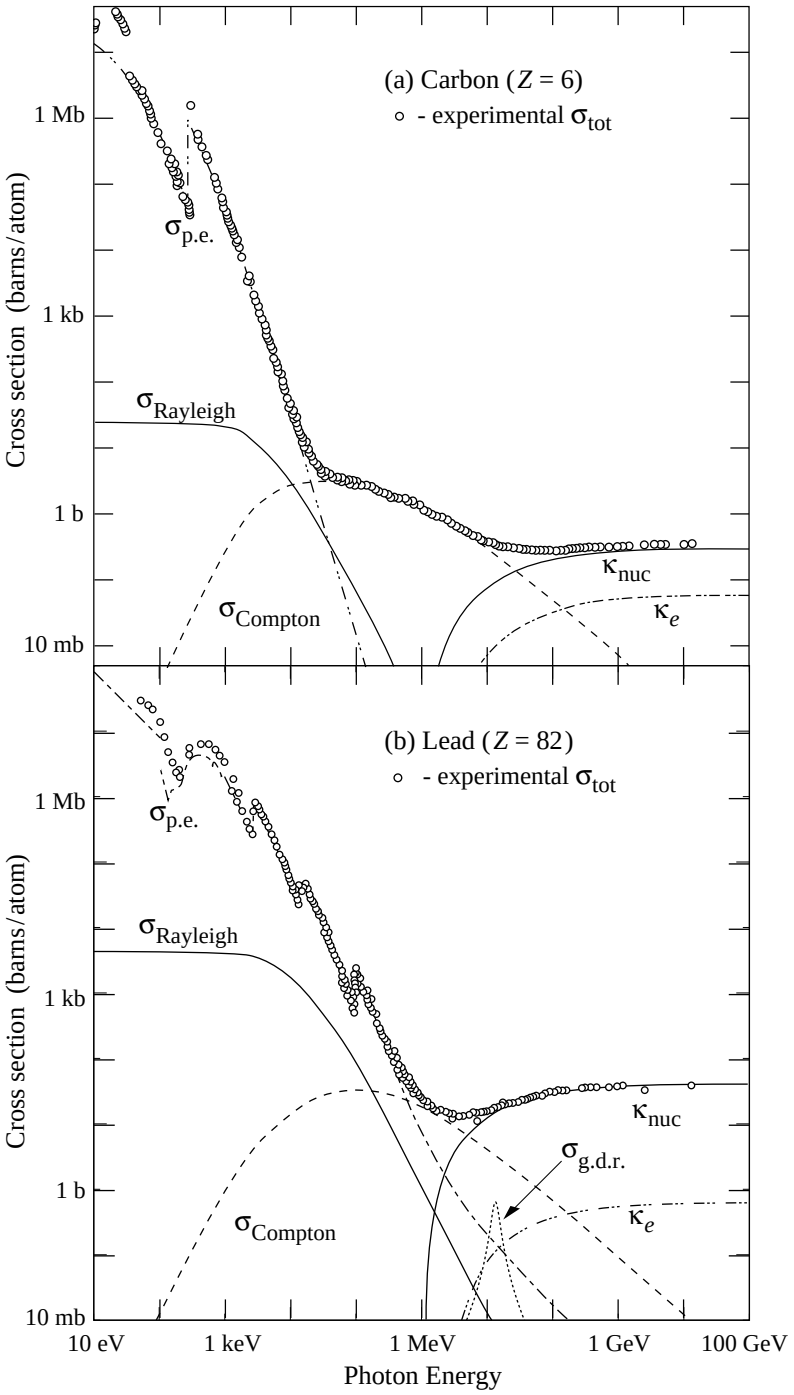

Figure 4.4: Different contributions to the photon cross section in lead and carbon. The figure was taken from [17]

4.4 Electromagnetic Showers

We call electromagnetic showers to those generated by an electron, positron or photon reaching a calorimeter. In this paragraph the mechanism of shower generation and the resolution achievable in an energy measurement involving an electromagnetic shower are discussed.

4.4.1 Shower generation

Several mechanisms contribute to the energy loss of electrons and photons incident on matter. However at high energies (well above $10\,MeV$) the fraction of energy lost per unit depth of material is almost energy independent and only due to bremsstrahlung (electrons or positrons) and pair creation (photons). The secondary particles produced in the cascade carry successively less energy until they reach the range where several other effects (Compton scattering and ionization) become important. If the whole shower is absorbed inside the calorimeter, the energy deposited is obviously equal to that of the primary particle.

For electrons and positrons the process that become relevant in the sub-GeV range is ionization. Positrons in addition suffer annihilation. Ionization is in fact the dominant process and the reason why all particles finally get absorbed. For photons the Compton and photoelectric effect are the ones that compete with pair production at low energies.

At high energies ($E > 1\,GeV$) the absorption can thus be characterised in a material-independent way by using the previously defined radiation length (X_0). Thus the typical shower particle energy at a given depth z (given in cm) is

$$E = E_0 \cdot e^{-\frac{z}{X_0}} = E_0 \cdot e^{-t}$$

where E_0 is the initial energy of the incident electron or positron. Obviously t is the depth measured in units of X_0.

At energies lower than the critical energy the ionization becomes as important as bremsstrahlung. Hence, this energy represents the limit where the growth of the shower stops and the particle multiplicity starts to decrease

A very simplified model of shower developement can provide some insight into electromagnetic calorimetry, assuming that the only dominant processes at high energies are bremsstrahlung and pair production and describing these two mechanisms by asymptotic formulae.

An electron entering a calorimeter with energy E much larger than the critical energy ϵ_0, after having crossed one radiation length of material (X_0), will have lost 63% of its initial energy into photon. We can say that on average the photon and the electron will carry each half of the original energy, $E/2$. After another radiation length of material the photon will create an e^+e^- pair and the electron will emit another bremsstrahlung photon. The energy of each of the four particles will be on average $E/4$. The multiplication process proceeds (figure 4.5). When the shower particles reach an energy below ϵ_0 they are completely absorbed by collisions and

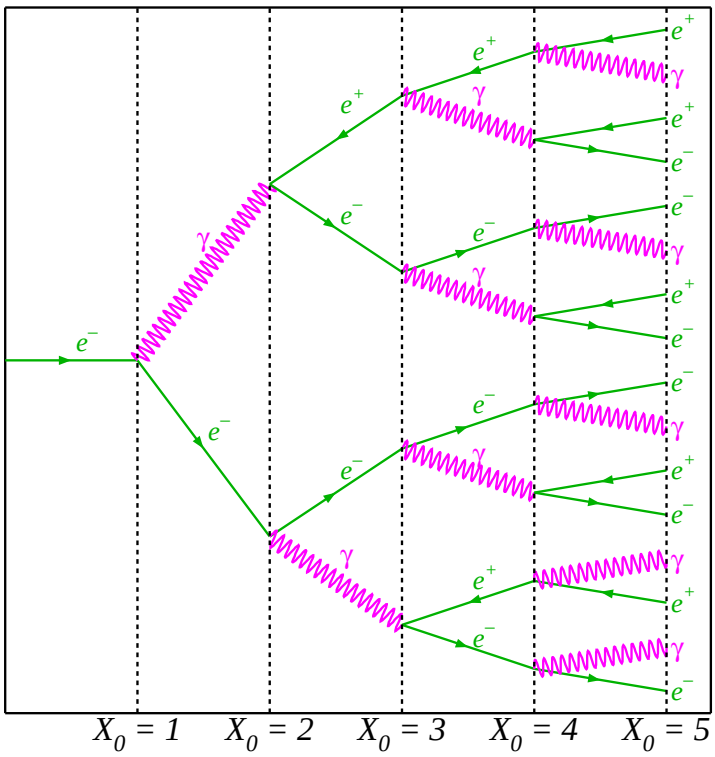

Figure 4.5: Schematic view of an electromagnetic shower

the shower terminates. The model is equally valid if the original particle is a photon, except for a small shift in depth.

The number of particles doubles after each radiation length. Therefore at a depth t (in units of X_0) the number of shower particles is

$$N = 2^t$$

The mean energy of a particle will then be

$$\epsilon = \frac{E}{N} = E \cdot 2^{-t}$$

The depth at which the mean energy ϵ equals the critical energy ϵ_0 is where the shower reaches its maximum particle multiplicity, that is:

$$ln\,(N_{max}) = ln\,(E/\epsilon_0) \Rightarrow ln\left(2^{t_{max}}\right) = ln\,(E/\epsilon_0)$$

Hence,

$$t_{max} \simeq \frac{ln\,(E/\epsilon_0)}{ln2} \tag{4.5}$$

The average total distance covered by all the particles of the shower is called the average *total track length* T. Since each particle travels on average a distance X_0

before splitting into two, the quantity T, in units of X_0, is equal to the total number of particles in the shower.

As the showering process occurs, a small part of the energy is lost by ionization and this fraction is proportional to the total track length, because each energetic particle of the shower deposits an amount of energy per unit length independent of the energy it carries. That is:

$$E_{visible} = E_{ionization} \propto T = \frac{E}{\epsilon_0}$$

This linear relation between the incident energy and the total track length or energy loss by ionization makes calorimeters useful devices.

In general the whole track length will not be detectable, but only a fraction of it, T_d. Only shower particles above a certain energy threshold η will be detected, so we can write

$$T_d \simeq F(\eta) \cdot T = F(\eta) \cdot \frac{E}{\epsilon_0}$$

In order to ensure the full containment of the shower in the calorimeter, both experimental information and some calculation can be used [21]. The length necessary to ensure a 98% energy shower containment can be parametrized as

$$< L_{98\%} > \simeq t_{max} + 4\lambda_{att}$$

where the quantity λ_{att} comes from the exponential decay of the shower energy density deposition (following $e^{-t/\lambda_{att}}$) after reaching the maximum (see 4.6). This λ_{att} turns out to be approximately energy-independent and can be characterized in terms of the radiation length as $\lambda_{att} \simeq (3.4 \pm 0.5) X_0$. Notice that the depth necessary for a calorimeter to fully contain and measure a shower grows only *logarithmically* with the energy (see eq. 4.5).

The shower also develops transversally to the primary particle direction due to the scattering angle of the different interaction processes. Averaging to enough number of events, the transverse energy deposits of the shower can be parametrized by two decreasing exponential functions in the polar variable r, with different length parameters [22]. The first exponential with a small mean length represents the core of the shower, while the second one with a larger mean-length takes into account the spread of the low energy particles in the last stages of the shower development (mainly the multiple scattering process). The fluctuations around this average transverse profile are estimated to be small. The Moliére radius (R_M) is a characteristic constant of a material giving the scale of the transverse dimension of the shower in units of radiation lenghts. By definition, a cylinder with axis the direction of the incident electron and radius $2R_M$ contains on average 95% of the shower energy. An approximate relation for R_M is:

$$R_M = 0.0265 X_0 (Z + 1.2)$$

For example, for lead $R_M = 12.3\ mm$ and for liquid Argon $R_M = 71.2\ mm$.

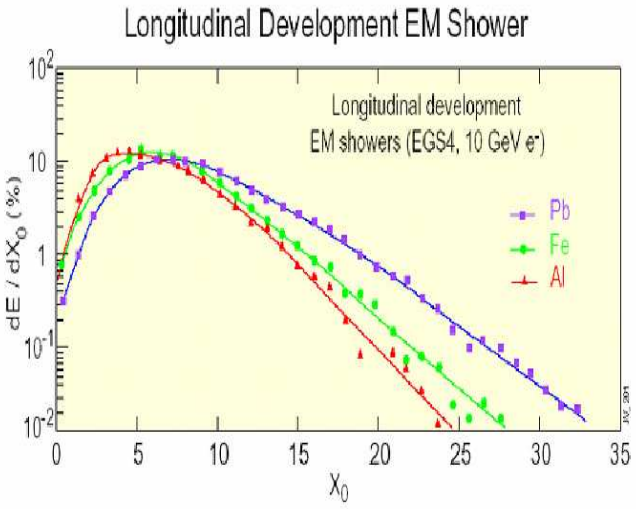

Figure 4.6: Average longitudinal energy deposition of electromagnetic showers for three types of materials: Lead (blue), Iron (green) and Aluminum (red).

4.4.2 Energy resolution

The processes of energy deposition, detection and read out are of statistical nature. The relative precision of the energy measurement can be obtained as:

$$\frac{\sigma\left(E_{visible}\right)}{E_{visible}}$$

where $\sigma(E_{visible})$ is the standard deviation of the variable $E_{visible}$.

Intrinsic fluctuations

Two kinds of uncertainties enter the energy measurement. First, the showering is in itself a statistical process, of almost gaussian character. Landau fluctuations [23] due to ionization processes with large energy transfer to the electrons of the detector material, lead to asymmetric spectra. They are however not quantitatively significant in the case of the ATLAS calorimeter.

The visible energy is, as shown above, proportional to the number of particles produced (N), but also to the number detected (N_d). Both are large numbers that will follow normal distributions. The standard deviation will thus scale as $\sigma \sim \sqrt{N}$. Then

$$\frac{\sigma(E)}{E} \sim \frac{\sigma(N_d)}{N_d} = \frac{\sqrt{N_d}}{N_d} = \frac{1}{\sqrt{N_d}} \propto \frac{1}{\sqrt{E}}$$

The relation stated above sets a lower limit to the accuracy of the energy measurement, i.e. the *intrinsic fluctuations*. The best homogeneous calorimeters made of scintillating crystals or noble liquids achieve energy resolutions of order $\sigma/E \simeq 1\%/\sqrt{E}$ [21].

Sampling fluctuations

In the case of a sampling calorimeter only the fraction of the particle track that is inside the active part will contribute to the visible signal. Hence, we need to decrease T_d by a factor to consider only the active part. However, we will follow in this section an alternative approach, which uses the sampled (or visible) energy instead. Let E_s be the sampled energy, s the thickness of one calorimeter active layer and $(dE/dx)_s$ the energy deposited by minimum ionising particles in the active layers per unit length. Hence, the number of crossing through the active medium layers will be:

$$N_s = \frac{E_s}{(dE/dx)_s s}$$

The visible energy can approximately be computed as:

$$\frac{E_s}{E} \sim \frac{\left(\frac{dE}{dx}\right)_s \; s}{\left(\frac{dE}{dx}\right)_s \; s + \left(\frac{dE}{dx}\right)_d \; d}$$

where d is the thickness of the absorber layers, and both s and d are expressed in units of radiation lengths.

Since normally $\left(\frac{dE}{dx}\right)_d \; d >> \left(\frac{dE}{dx}\right)_s \; s$, we can write the following approximation:

$$\frac{E_s}{E} \sim \frac{\left(\frac{dE}{dx}\right)_s \; s}{\left(\frac{dE}{dx}\right)_d \; d}$$

Hence,

$$N_s \sim \frac{E}{\left(\frac{dE}{dx}\right)_d \; d}$$

Therefore,

$$\frac{\sigma_s}{E_s} = \frac{1}{\sqrt{N_s}} = \sqrt{\frac{\left(\frac{dE}{dx}\right)_d \; d}{E}}$$

If d is in units of X_0:

$$\left(\frac{dE}{dx}\right)_d \sim \frac{E}{T} = \epsilon_0$$

where ϵ_0 is the critical energy of the absorber material, then,

$$\frac{\sigma_s}{E_s} = \sqrt{\frac{\epsilon_0 \; d}{E}}$$

where d is given in units of X_0.

Expressing the critical energy ϵ_0 in units of MeV and the energy E in GeV, previous relation becomes:

$$\frac{\sigma_s}{E_s} = 0.032\sqrt{\frac{\epsilon_0\ d}{E}} = R\sqrt{\frac{d}{E}}$$

where $R = 0.032\sqrt{\epsilon_0}$.

The formula above must be corrected for multiple scattering. Once the passive material is fixed, this correction can be reabsorbed in the constant R. The sampling fluctuations of the ATLAS Electromagnetic Calorimeter followed the previous approach, hence, the decrease law as $1/\sqrt{E}$.

Other fluctuations.

There are other sources of degradation of the energy resolution like non-uniformities, mechanical imperfections, energy leaking behind the calorimeter (in case the depth is not enough), misscalibrations, etc.

In general this type of imperfections do not follow the same scaling law as the sampling fluctuations, generating a constant term that dominates the energy resolution at high energies.

To sum up, the energy resolution of a sampling calorimeter can be parametrized by the formula [1]

$$\frac{\sigma_E}{E} = \frac{a}{\sqrt{E}} \oplus b$$

where the symbol $\oplus$ stands for the quadratic sum, that is:

$$\frac{\sigma_E}{E} = \sqrt{\frac{a^2}{E} + b^2}$$

The presence of noise, for instance in the readout chain, introduces an additional term which scales as $1/E$, since the $\sigma(noise)$ does not depend on the energy of the incoming particle. Hence,

$$\frac{\sigma_E}{E} = \frac{a}{\sqrt{E}} \oplus b \oplus \frac{c}{E}$$

[1] Electronics noise is not taken into account at this stage.

Chapter 5

The ATLAS EMEC

5.1 Introduction and Calorimeter requirements

Electromagnetic Calorimetry will play a main role in the understanding of the physics outcoming from proton-ptoton collisions in the LHC, since many processes will manifest themselves through photonic and electronic final states. The main task of the atlas electromagnetic calorimeter is to meassure energy and position of electrons, photons and jets (portion of jets), measurement of the transverse momentum (p_T) of the event and particle identification (specially electrons and photons). It is the only device to identify photons, since they do not leave any track in the Inner Detector. Several benchmark physics channels such as $H \rightarrow \gamma\gamma$, $H \rightarrow 4e$ or Z'or W' identification put the most tight constrains on the construction of the calorimeter. In this section we just describe those requirements of interest for the understanding of the presented work:

- Search for rare processes require a very good η coverage, as well as the measurement of the missing transverse energy of the event.

- The strongest constrains in terms of energy resolution are based on higgs searches. The channels $H \rightarrow \gamma\gamma$ and $H \rightarrow 4e$ need a mass resolution of 1% in the region $114GeV < M_H < 219GeV$ which requires a sampling term of about $\sim \frac{10\%}{\sqrt{E(GeV)}}$ and a constant term lower than $\sim 0.7\%$. In addition the energy scale must be controlled at the level of 0.1%.

- It is necesary to obtain a linearity better that 0.1%.

- Electron reconstruction capability from $1\,GeV$ to $5\,TeV$. The lower limit comes from the need of reconstructing electrons from b quark decay. The upper one is set by heavy gauge boson decays.

- The total thikness of at least 24 radiation lenghts (X_0) such that the resolution, linearity and energy scale are not affected by energy leaked behind the calorimeter for high energy particles ($E > 500GeV$).

- Excelent electron/jet and photon/jet separation. The main source of missidentification of electrons and photons is hadronic jets. For example, a high p_T π^0 decays in two high p_T photons, which, going very close together, may look as one photon of a Higgs decay channel $H \rightarrow \gamma\gamma$. To distinguish the two photons of the π^0 decay, a fine lateral (granularity) in the calorimeter is required.

5.2 The End-Cap Electromagnetic Calorimeter.

The ATLAS Electromagnetic End-Cap Calorimeter, is a sampling calorimeter with lead as absorber or passive material and Liquid ARgon (LAR) as an active material [16]. An accordion shape is given to all plates in order to avoid crack regions due to cables and boards of the readout. A picture of the accordion shape is shown in figure 5.1. Particles, which are incident onto the calorimeter from left to right of the picture, perceive the alternate Lead-LAr structure of the sampling calorimeter.

Figure 5.1: Accordion shape in EMEC inner wheel

The Argon is kept liquid at a temperature of $\sim 89^o K$ through a cryogenic system, being the EMEC inside a cryostat vessel, which has two walls separated by vacuum for better thermal isolation.

There are two EMEC, in their respective cryostats, located at the two mirror End-Cap positions, one at $z \sim -350\ cm$ (EMEC-C) and the other one at $z \sim 350\ cm$ (EMEC-A) of the nominal ATLAS interaction point (see figure 3.2). Each EMEC End-Cap has a cylindrical (wheel) form being the internal and external radii of about 30 cm and 200 cm respectively, and about 63 cm thick. In Figure 5.2 a picture of one EMEC inside the cryostat, seen from the back, is shown, together with a schematic drawing of the EMEC cylinder with some absorbers in it. The readout cables (orange-color) coming from the back side are seen in the picture as well as the 30cm-radius hole in the center to accommodate the beam pipe (as well as to leave place to the forward calorimeter behind). In order to acomodate the acordion

geometry the absorber plates are arranged radially like the spokes of a bicycle wheel and the accordion waves are paralel to the front and back edges of the wheel and run in depth (see drawing of figure 5.2).

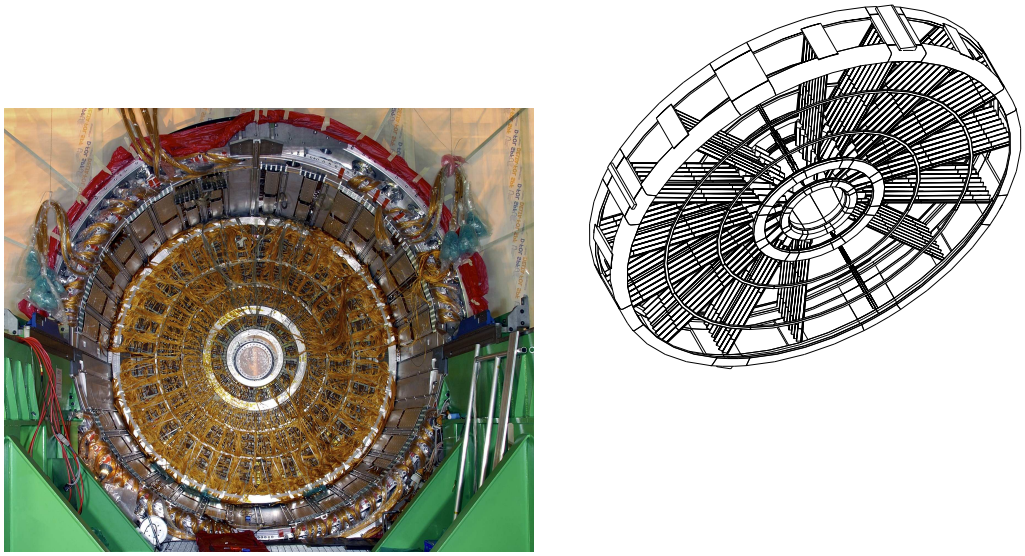

(a) Picture of an EMEC wheel inside the End-Cap Cryostat.

(b) Arrangement of absorbers in an EMEC cylindrical wheel

Figure 5.2: EMEC figures

Since the EMEC is a cylindrical wheel, the amplitude of the accordion waves decreases when η increases (when the radious decreases).

Due to mechanical constraints demanded by this accordion shape, a second independent wheel is needed to extend the coverage to $\eta = 3.2$. Hence, there are two wheels, the outer wheel from $\eta = 1.375$ to $\eta = 2.5$ and the inner wheel from $\eta = 2.5$ to $\eta = 3.2$. In the picture of figure 5.2 a metal ring is clearly seen separating the two outer and inner wheels, which is shown in the drawing as well. A discontinuity in the accordion wave shape is seen in the drawing of figure 5.2 when going from the outer to the inner wheel, and can be clearly seen in figure 5.3 where a detail picture of the outer-inner boundary is shown.

The lead is cladded by 0.2 mm thick steel to give it enough rigidity. For the outer wheel, the thickness of the lead plates is 1.7 mm while the LAR gap thickness between two absorbers decreases continously from 5.6 mm (at $\eta = 1.375$) to 1.8 mm (at $\eta = 2.5$). For the inner wheel, the thickness of the lead plates is 2.2 mm (see figure 5.3) while the LAR gap thickness between two absorbers decreases continously from 6.2 mm (at $\eta = 2.5$) to 3.6 mm (at $\eta = 3.2$).

The LAR ionization is collected by electrodes (at high voltage) situated in between two absorbers (at ground) as can be seen in figure 5.3 for the inner wheel as an example. To keep the electrode in the right place, honeycomb spacers are located

Figure 5.3: Stacked layer of the inner wheel. The electrode is placed in between two absorbers.

in between the absorber and the electrode, which are also distinguished in figure 5.3. Hence the liquid Argon gap between two absorbers is divided in two parts, the ionization of both being readout by the same electrode. A picture of an outer-wheel electrode is shown in figure 5.4. In the thickness of $0.25mm$ there are 3 copper layers separated by Kapton isolation, namely two layers on top and bottom holding the High Voltage and one layer in the middle to readout the ionization signal by the effect of capacitance coupling. The thicknesses of these layers are given in figure 5.4. The High Voltage (HV) held on the bottom and top electrode layers ranges between 1000 Volts and 2500 Volts depending on pseudorapidity (η) location. For such high values of the voltage a very good isolator, like Kapton, is mandatory to avoid leak current to the signal layer.

To facilitate handling and logistics each EMEC cylinder is divided into 8 octants or modules (see figure 5.5), hence there are 16 modules in total for the two EMEC End-Caps. One half of the modules have been stacked at the CPPM [1] and the other half at UAM [2] under strict clean conditions. These clean conditions are important to avoid short-circuits due to any dust particle entering in the gap between electrode and absorber where the electric field may be higher than 1000 V/mm.

One module consists of 96 (32) layers for the outer (inner) wheel stacked one on top of each other along the azimuthal direction (ϕ). Each layer is a sandwich of absorber, spacer (gap), electrode, spacer (gap). Figure 5.5 represents a picture of a module at the stacking frame of the UAM clean room.

The design is symmetrical in ϕ.

[1] Centre de Physique des Particules de Marseille
[2] Universidad Autónoma de Madrid

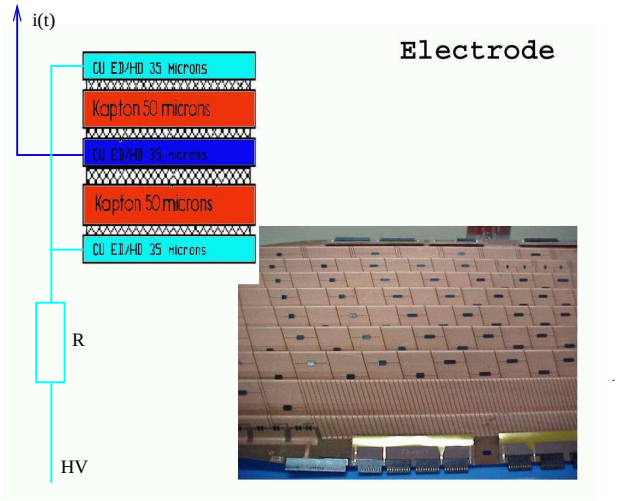

Figure 5.4: Picture of an EMEC electrode. The thin electrode has 3 layers separated by Kapton isolation: two HV layers on the sides and one signal layer inbetween which capture the ionization signal by capacitance coupling.

5.3 Spatial granularity

The EMEC is segmented along the two angular directions, η and ϕ, and along the calorimeter depth.

The electrodes are longitudinally segmented in three (two) compartments, all called samplings, in the outer (inner) wheel of the calorimeter:

- The first sampling (S1 or front) is about $4.4X_0$ thick in the outer wheel while it is about $22X_0$ in the inner wheel.
- The second sampling (S2 or middle) is about $17X_0$ $(2 - 8X_0)$ in the outer (inner) wheel. For particles hiting on the outer wheel most of the energy will be deposited on this second sampling since.
- The third sampling (S3 or back) has a depth between 4 and 12 X_0, depending on η, in the outer wheel. Note that this compartment is not present in the inner wheel. The back layer is used to avoid, as much as possible, the longitudinal leakage of electromagnetic showers.

Figure 5.6 shows a picture of an electrode corresponding to the outer wheel. The front and back sides correspond to the top and bottom parts of the picture respectively, while pseudorapidity η increases from right to left. The three compartments, S1, S2, S3 can be distinguish by the different segmentation along η they have: the S1 compartment on top of the picture, the S3 on the bottom part and the S_2 in between.

As showed in figure 5.6 the granularity along η is also defined in the electrodes by mean of copper strips using kapton as electrical isolator between them. The size

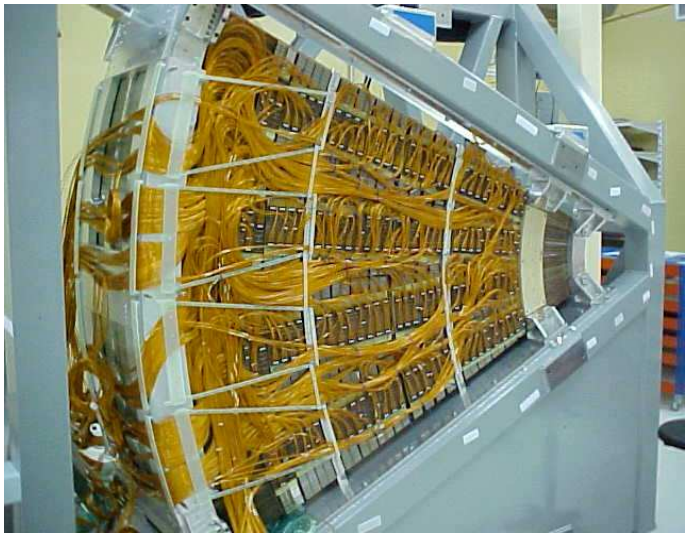

Figure 5.5: Picture of an EMEC module or octant at the stacking frame of the UAM clean room.

of such strips depends on the compartment, being smallest in the S1 to allow for the separation of the two photons from the decay of a π^0. This separation must be done before the cascade generated by the photons gets broader in the calorimeter material, hence the fine segmentation is defined in the front, S_1, compartment.[3] The values of the cell size for the three compartments as a function of η are given in table 5.1. The strips drawn in the electrodes point to the nominal ATLAS interaction point, however the accordion geometry, for example the absorbers, is not projective to that point.

Wheel	η range	Front	Middle	Back
	1.375 - 1.425	(0.050,2π/64)	(0.050,2π/256)	
	1.425 - 1.5	(0.025,2π/64)	(0.025,2π/256)	
Outer	1.5 - 1.8	(0.003,2π/64)	(0.025,2π/256)	(0.050,2π/256)
	1.8 - 2.0	(0.004,2π/64)	(0.025,2π/256)	(0.050,2π/256)
	2.0 - 2.4	(0.006,2π/64)	(0.025,2π/256)	(0.050,2π/256)
	2.4 - 2.5	(0.025,2π/64)	(0.025,2π/256)	(0.050,2π/256)
Inner	2.5 - 3.2	(0.1,2π/64)	(0.1,2π/64)	

Table 5.1: *Transverse granularity* $(\Delta\eta, \Delta\phi)$ *for each calorimeter sampling (Front, Middle and Back).*

[3]Regions $|\eta| < 1.5$ and $|\eta| > 2.5$ do not have very fine longitudinal and transversal granularity since they are out of the high precision measurement region. The former corresponds to the barrel-endcap crack (where the large amount of materials in front will not allow to get as good energy resolution as required) and the latter corresponds to very forward regions (with high noise coming from proton remnant and soft interactions).

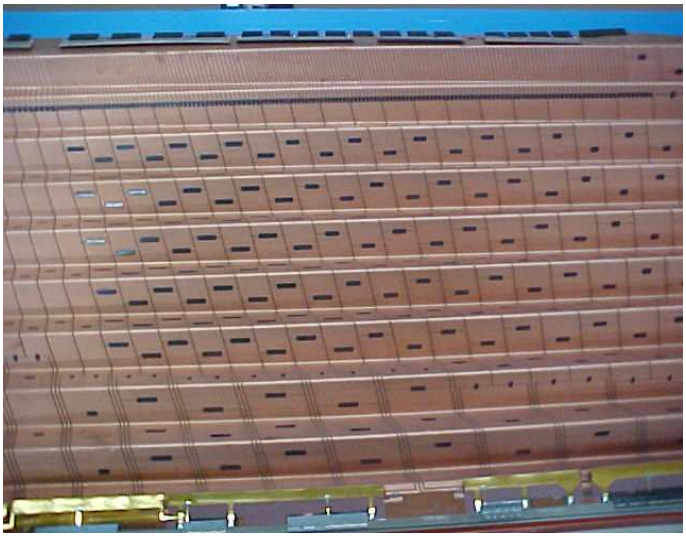

Figure 5.6: Picture of an EMEC electrode of the outer wheel. The segmentation along η and the three compartments in depth, S1,S2 and S3, are clearly seen.

The granularity along the azimuthal ϕ direction is defined by connecting several consecutive electrodes together using the so called summing boards. In principle one could read the electrodes individually, defining a fine granularity along ϕ of 0.003 radians; however this is too much fine for the needs and would increase the number of channels considerably. This is the reason for using Summing Boards (SB) to group the signal of several electrodes together. In this way, for example, in the S2 compartment, three consecutive electrodes are connected (their signals are summed) to obtain the desired granularity of $\Delta\phi = 0.025$ radians, while 12 electrodes are connected for the S1 compartment given a granularity of $\Delta\phi = 0.1$ radians in this compartment. A summary of the EMEC granularity is given in table 5.1.

Figure 5.7 shows some summing boards plugged in the electrode connectors for the S1 compartment of an EMEC module. The ϕ direction goes from bottom to top of the picture, while the η direction increases from left to right. The electrode connectors can be distinguished in black between two absorbers. The summing boards group the signals of 12 electrodes together in this example.

5.4 High Voltage

The relation between the signal (E) and the high voltage (U) applied on the gaps is:

$$E \sim \frac{f_s}{g^{1+b}} U^b \tag{5.1}$$

where g is the liquid argon gap thickness and f_s the sampling fraction (which is a function of the gap thickness). The value for the exponent b was measured at beam beam test of Module 0 to be close to 0.4 [26].

The argon gap of the EMEC decreases almost linearly when the pseudorapidity

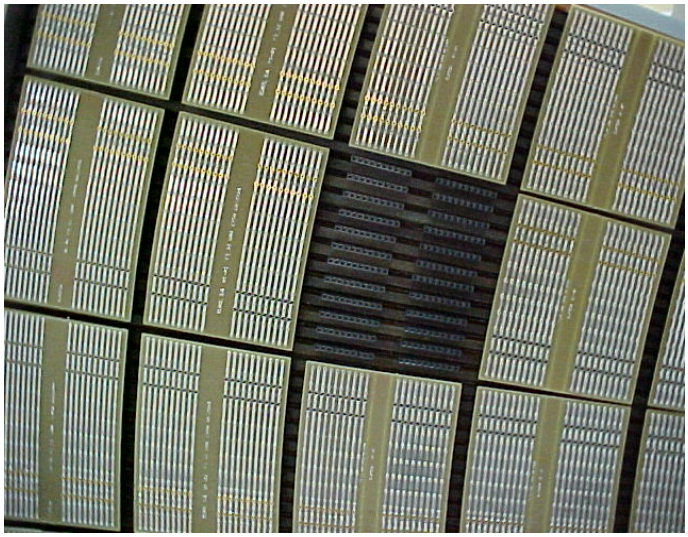

Figure 5.7: Picture the summing boards plugged in the front face of an EMEC module.

	End-cap outer wheel						
HV region	1	2	3	4	5	6	7
η range	1.375-1.5	1.5-1.6	1.6-1.8	1.8-2.0	2.0-2.1	2.1-2.3	2.3-2.5
HV values	2500 V	2300 V	2100 V	1700 V	1500 V	1250 V	1000 V

Table 5.2: *The high voltage regions of the end-cap outer wheel.*

(η) increases. This makes the cluster signal changing along the pseudorapidity direction due to the explicit gap variation and the implicit change in the sampling fraction according to equation 5.1. The sampling fraction (f_s) decreases when η increases, but not fast enough to cancel the $1/g^{1+b}$ rise, as a result the response E increases with η. This growth may be compensated by decreasing U continously when η increases. For practical reasons a decreasing stepwise function for U is chosen defining seven HV sectors, the High-Voltage sector definitions is given in Table 5.2. for the outer wheel [4]. Inside one sector the HV is constant and therefore the cluster signal increases with η. To correct for the increase of the cluster signal inside HV sectors, η-dependent weights ($w^{(s)}$) are applied on each cell:

$$w^{(s)}(\eta_j) = \beta^{(s)}/(1 + \alpha^{(s)}(\eta_j - \eta^{(s)})) \tag{5.2}$$

where for a given sampling layer (front, middle or back) η_j is the cell pseudorapidity and $\eta^{(s)}$ the pseudorapidity at the centre of the HV sector s. The parameter $\alpha^{(s)}$ is the slope of the energy dependence with η and the parameter $\beta^{(s)}$ accounts for inaccurate high voltage settings. Both parameters were obtained from a fit to the test beam data [27, 41].

[4] There are two additional sectors in the inner wheel which are not given on the table

5.5 Presampler

In figure 5.8 (a) a schematic view of a quadrant of the electromagnetic calorimeter is shown. An electron, positron or photon created in one p-p collision will cross different layers of material, of the inner detector, cables, boards, cryostat walls, etc, before it enters into the End-Cap Electromagnetic Calorimeter (EMEC). The particle may start a particle-shower (or particle-cascade) crossing these consecutive material layers by the effect of the bremsstrahlung process (photon emission by an electron or positron) or the pair creation process (e^+e^- creation by a photon). Every secondary particle may suffer either the bremsstrahlung process (in case of e^+ or e^-) or pair creation (in case of γ) creating tertiary particles and so on. In this way a cascade is developed. Every charged particle of this cascade will lose part of its energy by ionization of the material. In addition, the $2T$ magnetic field may bent some of the charged particles of the cascade such that they hit the calorimeter at an unexpected position. The result is that the energy measured in the calorimeter will be smaller than the initial particle energy as produced in the p-p collision.

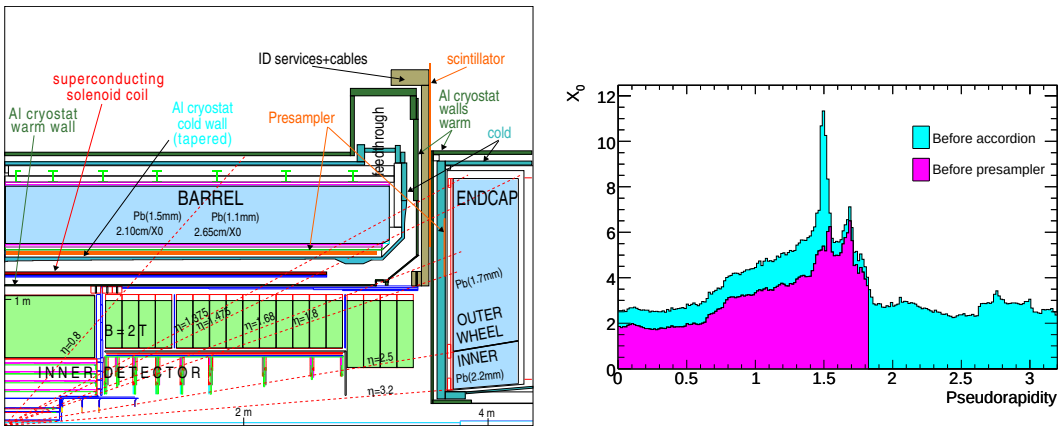

(a) Longitudinal view of a quadrant of the EM calorimeter

(b) Material in front of the presampler and bafore the accordion

Figure 5.8: Description of the material in front of the calorimeter

The amount of material depends on the η direction, as can be seen in figure 5.8 (b), where the amount of material is expressed in units of radiation lengths (X_0) and it goes up to about $5 - 7X_0$ in the region $1.5 < |\eta| < 1.8$ degrading the measured energy. In order to partially recover this resolution a presampler detector is placed in front of the calorimeter in the region $1.5 < |\eta| < 1.8$. The endcap presampler is divided into 768 cells per endcap wheel with a transversal segmentation of $\Delta\eta \times \Delta\phi = 0.025 \times 2 \cdot \pi/64$. The quoted segmentation along ϕ is achieved by the modularity in 32 identical azimutal modules. Each module consist of two active Liquid Argon layers, 2 mm thick, formed by three electrodes paralells to the front face of the EMEC.

Figure 5.9 shows the material in front of the calorimeter different layers of the EMEC versus η. Note that only the region $1.55 < |\eta| < 2.5$ is covered in this work.

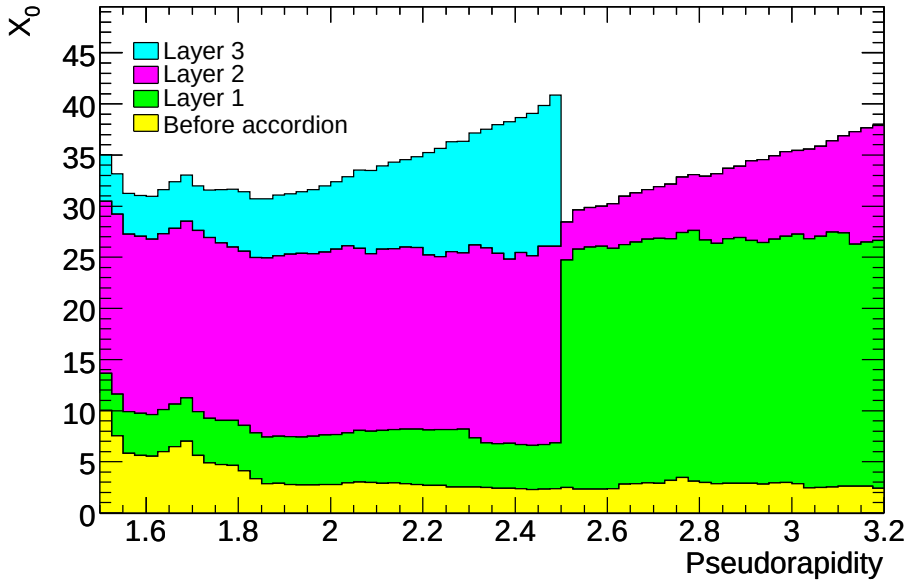

Figure 5.9: *Total ammount of material in front of the different samplings of the EMEC vs* η

Chapter 6

The Calibration Hits method

An electron/photon deposits energy in several cells of the calorimeter due to EM shower created by the interaction with matter. A cluster of cells is then defined to contain the energy deposits, or at least most of them, in order to compute the electron/photon) energy. However, several effects distort this calculation, namely:

- Energy lost in front of the calorimeter. A particle coming from the interaction point passes through Inner detector (ID), cables, boards, cryostats, etc depositing part of its energy before getting to the calorimeter.
- Energy leaked behind the calorimeter. Despite the about 25 X_0 length of the EM ATLAS calorimeter, a small percentage of the particle shower is leaked behind, specially for the highest energies.
- Energy leaked outside the cluster. The size of the cluster chosen to reconstruct the energy is a compromise between the noise and the lateral shower containment. The EM shower is a bit wider than the cluster width. The energy lost by this effect can be corrected easily. However, the magnetic field of the Inner Detector deflects secondary charged particles which may miss the defined cluster. These secondary particles are produced when electrons of photons interact with the material of the ID.

Figure 6.1 shows the energy scale (right) and resolution (left) for 100 GeV particles when no correction is applied for the various losses. The resolution can be an order of magnitude worse than the expected by design (an ideal $10\%/\sqrt{(}E) \oplus 0.7\%$ would correspond with $\sigma/E \sim 0.012$, represented with a green line in the graphic) and the energy 60 % of the true one. In this section, a procedure to correct for the different effect in the EMEC is presented. What it is proposed is a development of ideas introduced in [29], [30] and [31] to analyze test beam data using some EMB modules and in [32] to reconstruct the energy of electrons in the EMB using a Monte Carlo simulation of the ATLAS nominal set up. The aim of this technique is to provide a modular way to recover the energy of electrons/photons by decoupling the energy losses in the calorimeter, and upstream and downstream material.

The method relies in a special Monte Carlo simulation (labeled Calibration Hits) which records the energy deposits in all the materials of the detector and not only the

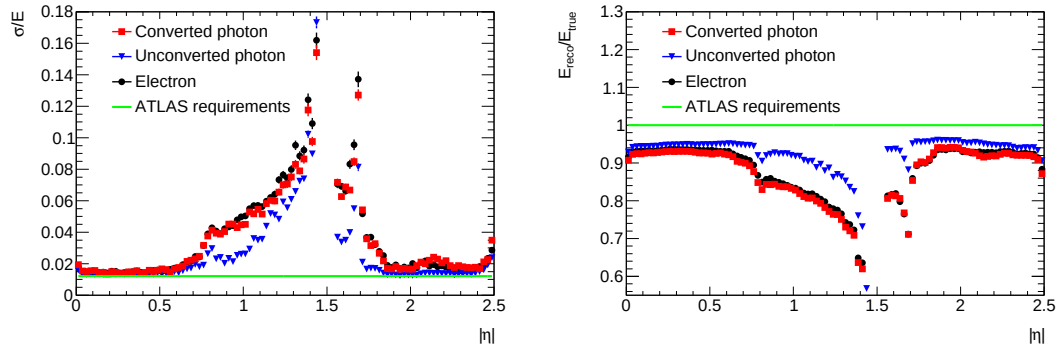

(a) Resolution for 100 GeV particles

(b) Energy scale for 100 GeV particles

Figure 6.1: *Uncorrected energy scale and resolution for electrons (black circles), converted photons (blue triangles) and unconverted photons (black squares) . The green line represents the ATLAS nominal requirements*

active ones. This allows to find correlations between the different energy losses and measurable quantities, such us energies in presampler, front, middle and back and the estimated longitudinal barycenter of the electromagnetic shower. In this work, the calibration procedure is applied to the EM EndCap Calorimeter (EMEC), taking into account the peculiarities of this device: different geometry, different dead material in front and the presampler does not cover the whole range in pseudorapidity (η). These differences between the EMEC and the EMB forced us to do some modifications in the Calibration Hits method, in particular in the region without presampler a new algorithm had to be developed to recover the energy lost in front of the EMEC

6.1 Monte Carlo samples.

For the analysis presented in this thesis, the centrally-produced samples summarized in table 6.1 were used. The simulation was performed using ATHENA 14.2.28 which incorporates GEANT 4.7 [33] for the particle-matter interaction. Each event corresponds to a single electron initially at the nominal ATLAS interaction vertex. The particle direction is changed from event to event according to a uniform distribution along both eta and phi. Only the high precision region is considered in the analysis, namely $|\eta| < 2.5$. The initial vertex is left to fluctuate in order to simulate the z-width of the LHC proton bunches. The ATLAS magnetic field is also included in the simulation. However, neither the electronic nor pile-up noise is included in the simulation.

Digitization and reconstruction [1] stages are taken into account to profit from

[1]The simulation of ATLAS events is performed in five steps: Generation (where the kinematics of the event is produced), Simulation (where GEANT emulates the interaction of every particle with matter), Digitization (where the readout and all the electronics is simulated), Reconstruction (where all variables of interest are computed from raw data) and ESD and AOD production (those last steps produce standard object to work with when doing physics analysis). Even though we are working at the simulation level, we run the two following steps to get the information needed for

E (GeV)	DSname	Evts (M)	DSname	Evts (M)
25	7072	~ 0.8	7082	~ 1.2
50	7060	~ 0.8	7062	~ 1.2
75	7073	~ 0.8	7083	~ 1.2
100	7061	~ 0.8	7063	~ 1.2
200	7074	~ 0.8	7084	~ 1.2
500	7075	~ 0.4	7083	~ 0.4
1000	7076	~ 0.2	7083	~ 0.2

Table 6.1: *Energy, data set number and number of events for the electron (left) and photon (right) samples used in this work*

extra information as the presence of tracks, to distinguish between electrons and photons, or EM particle identification (see Appendix A), to determine the quality of electrons. After these stages, cell energies are corrected by the effect of the gap size variation with η inside high voltage regions of the EMEC inside each high voltage region of the EMEC (see equation 5.2).

6.2 Cluster Energy

When an electron or photon goes through the ATLAS calorimeter it deposits part of its energy in several cells of the different layers. In order to reconstruct the energy of the incoming particle a cluster of cells is built using the Sliding Window (SW) algorithm [35]. The SW clustering algorithm [2] works in three steps, namely:

- Tower building. The (η,ϕ) plane of the calorimeter (up to $|\eta| = 2.5$) is divided into a grid of $N_\eta \times N_\phi = 200 \times 256$ elements of size $\Delta\eta \times \Delta\phi = 0.025 \times 2\pi/256$. The energy of all cells in all longitudinal layers within each of this elements is summed into the "tower" energy.

- Precluster finding. A window of size 5×5 in units of tower size is moved along the tower grid defined above. If the sum of the transverse energy of the towers contained in the window is a local maximum and is above a certain threshold E_T^{Thres} [3], a precluster is formed. The position of the precluster is computed as the energy weighted η and ϕ barycentres of all cells within a window of 3×3 towers around the central one. Finally, if two preclusters are found in a position within a distance $\Delta\eta \times \Delta\phi = 0.05 \times 0.05$ the one with higher transverse energy is kept.

particle identification.

[2] In the ATLAS reconstruction program two type of SW clusters are built: Electromagnetic (used for electrons and photons) and combined (used for jets and tau leptons). In this document only electromagnetic SW clusters are described.

[3] (In this work the $E_T^{Thres} = 3\ GeV$ although in newer releases of the ATLAS software this threshold has been lowered up to 2.5 GeV in order to avoid cluster duplication.)

- Cluster filling. The positions of pre-clusters are used as seeds around which final clusters are subsequently filled. The EM cluster filling consists of including all cells (of chosen calorimeter layers) that are located inside a rectangle of size $N_{\eta}^{clus} \times N_{\phi}^{clus}$ centered on the seed position. The rectangular size is given in tower units. Clusters of different sizes re built depending on the location in the calorimeter and the type of particle which produces it (see Table 6.2). Ideally, the cluster should be large enough to transversally contain the full shower limiting the effect of lateral shower fluctuation in the resolution. However, a limited size is chosen in order to minimize the introduction of electronic and pile-up noise expected in the ATLAS detector.

Particle Type	EMB	EMEC
Electron	3×7	5×5
Converted Photon	3×7	5×5
Unconverted Photon	3×5	5×5

Table 6.2: *Cluster size $N_{\eta}^{clus} \times N_{\phi}^{clus}$ for different particle types in the barrel and endcap regions of the EM calorimeter*

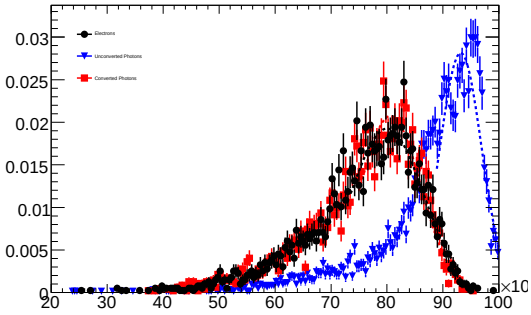

Figure 6.2: Cluster energy distribution for 100 GeV Monte Carlo electrons at $\eta = 1.6375$. Calibration Hits Method is not applied to the events. Long tails are observed towards the lowest energies which make the distribution differ considerably from a gaussian.

The sum of the energies deposited in each cell of the cluster will be named "cluster energy". As an example, a 3×7 cluster energy distribution for 100 GeV particles is represented in figure 6.2 before the Energy Reconstruction method (the Calibration Hit method) is applied to perform the corrections mentioned above. A gaussian fit is plotted as well to observed the deviation of the distribution from a guassian shape.

The clustering algorithm allows also to determine the pseudorapidity and azymuth of the incoming particle using only information from the calorimeter. The pseudorapidity η is computed as:

$$\eta_{calo} = \frac{\sum_{i=0}^{2} w_i \cdot \eta_i}{\sum_{i=0}^{2} w_i} = \frac{\sum_{i=0}^{2} w_i \cdot \sum_s e_s^i \cdot \eta_s^i}{\sum_{i=0}^{2} w_i}$$

and the azymuth;

$$\phi_{calo} = \frac{\sum_s e_s^2 \cdot \phi_s^2}{\sum_s e_s^2}$$

where η_i^s (ϕ_i^s) and e_s^i are the central η (ϕ) value of the $s-th$ cell in the $i-th$ layer of the calorimeter and the energy deposit on the $s-th$ cell and s runs over all the cells in a particular calorimeter layer. In this document we will refer to this magnitudes as η and ϕ since we are only using calorimeter information.

Note that in the computation of ϕ only the second compartment is considered whereas the first compartment is also taken into account in the computation of η. A different weight ($w_i = \sum_s a^i \cdot e_s^i$ with $a^1 = 3$ and $a^2 = 1$) is given to both compartments in order to account for the finer granularity and therefore for the better position resolution of the first layer of the calorimeter.

6.3 Description of the method

When an electromagnetic cluster in the EM Calorimeter is identified, the energy contained in this cluster of calorimeter cells is less than the original energy of the incoming particle due to different losses, namely: energy losses in the inactive materials in front of the calorimeter, energy deposited in the inactive part of the calorimeter or transversally leaked out of the defined cluster and energy longitudinally leaked behind the calorimeter. Therefore, the reconstructed energy of the electron/photon may be written as follows:

$$E_{reco} = E_{front} + E_{calo} + E_{behind} \tag{6.1}$$

where all three contributions are derived by using measurable quantities such as the energy in the presampler (when present) and the three different layers of the calorimeter (E_{ps}, E_1, E_2 and E_3), the pseudorapidity (η) of the incoming particle and the longitudinal barycenter of the electromagnetic shower computed as:

$$X = \frac{\sum_{i=1}^{3} E_i \cdot X_i}{\sum_{i=1}^{3} E_i} \tag{6.2}$$

being X_i, $i = 1, 2, 3$ the front, middle and back geometrical centers in units of radiation length (X_0).

In the current version of the Calibration Hits Method (CHM), the energy dependence of both E_{front} and E_{behind} is taken into account by parametrizing the correction factors as a function of E_{calo}. Hence, this contribution should be computed first.

6.4 Corrections for energy depositions in the calorimeter

Unless otherwise stated, the energy in the presampler and the three different layers of the calorimeter after the digitization and reconstruction steps will be denoted by E_{ps}, E_1, E_2 and E_3 respectively. These energies include an overall sampling fraction factor.

The reconstructed energy in the electromagnetic calorimeter can be written as:

$$E_{calo} = f_{calo} \cdot (1 + f_{out}) \cdot \sum_{i=1}^{3} E_i \tag{6.3}$$

where f_{calo} is defined as the ratio between the total energy deposited in the cluster (LAr and Lead) and the energy after the digitization and reconstruction steps:

$$f_{calo} = \frac{\sum_{i=1}^{3} E_{cl,i}^{abs} + E_{cl,i}^{lar}}{\sum_{i=1}^{3} E_i} \tag{6.4}$$

whereas f_{out} is the fraction between the total energy deposited out of the cluster and the total energy deposited in the cluster:

$$f_{out} = \frac{\sum_{i=1}^{3} E_{cl,i}^{out}}{\sum_{i=1}^{3} E_{cl,i}^{abs} + E_{cl,i}^{lar}} \tag{6.5}$$

As shown in figure 6.3 the factor f_{calo} is fairly energy independent when parameterized as a function of the longitudinal barycentre (X). Hence, the energy average is obtained for each of the particle types: electrons, unconverted photons and converted photons (see figure 6.3 g and h). Since f_{calo} as function of X does not depend much on the particle type, the profile for unconverted photons is used also for electrons and converted photons, being fitted by a second degree polynomial:

$$f_{calo}(\eta, X) = q_0(\eta) + q_1(\eta) \cdot X + q_2(\eta) \cdot X^2 \tag{6.6}$$

The η dependence of the coefficients means that a set of parameters has been determined for each η-middle-cell value.

In contrast to f_{calo}, the mean of the f_{out} distributions is not energy independent when parametrized as a function of the longitudinal barycenter of the EM shower (Figure 6.4 a). The fout distribution for each X bin is not gaussian, but manifests long tails at high values, as it can be seen in figure 6.4 (b). This is due to bremstrahlung radiation and deflection of low energy particles produced in the early shower by the magnetic field . This tails clearly depend on the energy of the incoming particle being shorter for higher energies. However, the peak of the distribution is fairly energy independent which makes it more suitable for the present parametrization. Hence, the adopted approach is to produce f_{out} distributions in different X intervals (or bins) and fit each distribution to a landau-like function to extract the position of the maximum or Most Probable Value (MPV). Thereafter, these MPVs are parametrized as a function of X.

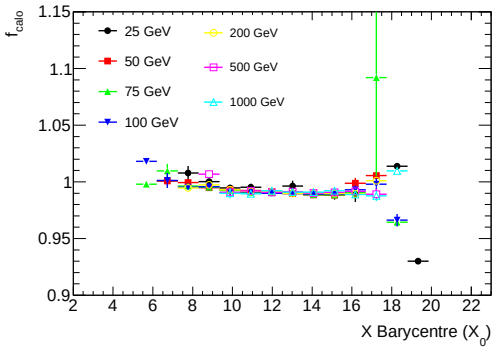

(a) *electrons*

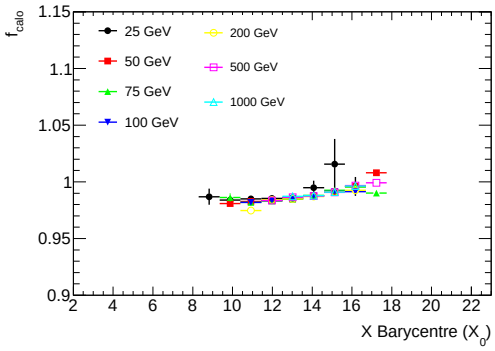

(b) *electrons*

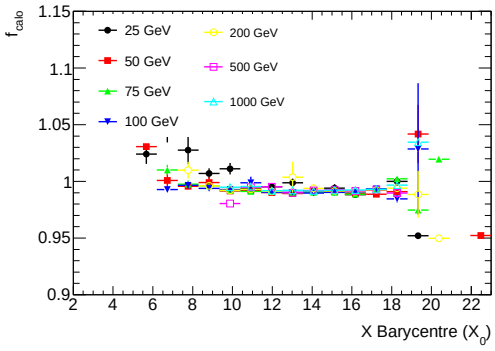

(c) *unconverted photons*

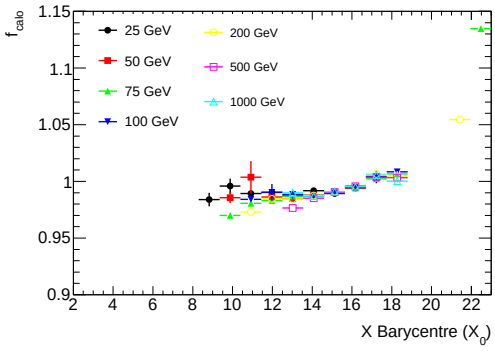

(d) *unconverted photons*

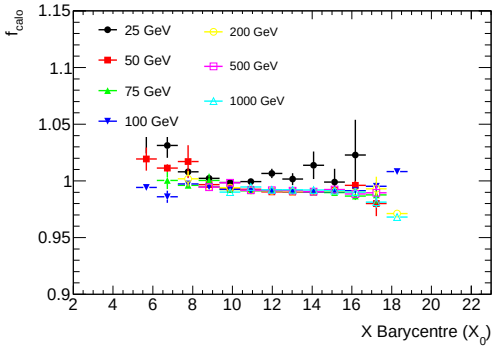

(e) converted photons

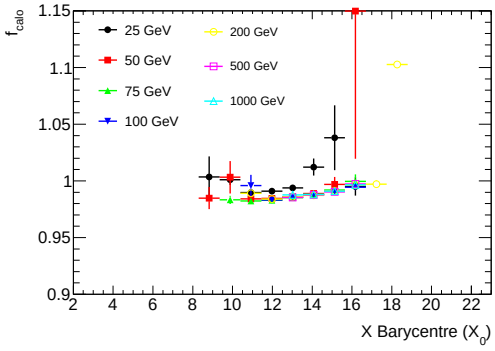

(f) converted photons

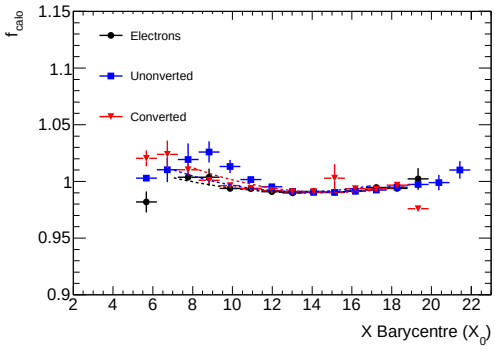

(g) Energy averaged

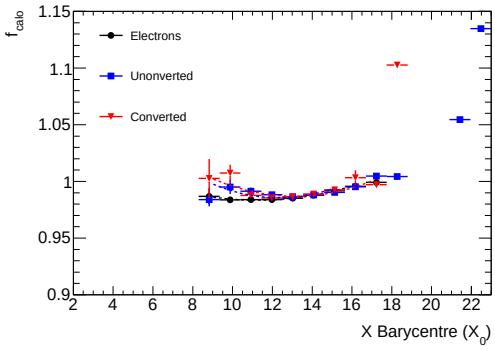

(h) Energy averaged

Figure 6.3: *f_{calo} vs X for the various energies and energy averaged at $\eta = 1.6375$ (left) and $\eta = 1.9125$ (right)*

To give an idea of the quality of the Landau-like fits, three f_{out} distributions are shown in Figure 6.5 a, b and c corresponding to three different X intervals centered at $\sim 10X_0$, $\sim 13.5X_0$ and $\sim 17X_0$, each with a bin size of $\delta X \sim 0.5X_0$. The distributions show a very populated tail for low X whereas the profiles at high X are more gaussian-like. This reflects into a high overestimation of the f_{out} correction if the average is taken by default. Moreover, as shown in figure 6.6 [4] , the energy independence is recovered if the MPV of the distribution is taken as the correction factor. An energy average profile of f_{out} vs X (as explained above) is then fitted:

$$f_{out}(\eta, X) = p_0(\eta) + p_1(\eta) \cdot X + \frac{p_2(\eta)}{X} \tag{6.7}$$

A different fit is done for each different type of particle: electron, unconverted photon and converted photon.

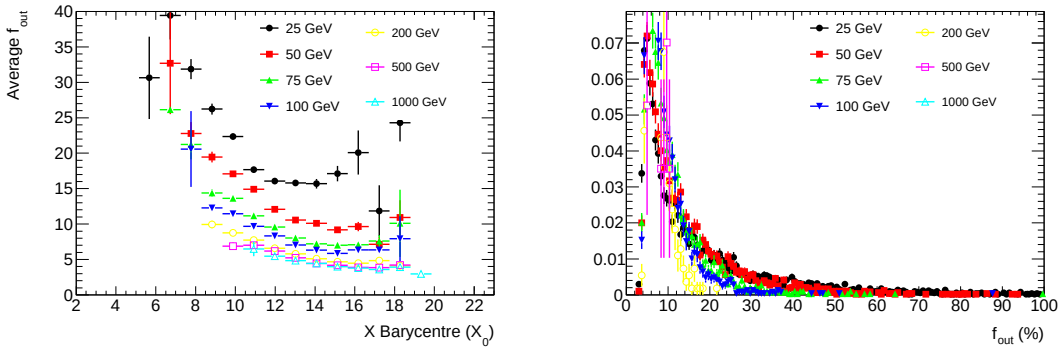

(a) *Average f_{out} vs X* (b) *f_{out} for electrons with $10 < X < 12$*

Figure 6.4: *f_{out} and f_{out} vs X for electrons at $\eta = 1.7125$*

It should be notice that the approach of taking MPV of the f_{out} distribution it is sufficient to properly recover the energy deposited outside the cluster for those events with f_{out} values around the peak of the distributions. For events with f_{out} values corresponding to the tails the Calibration Hits Method will underestimate this correction leading to energy distributions with low energy tail. The effect of this tails will be studied in detail in subsequent sections.

In this procedure it was assumed that the particle is incident at the center of the central cell of the cluster. This is obviously not always the case and must be taken into account in a second step of the Calorimeter Reconstruction Algorithm. In order to be more clear, figure 6.7 shows the obseved η (left plot) and ϕ modulation during beam tests. The η modulation shows clearly the increase of energy underestimation when the incident electron hits farther away from the center of the cluster. In the ϕ modulation plot a combination of leakage and irregularity effect due to the accordion geometry is shown. Notice that these corrections are applied in a step after the

[4] For converted photons the energy independence is only partially recovered. The angular separation in a pair creation is typically $\sim m_0c^2/E$ with E the energy of the incident photon. Hence, pairs created by low energy photons could be very separated from each other. This increases the probability for one of the electrons to miss the defined cluster.

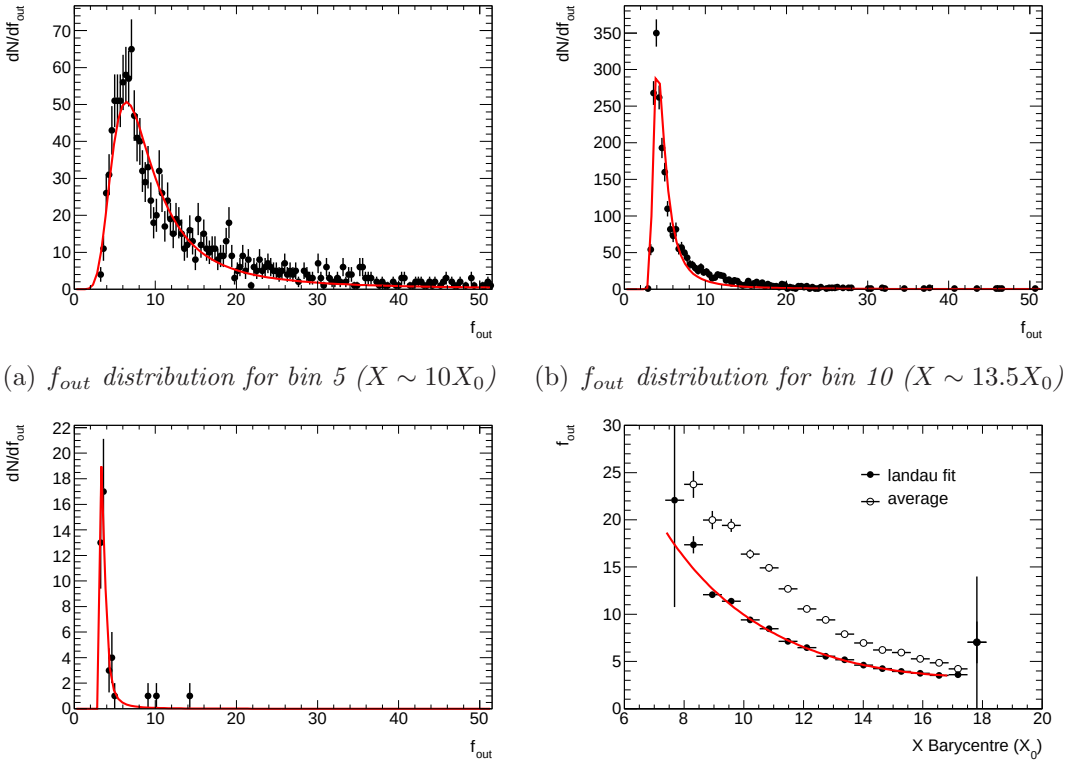

(a) f_{out} *distribution for bin 5 (*$X \sim 10X_0$*)*

(b) f_{out} *distribution for bin 10 (*$X \sim 13.5X_0$*)*

(c) f_{out} *distribution for bin 15 (*$X \sim 17X_0$*)*

(d) *Average and MPV of* f_{out} *vs* X

Figure 6.5: f_{out} *distributions at three* X *bins and average and MVP of the distributions vs* X *for convertend photons hitting a 5x5 cluster centered at* $\eta = 1.7125$

calibration hits method. Therefore, all results presented in subsequent sections still need to be corrected by those modulations.

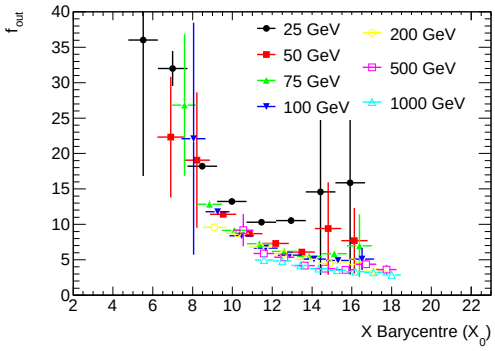

(a) *electrons*

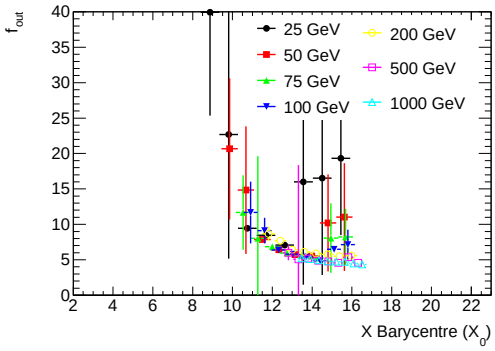

(b) *electrons*

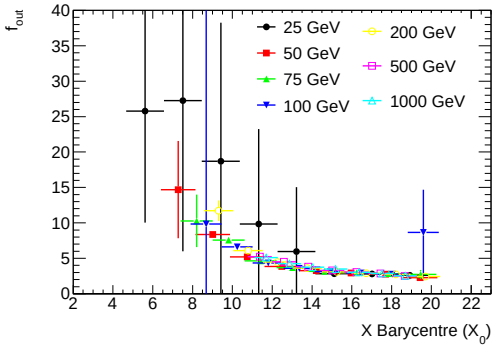

(c) *unconverted photons*

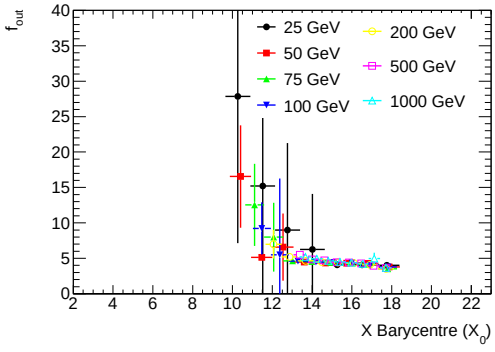

(d) *unconverted photons*

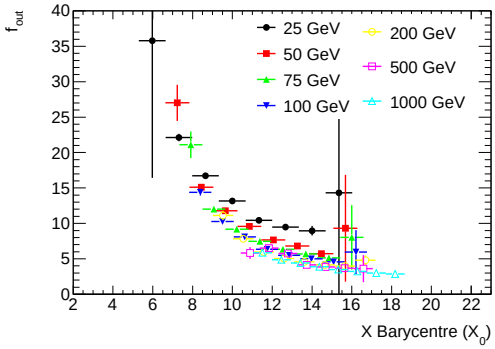

(e) converted photons

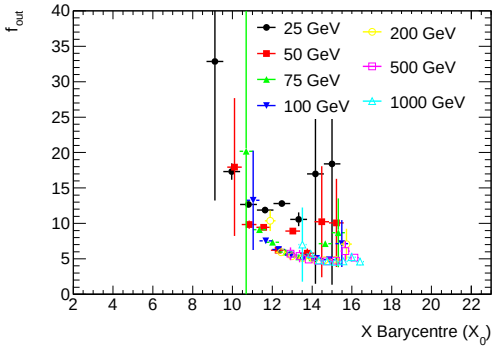

(f) converted photons

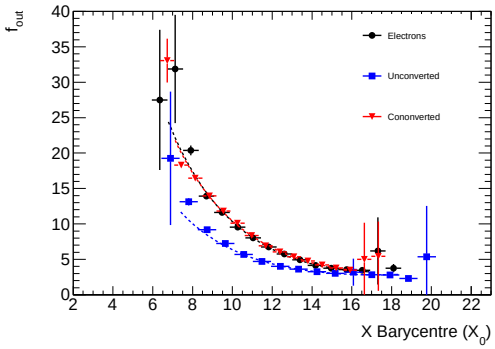

(g) Energy averaged

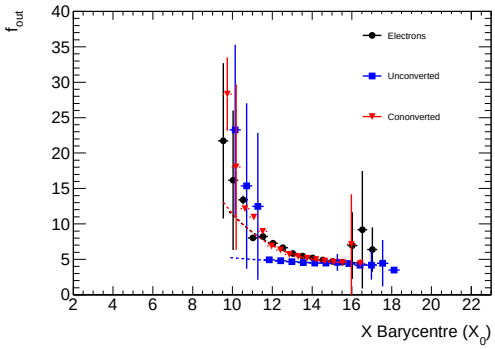

(h) Energy averaged

Figure 6.6: *f_{out} vs X for the various energies and energy averaged at $\eta = 1.6375$ (left) and $\eta = 1.9125$ (right)*

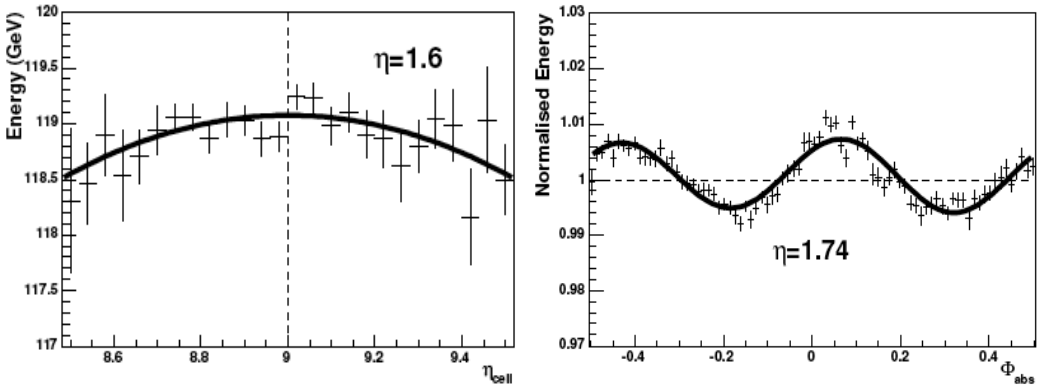

(a) η modulation of the energy scale (b) *phi* modulation of the energy scale

Figure 6.7: η and ϕ modulations observed on the beam test.

6.5 Corrections for longitudinal leakage

The small fraction of the energy that is deposited behind the calorimeter is computed by applying to the reconstructed energy in the calorimeter the factor f_{leak}, defined as:

$$f_{leak} = \frac{E_{leak}}{E_{acc}} \tag{6.8}$$

where E_{leak} accounts for all the energy deposited behind the calorimeter and E_{acc} for all the energy depositions in the calorimeter (active and pasive materials), i.e.:

$$E_{acc} = \sum_{i=1}^{3} E^i_{lar} + E^i_{abs} \tag{6.9}$$

As shown in figure (6.8 a, b and c), f_{leak} is again fairly energy independent when it is parameterized as a function of the longitudinal barycenter of the shower.

The weights that correct for the longitudinal leakage are extracted by fitting the energy averaged f_{leak} distributions , for every type of particle, using the following function:

$$f_{leak}(\eta, X) = l_0(\eta) \cdot X + l_1(\eta) \cdot e^X \tag{6.10}$$

Figure 6.8 g and h give an idea of the quality of the fits. The η dependence of these parameters reflects the variation of the calorimeter depth with η.

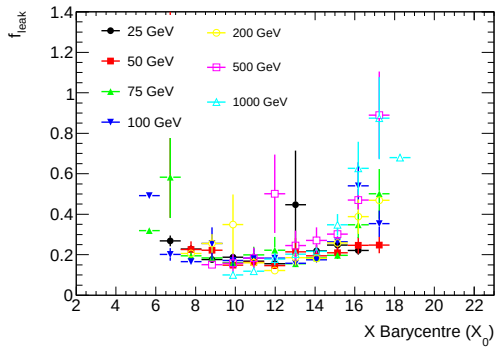

(a) *electrons*

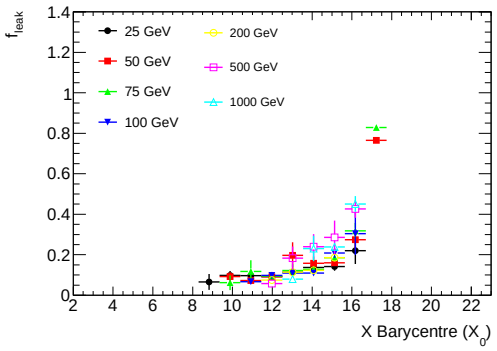

(b) *electrons*

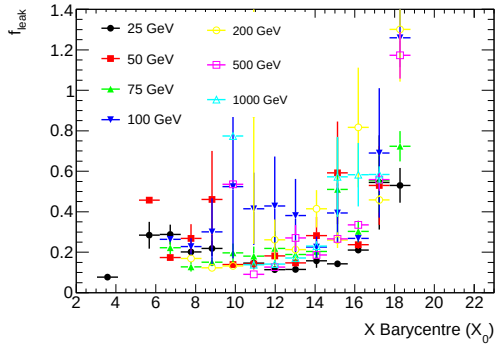

(c) *unconverted photons*

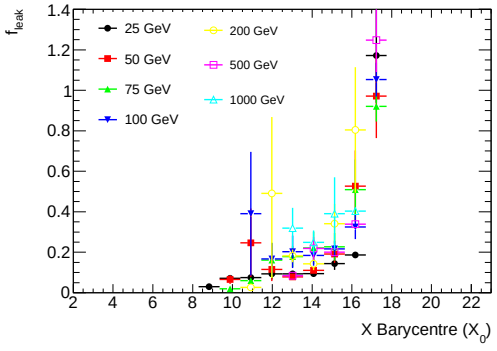

(d) *unconverted photons*

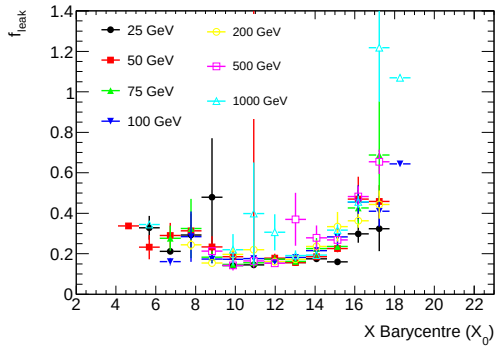

(e) converted photons

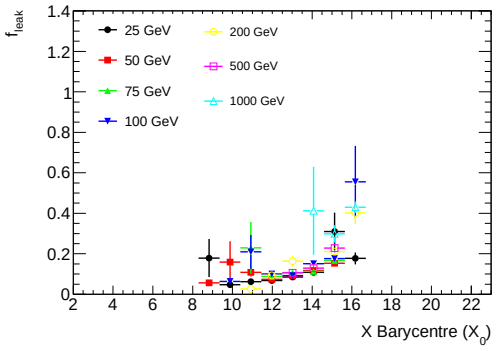

(f) converted photons

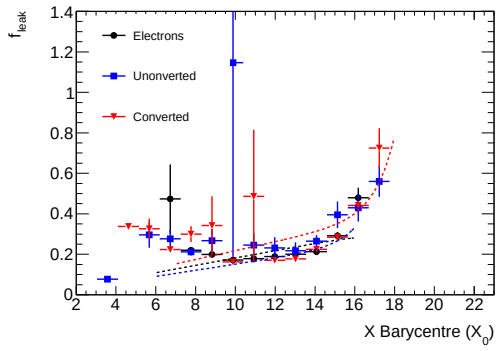

(g) Energy averaged

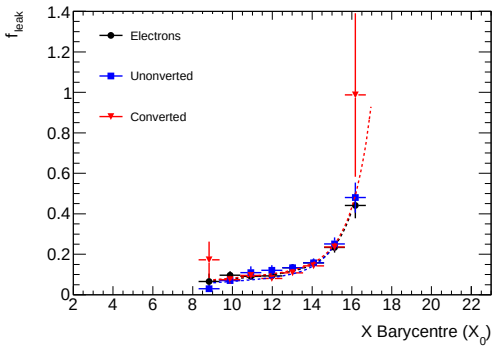

(h) Energy averaged

Figure 6.8: *f_{leak} correction as a function of the longitudinal barycenter of the shower at $\eta = 1.6375$ and $\eta = 1.9125$*

6.6 Corrections for the energy loss in front of the Calorimeter

In [34] is demonstrated that the energy lost in front of the calorimeter, in which inner detector, cryostats boards, cables, presampler and material between presampler and front layer are included, can be successfully parameterized as a function of the energy deposited in the presampler. However, the ATLAS EMEC is only instrumented with a presampler for $1.5 < |\eta| < 1.8$. In order to calibrate the EMEC region in which the presampler is absent a new procedure had to be developed.

6.6.1 Region with presampler $|\eta| < 1.8$

As in the case of f_{out} a special treatment of the distributions of energy in front of the calorimeter per presample energy (E_{ps}) bin was done. In figure 6.9 a, b and c we can see the energy deposited in front of the calorimeter for $50GeV$ in three bins for the energy in the presampler. These three bins are centered at $3GeV$, $4.5GeV$ and $7GeV$ and they have size of $\Delta E_{ps} \sim 0.8GeV$. The distributions are mostly gaussian but they present a tail at high values of $E_{infront}$. The treatment consist on taking the most probable value (MPV) of the distributions (instead of the average value) by using a gaussian fit in the interval $(1.0 \cdot \sigma, 1.5 \cdot \sigma)$ around the maximum. The fit function is superimposed to the distributions. Figure 6.9 (d) shows the difference between considering the most probable value extracted from the gaussian fit and the mean of the distribution. The proper choice in this approach has an impact on the energy resolution and energy scale. The MPV is more stable than the mean, however it underestimate (a bit more than the mean) the energy for those events with $E_{infront}$ in the tail of the distribution. This will reflect on low energy tails in the total energy reconstruction.

The energy in the dead material in front of the calorimeter, obtained as the most probable value described above, is represented versus the energy deposited in the presampler at $\eta = 1.6375$ in figure 6.10. The seven different plots correspond to the seven different particle energies.

The correlation observed between the energy deposited in front of the calorimeter and the energy deposited in the presampler is shown in figure 6.10 for all three types of particles. The adopted parameterization is a second degree polimomial:

$$E_{front} = a + b \cdot E_{ps} + c \cdot E_{ps}^2 \tag{6.11}$$

The fit includes a quadratic term, which is absent in the EMB, due to the larger variation of material in the EMEC. A clear dependence on the incoming particle is observed. Electrons (or pairs coming from a photon conversion), having a higher probability of interaction with matter deposit a higher fraction of its energy in the upstream material. Hence the procedure must be done independently for each type of particle. The correlation between $E_{infront}$ and E_{ps} is strongly energy dependent. Hence coefficients a, b and c in equation 6.11 depend on the energy of the incoming particle. Since the true energy of the particle is unknown, the coefficients are pa-

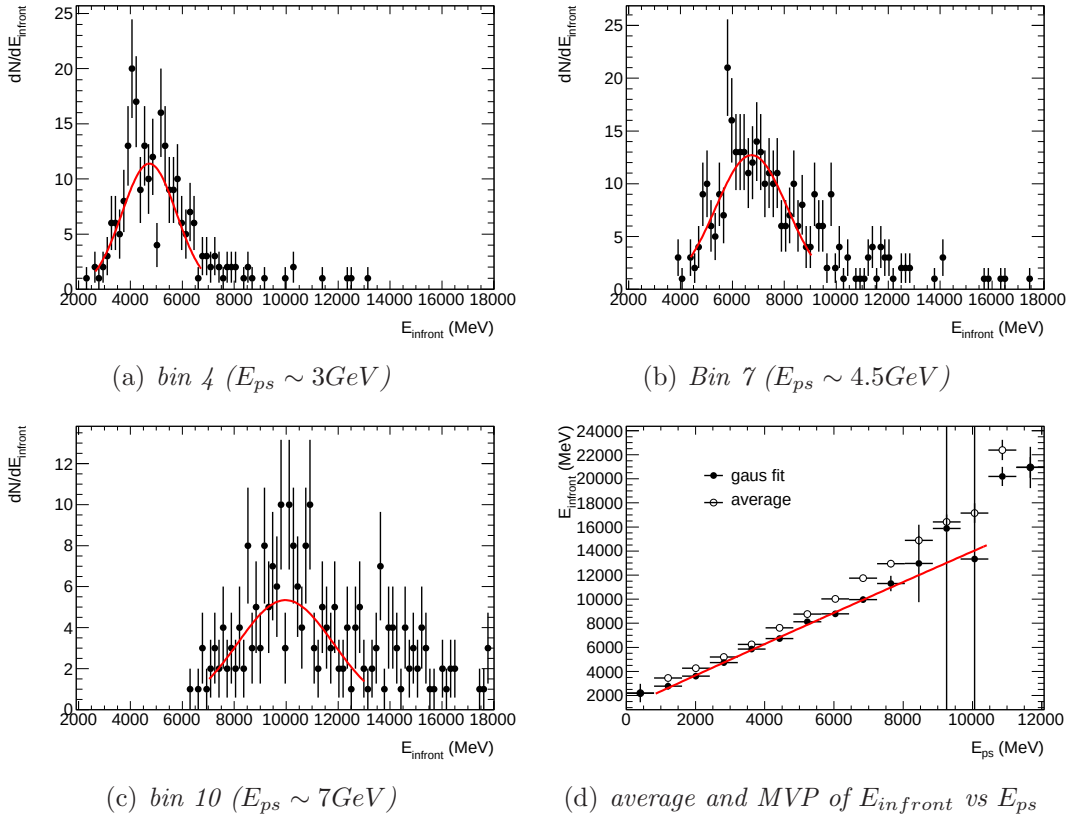

(a) *bin 4 ($E_{ps} \sim 3GeV$)* (b) *Bin 7 ($E_{ps} \sim 4.5GeV$)*

(c) *bin 10 ($E_{ps} \sim 7GeV$)* (d) *average and MVP of $E_{infront}$ vs E_{ps}*

Figure 6.9: *E_{front} distributions at three E_{ps} bins and average and MVP of the distributions vs E_{ps} for electrons hitting a 5x5 cluster centered at $\eta = 1.6785$*

rameterized as a function of the previously reconstructed energy in the calorimeter E_{calo}. Such dependence is represented in figure 6.11. The points are fitted to the following functions:

$$a(E_{calo}, \eta) = O_0(\eta) + O_1(\eta) \cdot E_{calo} + O_2(\eta) \cdot \sqrt{(}E_{calo}) \quad (6.12)$$

$$b(E_{calo}, \eta) = S_0(\eta) + S_1(\eta) \cdot Log(E_{calo}) + S_2(\eta) \cdot \sqrt{(}E_{calo}) \quad (6.13)$$

$$c(E_{calo}, \eta) = R_0(\eta) + R_1(\eta) \cdot E_{calo} - \frac{R_2}{E_{calo}^2} \quad (6.14)$$

The fact that the offset a is not negligible means that there may be energy lost in the material in front and however no energy deposit in the presampler. This effect has two sources:

- the material between the presampler and the front compartment of the calorimeter (electronics and cables) is considered as material in front of the calorimeter but it is behind the presampler.

- absorption of very low energy electrons and photons in the early shower.

Acording to equation 6.14 this offsets increases with E_{calo}.

Parameter b is kind of a "gain" factor to convert from E_{ps} signal to $E_{infront}$. Parameter c takes into account small non-linearities or saturation effects.

6.6.2 Region without presampler $|\eta| < 1.8$

In [34] is shown that the energy lost in front of the calorimeter can be corrected by using the estimated barycentre of the electromagnetic shower X which is expected to change by the presence of upstream material due to the early start of the shower. More energy lost in the upstream material would mean less value of X and vice versa. Figure 6.12 represents the energy lost in front as a function of X for the various energies and the three types of particle, from where it can be inferred the sensitivity of X to the energy losses in the upstream material. Note that the limits on the abcisa differ from those shown in figure 6.10 by a factor 4. This reflect the difference in the amount of upstream material. The relation between $E_{infront}$ and X can be described by:

$$E_{front} = a(E_{calo}, \eta) + b(E_{calo}, \eta) \cdot X + c(E_{calo}, \eta) \cdot X^2 \tag{6.15}$$

The dependence of a, b and c with E_{calo} are shown in figure 6.13. In contrast to the equivalent parameters in the region with presampler, discussed in the previous section, this energy dependences is more simple and can be parameterized using second order polynomials.

6.7 Summary

The procedure to extract the coefficients that will be applied to reconstruct the energy have been explained. At the end of the procedure we have a set coefficients that applied to E_{ps} and E_i $(i = 1, 2, 3)$ will produce an output E_{reco}. Not that the relation $(E_{ps}, E_1, E_2, E_3) \rightarrow E_{reco}$ is univocal and the fluctuations on E_{reco} are determined by the stochastic nature of the input variables.

All the corrections are computed by using the most probable or average values of the various distribution. The magnitudes f_{out} and f_{calo} depend on the size of the considered cluster. Hence, a different set of coefficient for every cluster size is computed. The correction $E_{infront}$ and f_{leak} are both considered cluster size independents. For the sake of clarity, the corrections of the Calibration Hits Method are summarized in table 6.3.

Correction	$n0$ params/cluster	Cl dependence	total $n0$ params
$E_{infront}$	9	no ($\times 1$)	9
E_{calo}	6	yes ($\times 3$)	18
E_{behind}	2	no ($\times 1$)	2
TOTAL	17		29

Table 6.3: *Summary of the parameters used by the calibration hits method in each correction. The parameters corresponding to $E_{infront}$ refer a, b and c to equation 6.11 (equation 6.15 for $\eta > 1.8$)). E_{calo} include the parameters of both f_{calo} (equation 6.6) and f_{out} (equation 6.7). Those parameters need to be computed for the three different cluster sizes. E_{behind} includes the three paramaters in equation 6.10.*

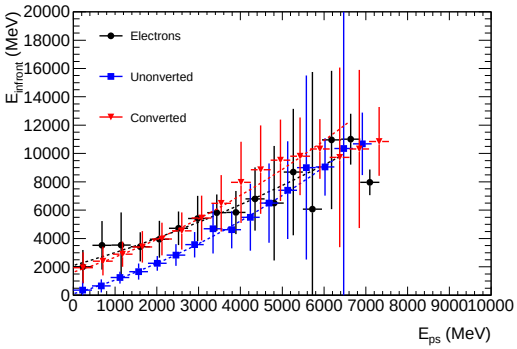

(a) *25 GeV particles*

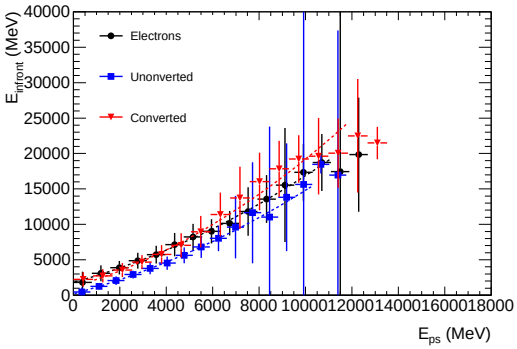

(b) *50 GeV particles*

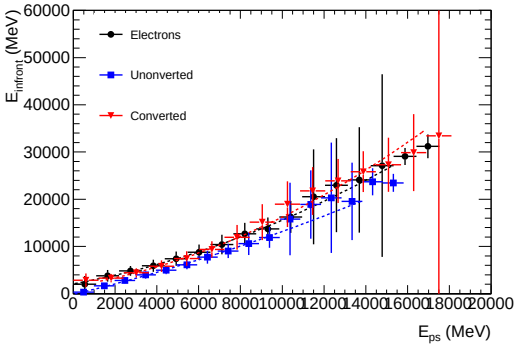

(c) *75 GeV particles*

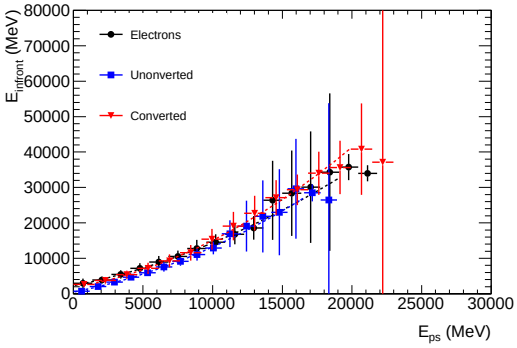

(d) *100 GeV particles*

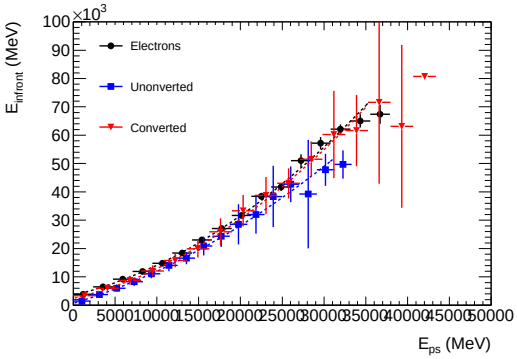

(e) *200 GeV particles*

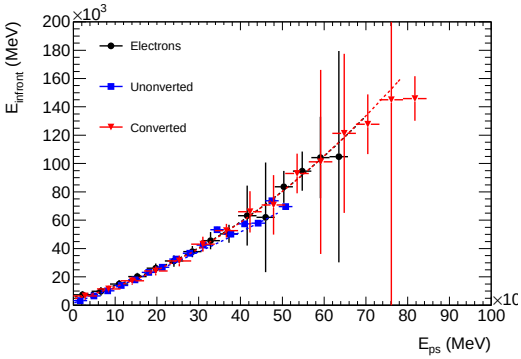

(f) *500 GeV particles*

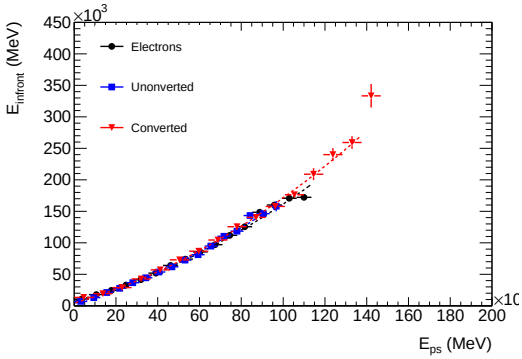

(g) *1000 GeV particles*

Figure 6.10: *$E_{infront}$ vs E_{ps} for different energies and all type of particles at* $\eta = 1.6375$

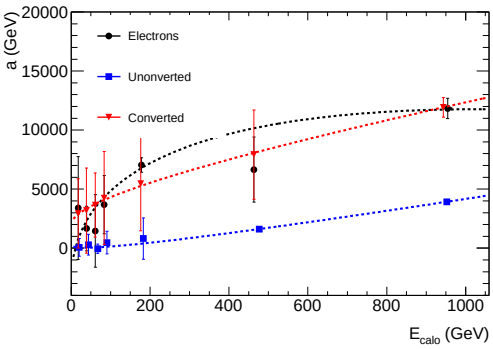

(a) *a versus* E_{calo}

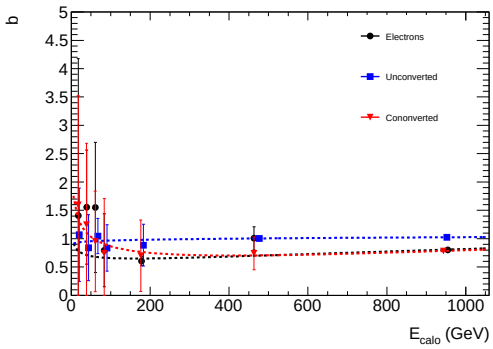

(b) *b versus* E_{calo}

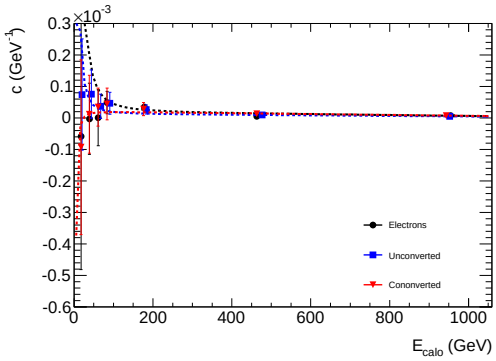

(c) *c versus* E_{calo}

Figure 6.11: *a, b and c parameters in eq. 6.11 versus* E_{calo} *at* $\eta = 1.6375$

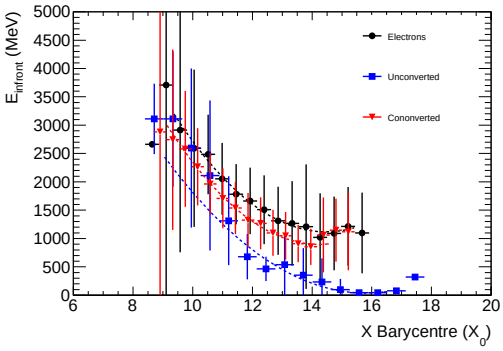

(a) *25 GeV particles*

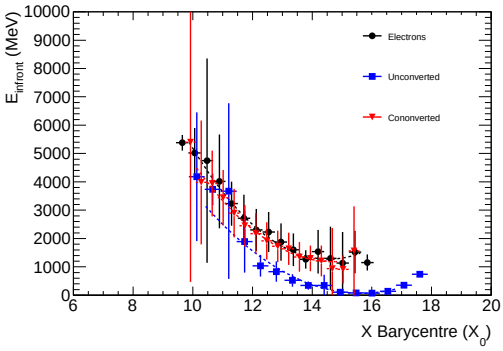

(b) *50 GeV particles*

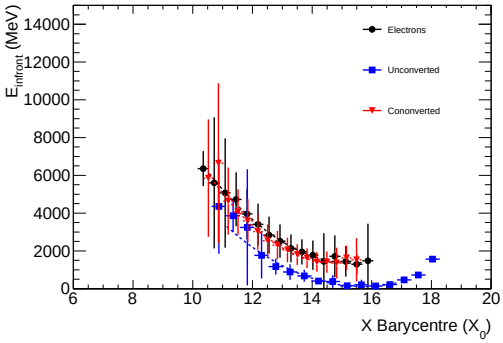

(c) *75 GeV particles*

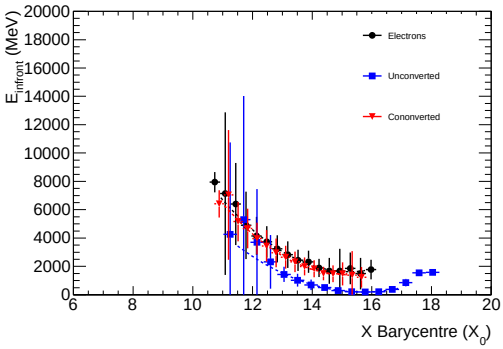

(d) *100 GeV particles*

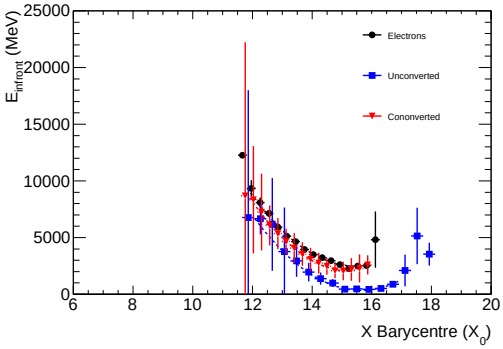

(e) *200 GeV particles*

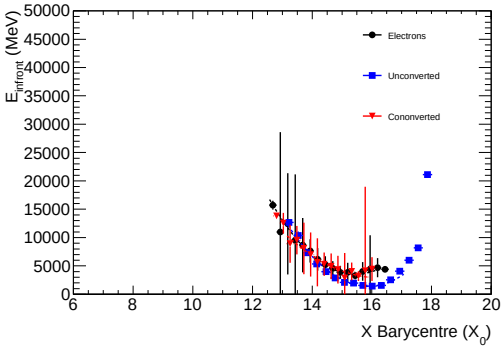

(f) *500 GeV particles*

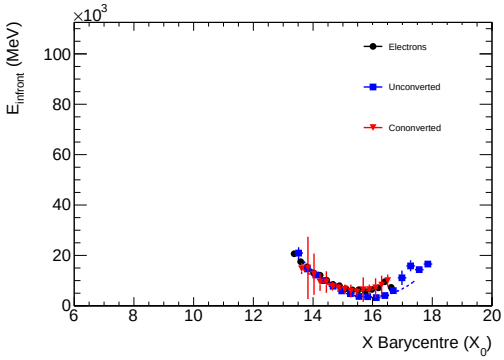

(g) *1000 GeV particles*

Figure 6.12: *$E_{infront}$ vs X for different energies and all type of particles at* $\eta = 1.9125$

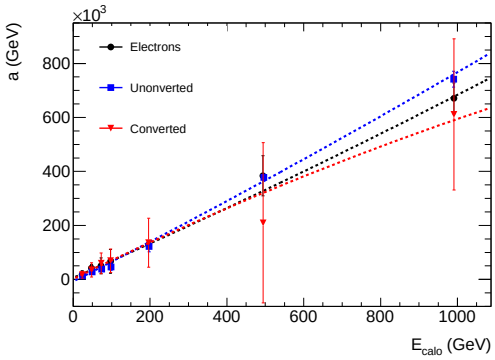

(a) *a versus* E_{calo}

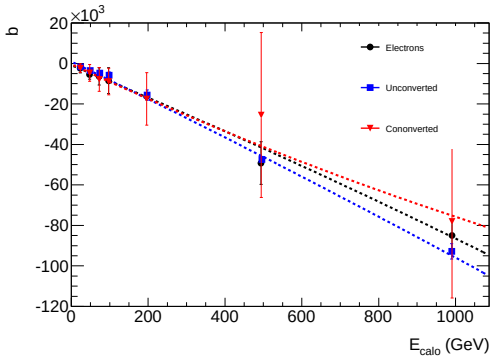

(b) *b versus* E_{calo}

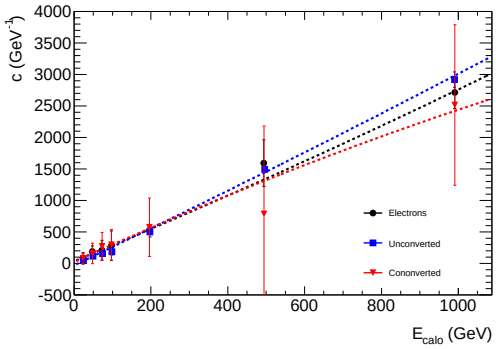

(c) *c versus* E_{calo}

Figure 6.13: *a, b and c parameters in eq. 6.15 versus* E_{calo} *at* $\eta = 1.9125$

Chapter 7

Results

The set of coefficients or parameters extracted in previous chapter are applied in Monte Carlo samples of single particles to check the peformance of the method in terms of energy resolution, linearity, uniformity and energy scale. The ideal performance of the Calibration Hits Method wanted to be checked, hence neither electronic noise or pile-up noise was included in the simulation. Some systematics affecting the CHM are also studied in this chapter.

7.1 Energy resolution and linearity

The energy of the incoming particle is reconstructed using the procedure described in chapter 4, $E_{reco} = E_{infront} + E_{calo} + E_{behind}$, where the three different terms include the coefficients for the needed corrections. Unless otherwise stated, all the results presented correspond to electrons and photons that satisfy a Tight IsEm quality cut (See Apendix A). As an example, the distributions of E_{reco} are represented in figures 7.1 and 7.2 for the various energies and for particles hitting a cluster centered at $\eta = 1.6375$ and $\eta = 1.9125$ respectively. Those two η positions were chosen in order to give an idea of how the calibration hits method works when the energy loss in the upstream material is corrected by using the presampler or the barycentre of the electromagnetic shower (η below and above 1.8 respectively).

Under ideal conditions, perfect gaussian distributions for E_{reco} are expected. However, a low energy tail is observed at low generated energies. This is a combination of the effect of the upstream material and the lateral leakage. The upstream material has also a manifest consequence on the width of the distributions. Energy profiles for unconverted photons are narrower since, as discussed in previous sections, the interaction photon-matter is less probable than interactions electron-matter. However, the effect becomes clearer by comparing the distribution, corresponding to particles of the same energy, in the two different η positions. The distributions corresponding to a cluster centered at $\eta = 1.6375$ are obviously wider since the amount of upstream material in that position is about $1.5X_0$ bigger. The effect of both contributions, lateral leakage and upstream material, becomes less significant at the highest energies. If we focus on the profiles for one particular value

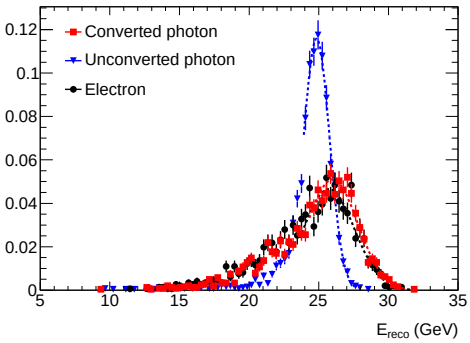

(a) $E = 25GeV$

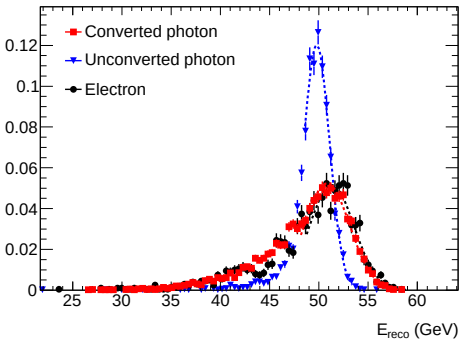

(b) $E = 50GeV$

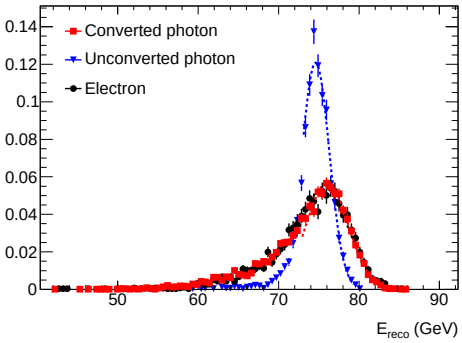

(c) $E = 75GeV$

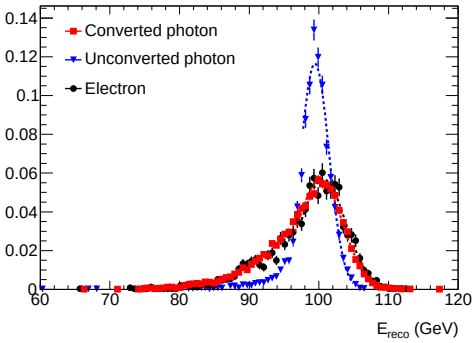

(d) $E = 100GeV$

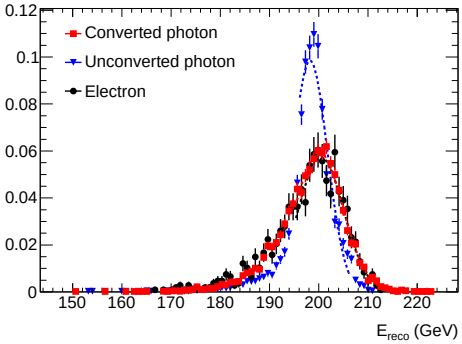

(e) $E = 200GeV$

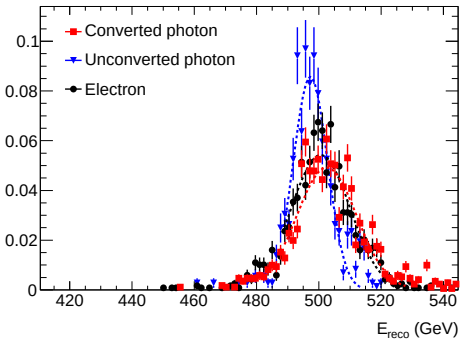

(f) $E = 500GeV$

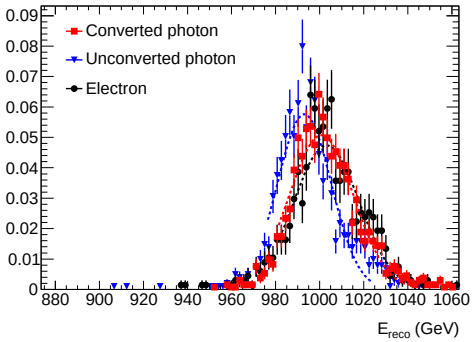

(g) $E = 1000GeV$

Figure 7.1: Reconstructed energies at $\eta = 1.6375$

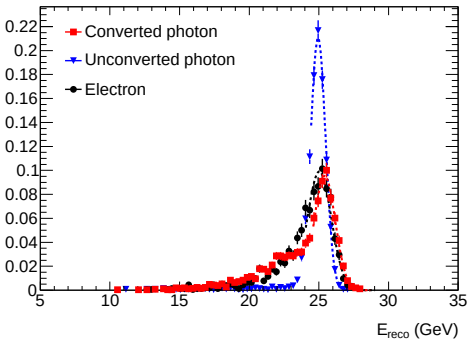

(a) $E = 25GeV$

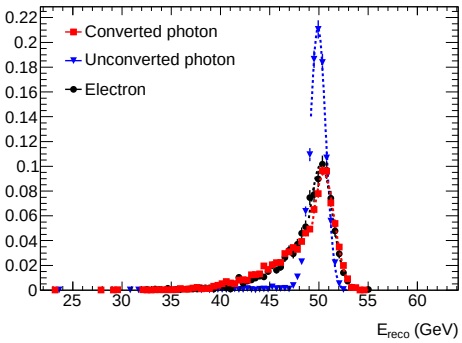

(b) $E = 50GeV$

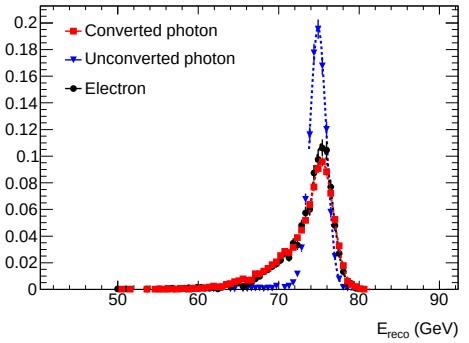

(c) $E = 75GeV$

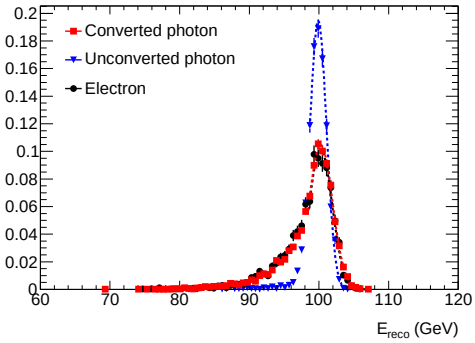

(d) $E = 100GeV$

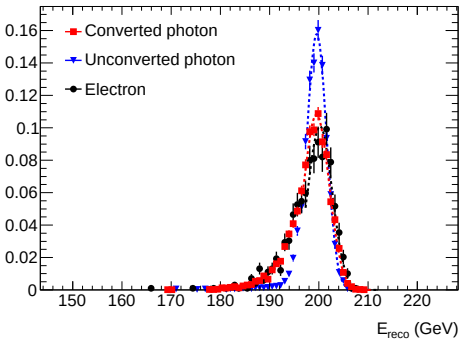

(e) $E = 200GeV$

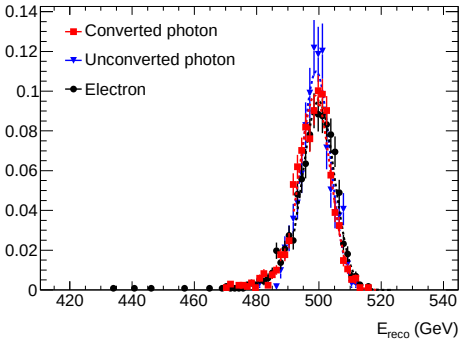

(f) $E = 500GeV$

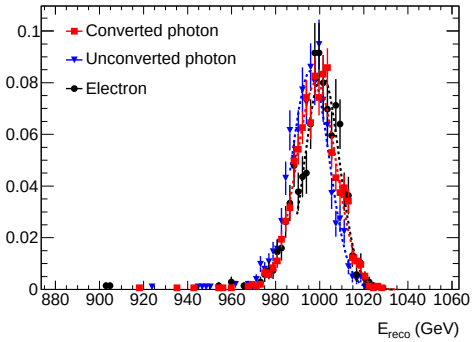

(g) $E = 1000GeV$

Figure 7.2: Reconstructed energies at $\eta = 1.9125$

of η, the distributions are narrower and they have a smaller fraction of events in the low energy tail as the energy increases. This will be studied in more detail in section 7.3. Another appreciable feature is a high energy tail appearing only at very high energy and low η, clearly shown in figure 7.1 g. In order to clarify this point figure 7.3 (a) represents a scatter plot of f_{calo} versus the barycenter of the Shower for all clusters produced by unconverted photons in the region $1.55 < \eta < 1.65$. By design of the Endcap EM calorimeter, the Liquid Argon gap size increases with depth (z-direction) for any fixed η value. In the selected pseudorapidity region of Figure 7.3 (a), the variation of the LAr gap from the front layer to the back layer is maximum. It is observed that the values of f_{calo} are separated in two populations for high X, namely at $X > 16\ X_0$. Figure 7.3 (b) shows the f_{calo} distributions for two sub-samples: events with $X > 16\ X_0$ and events with $X \leq 16\ X_0$. The distribution corresponding to $X > 16\ X_0$ manifests two peaks at ~ 1 and ~ 0.95. Particles with a late cascade, $X > 16\ X_0$, deposit more energy in the LAr gaps, due to its higher thickness, than particles with an early shower, which implies a smaller value of f_{calo} (see Equation 6.4). Although a parameterisation in terms of the depth X should take this into account there is an intrinsic bias on the barycentre of the shower as defined in the previous chapter. Since the middle layer is designed to contain most of the energy in the shower, X is biased towards the center of the middle compartment and it is not very sensitive to small variations in the energy deposited in the back layer. Hence two peaks are observed in the f_{calo} for $X > 16\ X_0$.

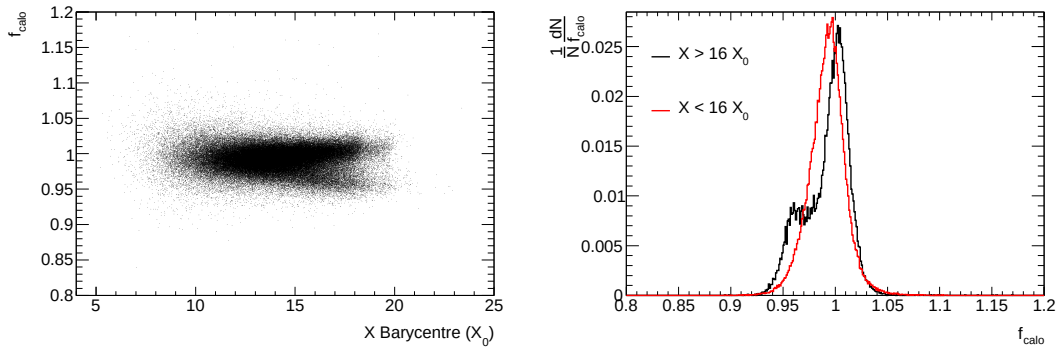

(a) f_{calo} vs X (b) $E = 50GeV$

Figure 7.3: f_{calo} ditributions for $1.55 < \eta < 1.65$

The results shown in subsequent sections are based in an iterative and asymetric gaussian fit. The first iteration is used to roughly get the mean value μ and the standard deviation σ of the distributions and the fit is performed within the limits $(E_{true} - 4 \times 25\%\sqrt{E_{true}}, E_{true} + 6 \times 25\%\sqrt{E_{true}})$. Such a large range was chosen in order to take into account mostly the whole distribution, with independence on energy and η. The next three iterations use an asymetric fit in the interval $(\mu_{i-1} - \sigma_{i-1}, \mu_{i-1} + 2.5\sigma_{i-1})$ where μ_{i-1} and σ_{i-1} represent the mean value and standard deviation of the asymetric gaussian fit in the previous iteration.

7.1.1 Linearity

The fitted mean of the reconstructed energy as a function of the generated energy is represented in figure (7.4) for all type of particles and for two values of η, namely: 1.6375 (belongs to region with presampler) and 1.9125 (belongs to region without presampler). Apparently for both η values the relation is linear. However, to check the deviation from a linear relation at the per mil level, the points are fitted using a first degree polinomial and the following quatity is calculated for each point m_i , $i = 1, \ldots, 7$:

$$\Delta m_i = \frac{m_i - E_{fit}}{E_{fit}}$$

where $E_{fit} = e_1 \cdot E_{true} + e_2$ being e_1 and e_2 the parameters of the fit.

e_1	$\eta = 1.6375$	$\eta = 1.9125$
electrons	1.0006 ± 0.0006	1.0005 ± 0.0003
unconverted	0.9936 ± 0.0004	0.9977 ± 0.0003
converted	0.9997 ± 0.0004	0.9967 ± 0.0002

Table 7.1: *Parameter e_1 from the linear fit at $\eta = 1.6375$ and $\eta = 1.9125$ for the different type of particles*

e_2 (GeV)	$\eta = 1.6375$	$\eta = 1.9125$
electrons	0.7705 ± 0.0740	0.1245 ± 0.0355
unconverted	0.0466 ± 0.0319	0.0514 ± 0.0225
converted	0.7305 ± 0.0484	0.5524 ± 0.0231

Table 7.2: *Parameter e_2 from the linear fit at $\eta = 1.6375$ and $\eta = 1.9125$ for the different type of particles*

The values of e_2, represented as a funtion of η in figure 7.5 (a), are close to zero, but not compatible with this value. This fact indicates that the Calibration Hits Method is a little biased at very low energies. From the fits corresponding to the two shown cells (tables 7.1 for e_1 and 7.2 for e_2) electrons get the highest value at $\eta = 1.6375$, since they are more affected by the presence of the upstream material, whereas converted photons get the higher value at $\eta = 1.9125$. At this point, the dominant correction is the lateral leakage correction which affects more to converted photons since the axial magnetic field separate the pair e^+e^- coming from the conversion. The values of e_1 (figure 7.5 b) are close to one, this parameter being related with the energy scale (E_{reco}/E) of the calorimeter.

In figure 7.6 the quantities Δm_i as a function of the generated energy (E_{true}) are shown. The left (right) row correspond to $\eta = 1.6375$ ($\eta = 1.9125$). At $\eta = 1.6375$ the deviation from linearity is below 0.5 % except for the low energies for electrons

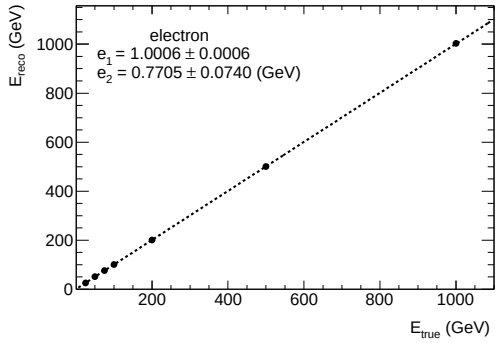

(a) Electrons at $\eta = 1.6375$

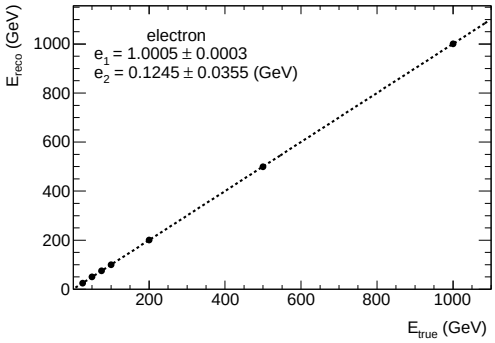

(b) Electrons $\eta = 1.9125$

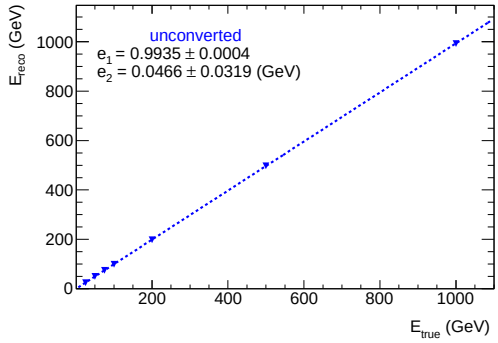

(c) Unconverted γ at $\eta = 1.6375$

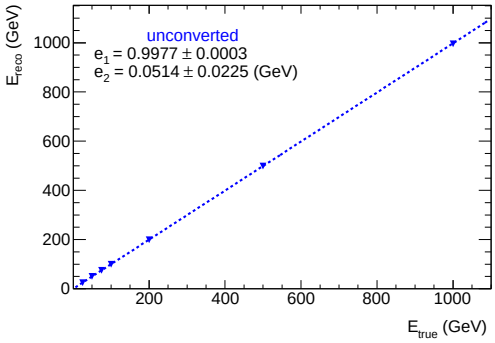

(d) Unconverted γ at $\eta = 1.9125$

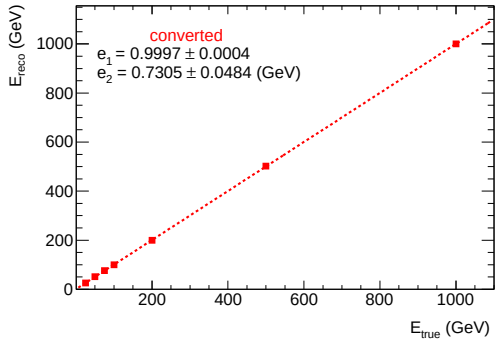

(e) Converted γ at $\eta = 1.6375$

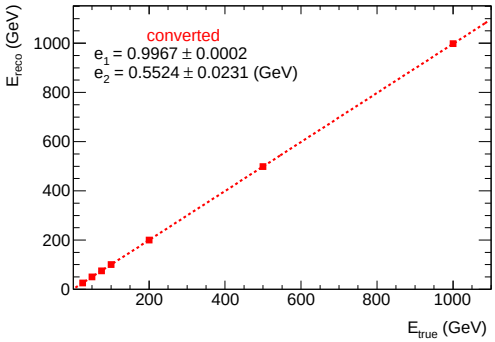

(f) Converted γ at $\eta = 1.9125$

Figure 7.4: Reconstructed energy versus true energy superimposed with a first degree polinomial fit

and converted photons, which are about 1.0 % . At $\eta = 1.9125$ the linearity is better with all particles and all energies within 0.5%.

To study the uniformity of the linearity as a function of η, one quantity representing the deviation from linearity at a given pseudorapidity must be defined. One candidate is the maximum deviation from linearity defined as:

$$L = \Delta m_k$$

where k corresponds to the index which makes $|\Delta m_i|$ maximum.

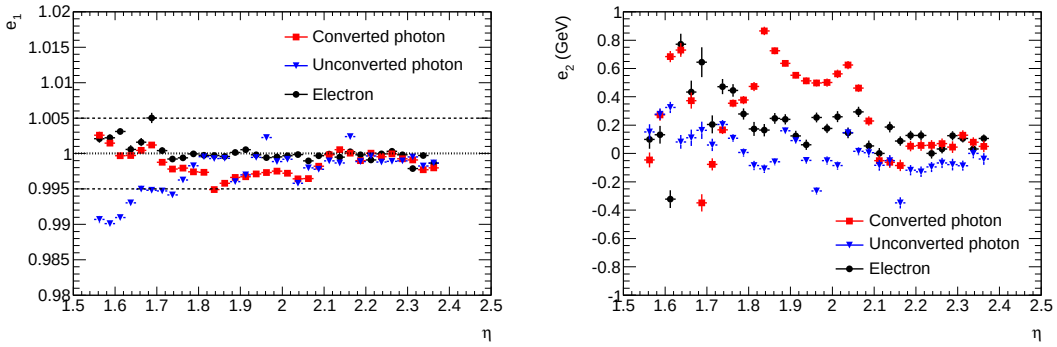

(a) e_1 versus η (b) e_2 versus η

Figure 7.5: Uniformity of the parameters e_1 and e_2

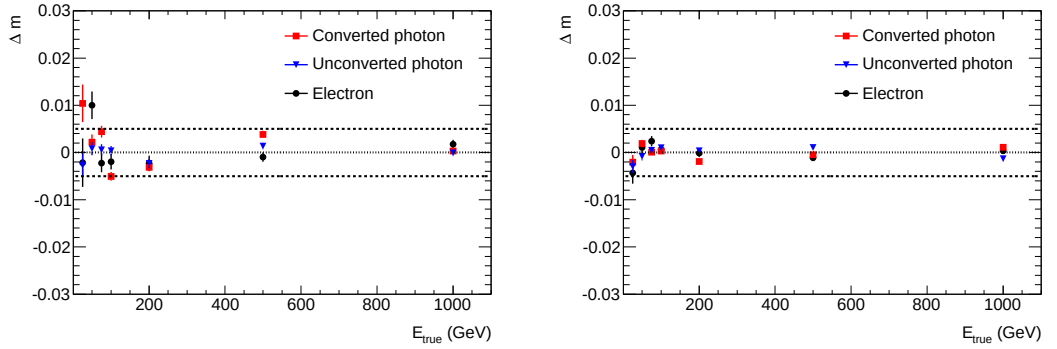

(a) $\eta = 1.6375$ (b) $\eta = 1.9125$

Figure 7.6: Δm versus energy

This quantity L is shown as a funtion of η in figure (7.7). L is within 0.5 % for all particles at $\eta > 1.8$ except for converted photons with $\eta > 2.1$. Due to the structure of the inner detector, the conversions at $\eta > 2.1$ occur only at radii lower than 40 cm. Conversions closer to the interaction point are also harder to calibrate since the pair e^+e^- travel through the whole inner detector feeling the magnetic field and separating from each other. The effect of conversions happening at different radii in the linearity, energy scale and energy resolution will be explained in detail in section 7.4. For $\eta < 1.8$ converted photons are compatible with 2.5% linearity whereas electrons are within 1% except for four cells that reach up to 3 %. This broad deviation from perfect linearity is due to the large amount of upstream material in front of the calorimeter, as we can see from the fact that unconverted photons are not affected, being within 0.5 %.

Finally, note that the last five calorimeter cells ($\eta > 2.375$) are not represented in the previous plots. As stated before, all particles should satisfy a Tight cut which requires a reconstructed track pointing to a calorimeter cluster. The efficiency of this cuts decreases with η as the tracking becomes less efficient and no events (or very few) survive this condition for very high η. Hence, these calorimeter cells will be independently analyzed in section 7.5.

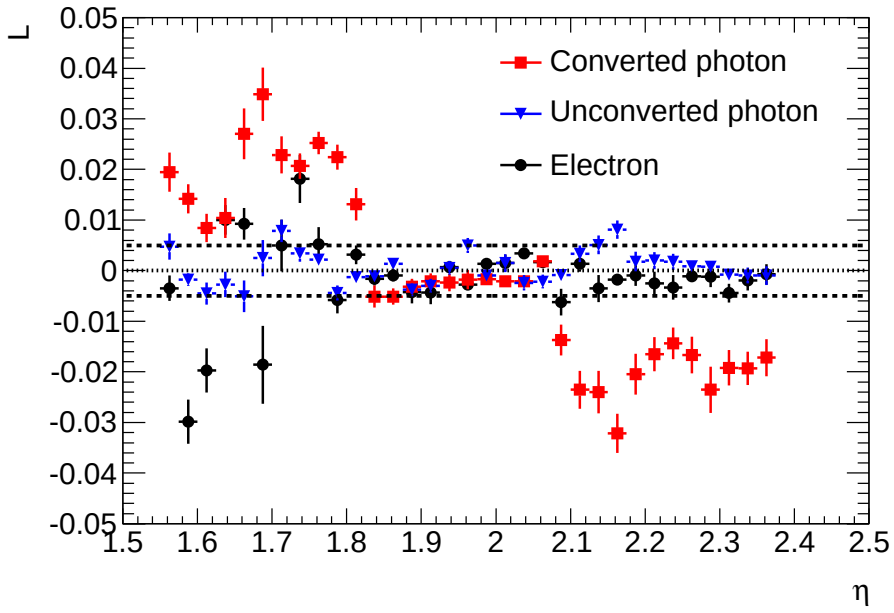

Figure 7.7: *Maximum deviation from linearity versus η.*

7.1.2 Energy resolution

As seen in chapter 4 the energy resolution $\frac{\sigma}{m}$ is parameterized as:

$$\frac{\sigma(E)}{\mu(E)} = \frac{b}{\sqrt{E(GeV)}} \oplus c \tag{7.1}$$

where b and c are the sampling and constant term respectively and $\oplus$ means the quadratic sum. As explained in previous sections, this document presents the performance of the Calibration Hits method in ideal conditions. Hence, no electronic or pile-up noise was included in the simulation. Furthermore, the results showed in this section are not corrected by the effect of η and ϕ modulations (see section 6.4) which mostly have an effect on the constant term of the resolution.

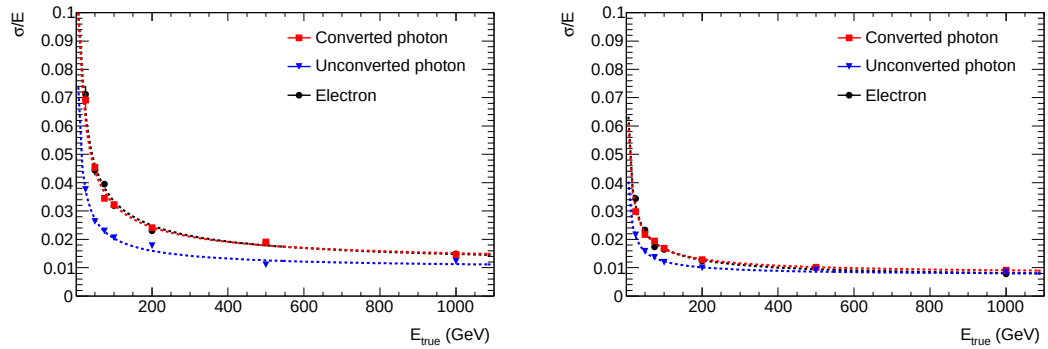

(a) $\eta = 1.6375$ (b) $\eta = 1.9125$

Figure 7.8: Resolution versus energy

In figure 7.8 the energy resolution as a function of the generated energy (E_{true}) is shown for the three type of particles . The left (right) plot correspond to $\eta = 1.6375$ ($\eta = 1.9125$).

b (%)	$\eta = 1.6375$	$\eta = 1.9125$
electrons	31.6434 ± 0.6317	15.4087 ± 0.3389
unconverted	17.8985 ± 0.3746	9.7216 ± 0.2206
converted	23.5457 ± 0.3977	14.7783 ± 0.7802

Table 7.3: *Sampling term at* $\eta = 1.6375$ *and* $\eta = 1.9125$ *for the different type of particles*

c (%)	$\eta = 1.6375$	$\eta = 1.9125$
electrons	1.0949 ± 0.0886	0.6499 ± 0.0381
unconverted	0.9733 ± 0.0543	0.7450 ± 0.0273
converted	1.1783 ± 0.0624	0.7802 ± 0.0235

Table 7.4: *Constant term at* $\eta = 1.6375$ *and* $\eta = 1.9125$ *for the different type of particles*

In the region around $\eta = 1.6$ the dead material in front has a higher value and larger variation than in the region about $\eta = 1.9$. This fact reflects on the different values obtained for the resolution, much better at $\eta = 1.9$.

To study the uniformity of the energy resolution the sampling and constant terms are represented as a function of η in figures (7.9) and (7.10) . Both parameters show a flat behaviour in the η range between 1.8 and 2.4 with values $b \sim 16\%$ and $c \sim 0.7\%$ for electrons and converted photons and $b \sim 11\%$ and $c \sim 0.7\%$ for unconverted photons. The same constant term is achieved for all type of particles since this is a property of the calorimeter itself. The values obtained for the sampling term for electrons are also compatibles with those found in test beam measurements [26]. Note also a small peak in the sampling term around $\eta = 2.2$. Again, this is an effect of the structure of the ATLAS ID and will be explained in following sections. However, there is a large variation on both the sampling and constant term on the region $1.55 < \eta < 1.8$. The variation of the sampling term is attributed to the large amount and strong variation of upstream material. This also leads to a deviation of the constant term from the 0.7% observed in the rest of the calorimeter due to the correlation between the two parameters on the fitted function. For electrons, the sampling term varies from 16% up to 42% and the constant term from 0.6% up to 1.4%. The same behaviour is observed for converted photons. The sampling term varies from 16% up to 35% following the amount of upstream material. A smaller variation is observed for unconverted photons, for which the sampling term goes from 10% up to 20%. As a comparison, the EM Barrel at $\eta = 1.35$ has proved [39] to achieve a sampling term of $\sim 30\%$ for electrons, $\sim 22\%$ for unconverted photons

and $\sim 14\%$ for unconverted photons. This agrees with the results obtained in the EMEC in the range $1.7 < \eta < 1.75$ which is also the interval with the same amount of material in front of the calorimeter ($\sim 5X_0$). For $\eta < 1.7$ this value goes up to $7.5X_0$. This could make an EM shower to start and develop before reaching the calorimeter, making more difficult to totally correct for fluctuations and hence deteriorating the energy resolution. An extra reason would be a ϕ modulation in the upstream material due to the inner detector services. This includes extra material far away from the calorimeter producing early showers. As an example of both effects, the fraction of energy deposited in front of the calorimeter by 25 GeV electrons is represented for various η intervals in figure 7.11 as a function of eta and as a function of ϕ. For example, in the region $1.3 < \eta < 1.4$ the energy loss in the upstream material varies from 33 to 38 % within the η range whereas in both the other intervals the variation is of 15 %. Figure 7.11 b shows variations of 5 and 15 % for $1.6 < \eta < 1.7$ and $1.7 < \eta < 1.8$ respectively whereas the interval $1.3 < \eta < 1.4$ shows a flat value. Applying coefficients extracted specifically for each ϕ area would improve the energy scale and resolution in this area. However, as a first approximation for early data, ϕ symmetry was considered. The ATLAS Collaboration agreed to postpone this until a better description of the detector is determined from real data [1].

[1] For instance counting the number of conversions or looking at shower shape variables [38]

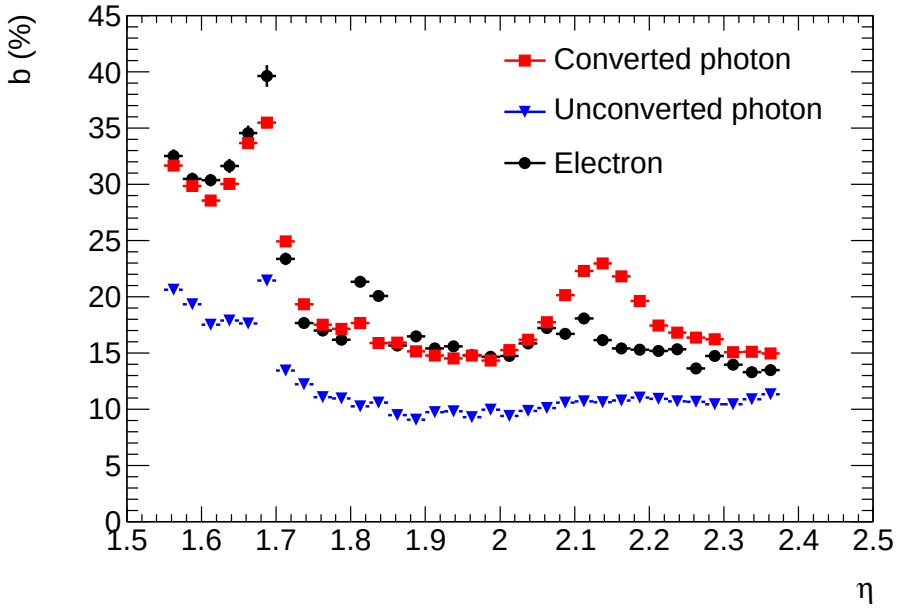

Figure 7.9: *Resolution sampling term for different type of particles versus η.*

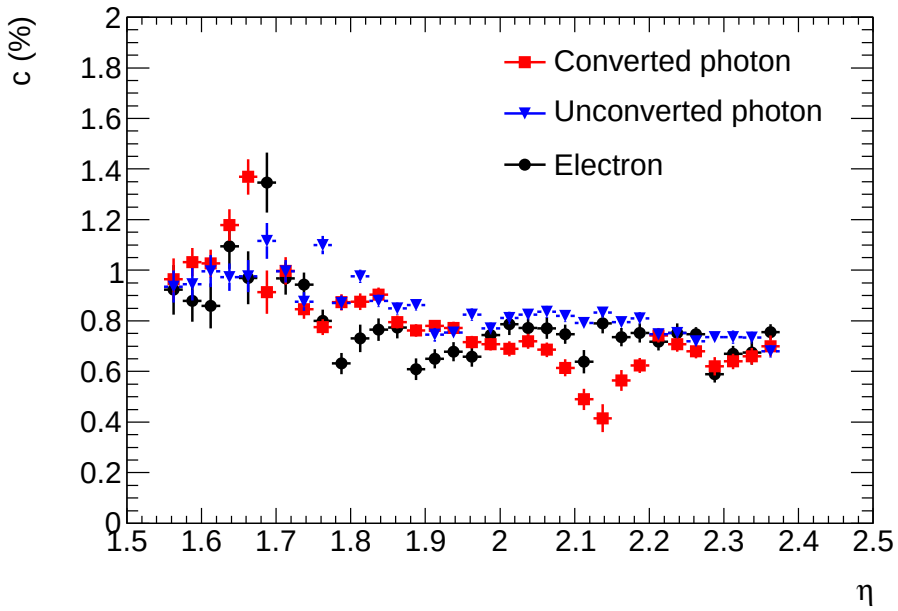

Figure 7.10: *Resolution constant term for different type of particles versus η.*

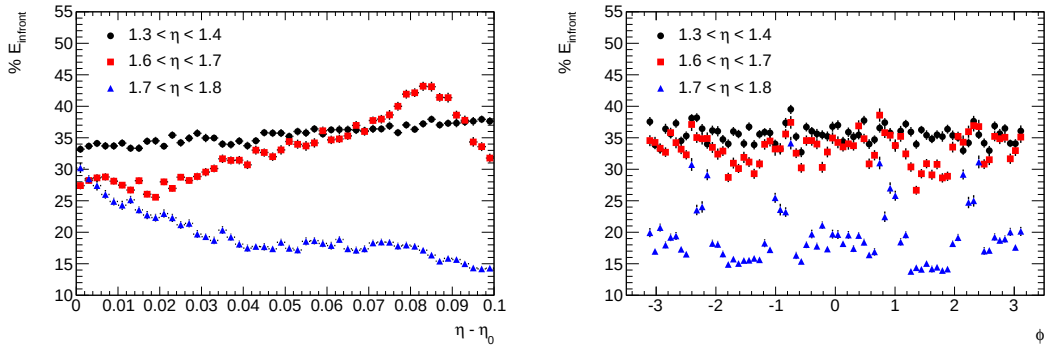

(a) fracion of energy versus eta η (b) fracion of energy versus eta η

Figure 7.11: Fraction of energy in front of the calorimeter in several η bins

7.1.3 Uniformity of the response

The uniformity of the response along η is represented in figures (7.12) (electrons), (7.13) (unconverted photons) and (7.14) (converted photons), for both the mean reconstructed energy and σ normalized to the true energy. The normalization is performed to check the energy resolution and scale simultaneously.

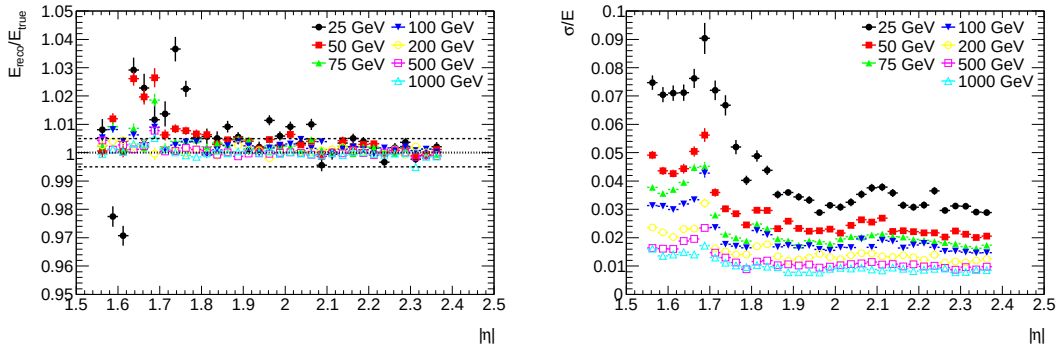

(a) E_{reco}/E_{true} versus eta η (b) fracion of energy versus eta η

Figure 7.12: Uniformity of σ/E and E_{reco}/E_{true} for electrons

Again the results can be commented in two different η intervals. For $\eta > 1.8$ the uniformity on energy scale is better than 0.5 %. Only a few calorimeter cells around $\eta \sim 2.0$ reach a value of $\sim 1\%$ for low energy electrons. Converted photons of energy higher that 50 GeV reach a uniformity within 0.5 % (1 % for 50 GeV). For very low energy , the uniformity goes up to 3 % at $\eta < 2.1$ and increases up to 4 % for higher values of η. The resolution is constant with η in this interval an compatible with $\sim (16\%/\sqrt{(E)} \oplus 0.7\%)$ for electrons and converted photons (as explained in previous sections). At $\eta \sim 2.1$ there is again an increasing behaviour in the resolutions since all the conversions happen very early. Resolution for unconverted photons is completely flat with η and compatible with $\sim (10\%/\sqrt{(E)} \oplus 0.7\%)$.

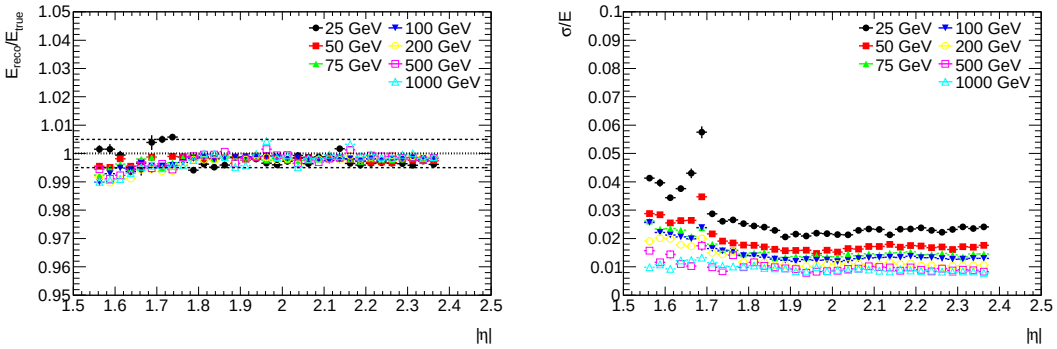

(a) E_{reco}/E_{true} versus eta η (b) fracion of energy versus eta η

Figure 7.13: Uniformity of σ/E and E_{reco}/E_{true} for unconverted photons

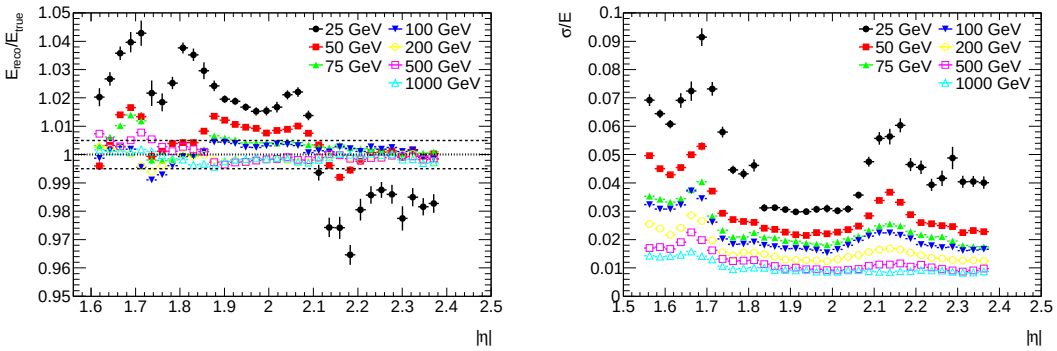

(a) E_{reco}/E_{true} versus eta η (b) fracion of energy versus eta η

Figure 7.14: Uniformity of σ/E and E_{reco}/E_{true} for converted photons

For $\eta < 1.8$ the resolution increases following the amount upstream material as explained in previous sections. The energy scale uniformity is within 0.5 % for unconverted photons except for the first cells. This is a consequence of the large variation of the LAr gap size with the depth. For electrons the uniformity is within 1 % except for very low energy points that can reach up to 4 %. Converted photons of energy lower than 50 GeV are within 1.5 % whereas the very low energy reaches up to 3% . As it will be discussed in following sections these results do not include the systematic error coming from the selected range for the gaussian fit. Due to both effects, the magnetic field and the upstream material, the energy distributions are extremely asymetric and varying the range of the fit from $(m - \sigma, m + 2.0\sigma)$ can modify the results.

7.2 Low energy tails

As stated in previous sections, the energy profiles after the CHM is applied have a main gaussian core but show a certain fraction of events at low energies clearly above the gaussian prediction. This is a consequence of the fact that the coefficients for recovering the energy loss in the upstream material and the lateral leakage are computed by considering Most Probable Values, hence fluctuations are not taken into account properly for these quantities. As an example, figure 7.15 shows the energy profile for 25 GeV particles hitting a cluster centered at $\eta = 2.0125$. In order to stress the presence of tails a gaussian fit (with limits $(\mu - \sigma, \mu + 2.0\sigma)$ as described in section 7.1) is superimposed and logarithmic scale is used. Unconverted photons are well described by the gaussian fit in most of the range, whereas electrons and converted photons are far away from the gaussian behaviour in the left part of the distributions.

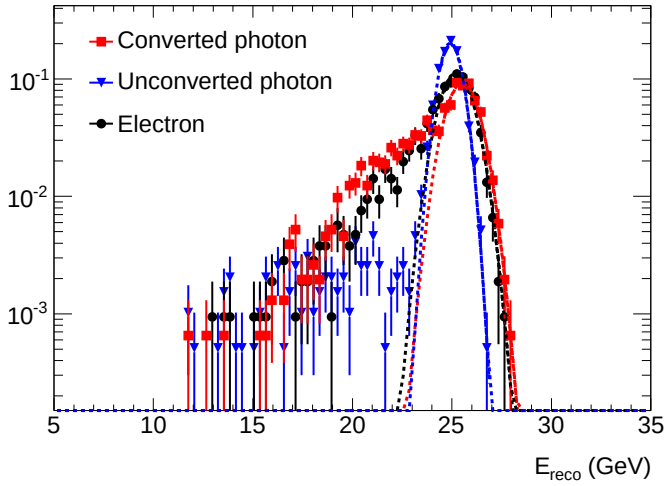

Figure 7.15: *Energy distribution for 25 GeV particles at* $\eta = 2.0125$

We define an event belonging to the low energy tail as such with energy $E < \mu - 1.5\sigma$. Figure 7.16 show the percentage of events in the low energy tail for the three type of particles and for two calorimeter cells. The dashed line correspond to the number of events expected if the distributions were perfectly gaussian. Electrons and converted photons can even reach 30 - 40 % of events in the tails. This effect decreases rapidly when the particle energy grows.

Figures 7.17 ,7.18 and 7.19 show the variation of the fraction of event with η for the various energies and for electrons, unconverted photons and converted photons respectively. For electrons, all energies bellow 200 GeV show a percentage of events higher than 20 % at very high η and reaching about 30 % in the central region. Unconverted photons, are much more gaussian-like. The case of converted photons is the worse with all energies below 200 GeV having a fraction of events in the tail higher than 30 % in the whole eta range. The effect seen at 25 GeV for $\eta > 2.1$ is a consequence of the fact that most of the photons have suffered an early conversion

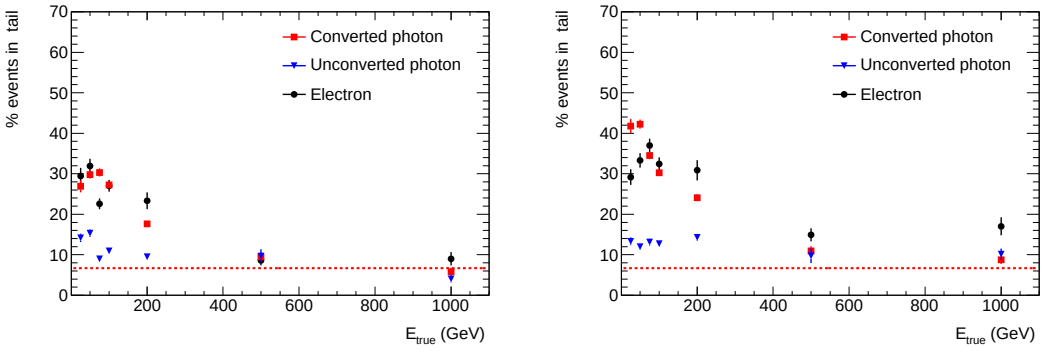

(a) $\eta = 1.7125$ (b) $\eta = 1.9125$

Figure 7.16: Fraction of event in the low energy tails as a function of energy

due to the structure of the ID. The hollow in this regions comes from the fact that the width of the fitted gaussian is larger (see Figure 7.14).

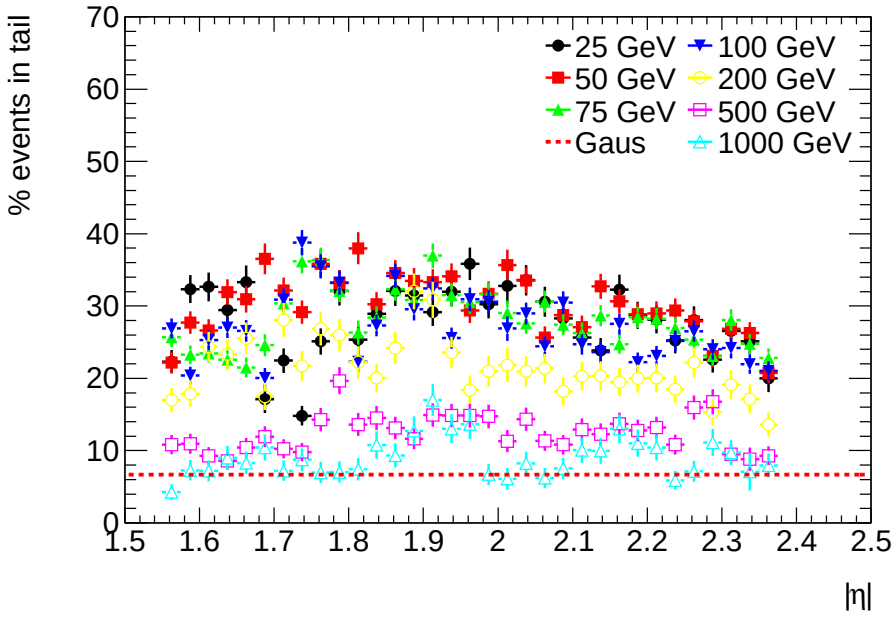

Figure 7.17: *Fraction of events in the low energy tails as vs η for electrons of various energies.*

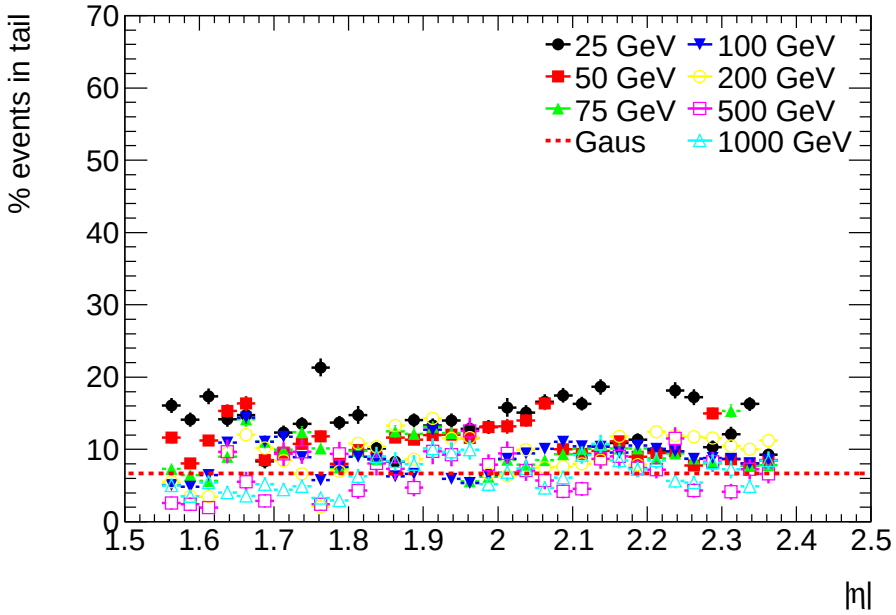

Figure 7.18: *Fraction of events in the low energy tails as vs η for unconverted photons of various energies.*

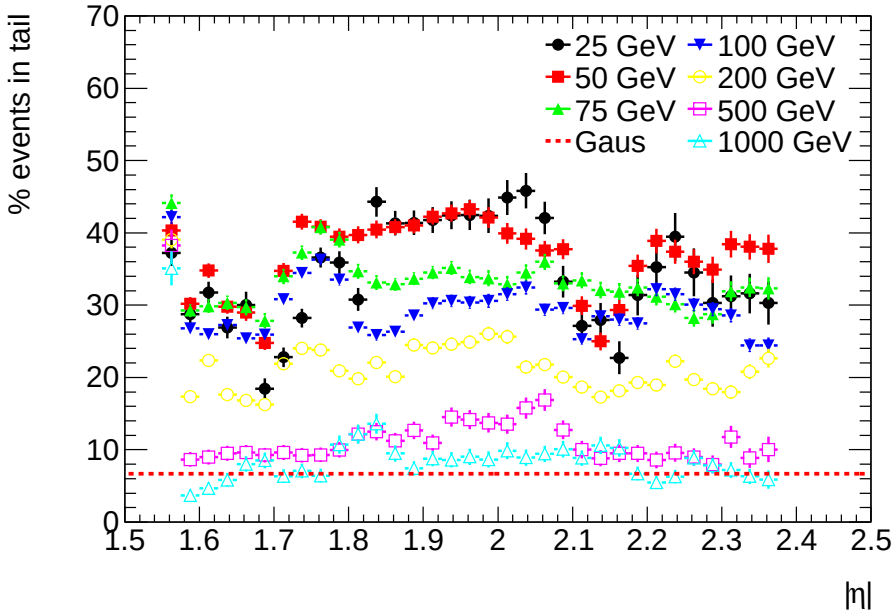

Figure 7.19: *Fraction of events in the low energy tails as vs η for converted photons of various energies.*

7.3 Contribution from the different corrections

First we would like to stress the necessity of applying a reconstruction method in order to improve the energy resolution, energy scale and linearity. With this goal we compare the energy scale and resolution , figures 7.20 and 7.21, when no corrections are applied at all (red squares), called raw energy in the graphic, with the case in which the Calibration Hits Method is used (black points). The left plots correspond to $\eta = 1.6375$ and the right ones to $\eta = 1.9125$. The x axis refers to the generated particle energy (E_{true}). It can be seen, for example, that at $\eta = 1.6375$ the raw energy is unaceptable, about 85% of the true 50 GeV for electrons and converted photons and 96 % for unconverted photons, while applying the Calibration Hits Method to this raw energy leads to an energy which is within 99.0 % of the true energy for all type of particles. Similarly for the energy resolution one sees the improvement applying the Method at $\eta = 1.6375$. In contrast, at $\eta = 1.9125$ there is only improvement for the energy scale, but no gain for the resolution. In the region $\eta > 1.8$ the distribution of upstream material is flat and small so the corrections for energy in the calorimeter are expected to be the most important ones, and in paticular the correction for lateral leakage. However this depends basically on the fluctuations of the transversal section of the electromagnetic shower that, as explained in chapter 4, is almost negligible. The corrections will have an effect on the low energy tail of the energy distributions due to the nature of the f_{out} correction.

As a second exercice, we discuss the contribution of the different corrections applied in the Calibration Hits Method to obtain the reconstructed energy. The modularity of the method allows to perform this kind of studies. Looking again at figures 7.20 and 7.21 and starting from the raw energy, the corrections are applied in an accumulative way following the order, f_{calo} (green triangles) thereafter f_{out} (blue triangles), next is f_{leak} (open yellow squares) and last $E_{infront}$ (black circles) which shows the performance of the full method.

The following exercice consists in fixing a certain generated energy, 100 GeV in this case, and study the contribution of the different corrections as a function of η. This is represented in figure 7.22 for the energy scale (left) and the energy resolution (right).

In the η interval $(1.55, 1.8)$ the largest contribution to the energy scale as well as the resolution is the correction by energy loss in front of the calorimeter, improving the former up to $\sim$ 25% and the latter up to $\sim$ 74% for electrons, $\sim$ 12% and $\sim$ 58% for unconverted photons and $\sim$ 20% and $\sim$ 55% for converted photons. At η values above 1.8 that correction becomes less important, having an impact only on the energy scale of a 1-2 percent for electrons and converted photons and almost a negligible effect for unconverted photons. The next significant correction is f_{out}, that is the correction for the cascade energy leaking transversally out of the defined cluster of calorimeter cells. It can be seen in figure 7.22 that the correction for the energy scale increases when η increases from $\sim$a 2% at low η to a $\sim$8% at high eta for unconverted photons and from 5-4% to 8-10% for electrons and converted photons. This reflects the two facts. Namelly: the cell size in cm decreases when η increases and the transverse momentum of the particles (for a given energy) decreases with

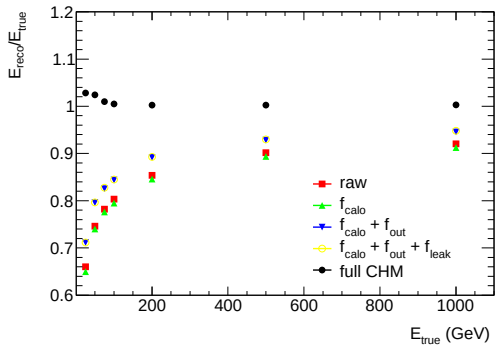

(a) $\eta = 1.6375$

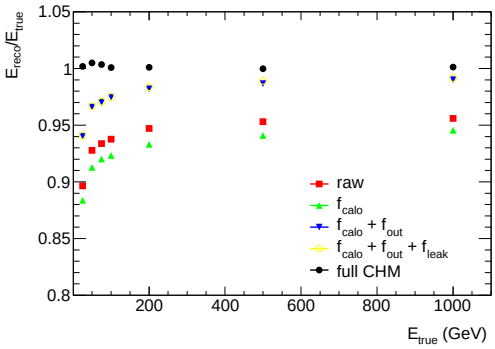

(b) $\eta = 1.9125$

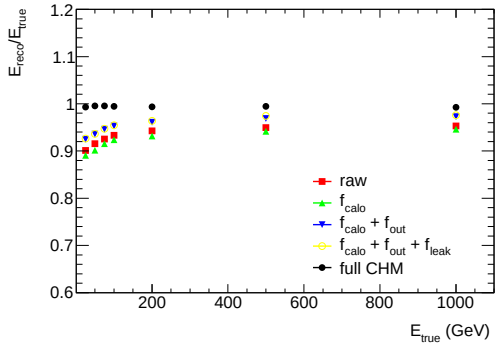

(c) $\eta = 1.6375$

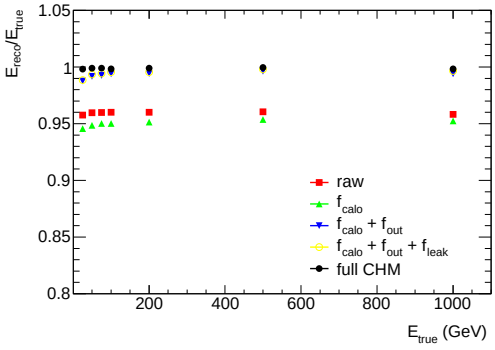

(d) $\eta = 1.9125$

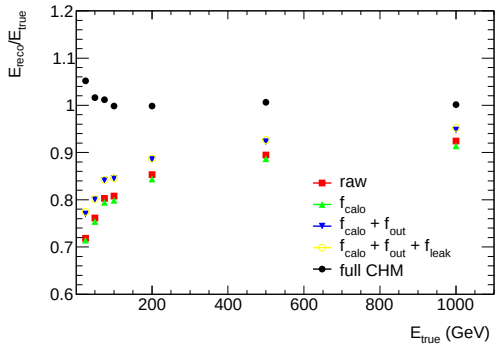

(e) $\eta = 1.6375$

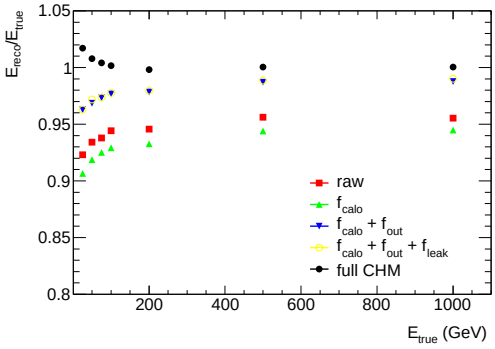

(f) $\eta = 1.9125$

Figure 7.20: *All different contributions to the Energy scale versus energy, The different plots correspond to electrons, unconverted and converted photons (from top to bottom)*

energy being theese particles more affected by the axial magnetic field. Hence more lateral leakage is expected a larger η values.

The factor f_{calo} has the effect of correcting a small overestimation applied at the reconstruction level before the Calibration Hits Method. Finally, as expected, the contribution of the energy behind the calorimeter (f_{leak}) is almost zero since the fraction of energy deposited in this part of the detector never exceeds 1% of the total energy for very high energies and 0.2% for low energy particles. The points are

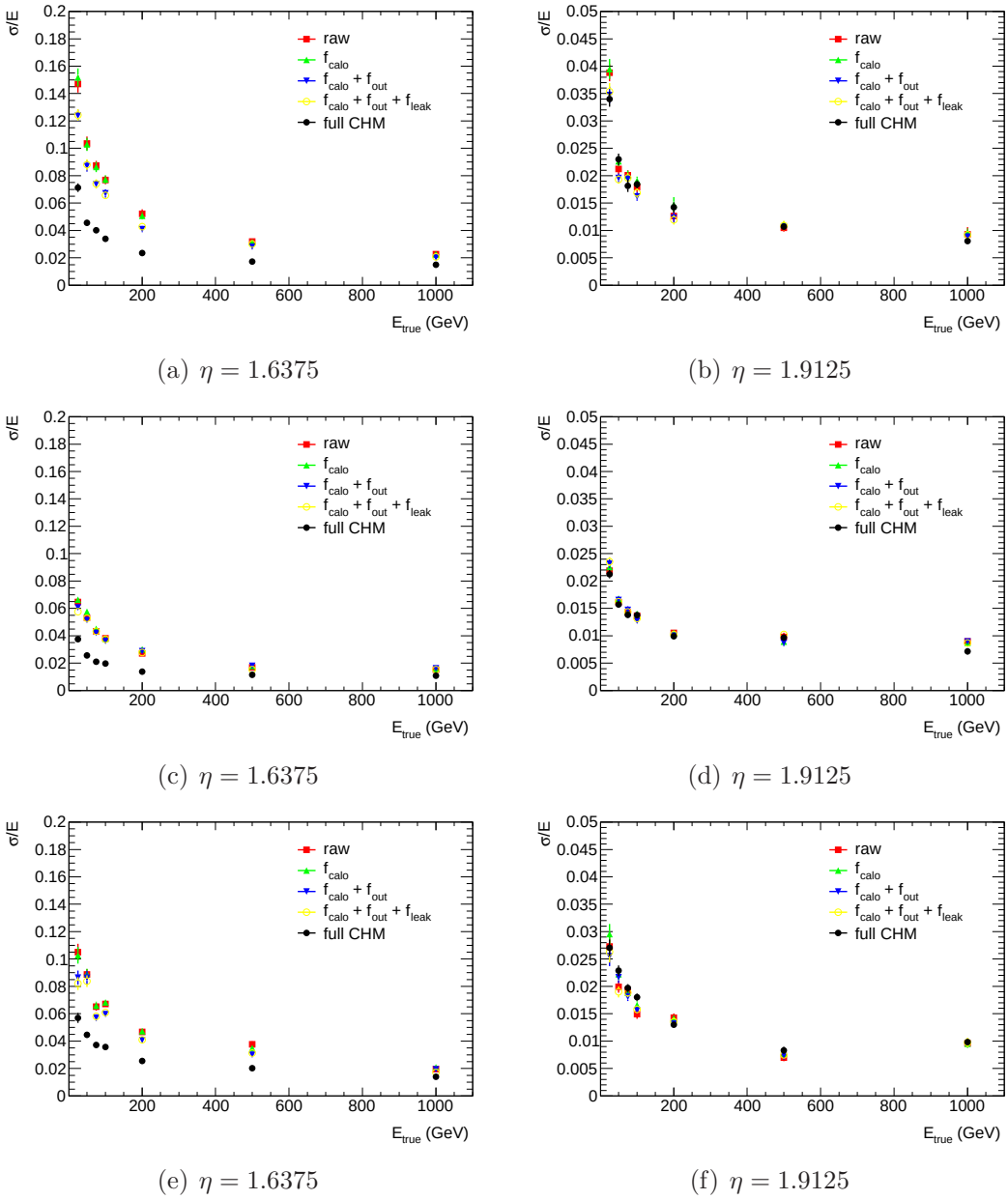

(a) $\eta = 1.6375$ (b) $\eta = 1.9125$

(c) $\eta = 1.6375$ (d) $\eta = 1.9125$

(e) $\eta = 1.6375$ (f) $\eta = 1.9125$

Figure 7.21: *Al different contributions to the resolution versus energy. The different plots correspond to electrons, unconverted and converted photons (from top to bottom)*

superimposed with the correction for f_{out} and can be hardly seen.

7.4 Effect of the radius of conversion

In this section we try to address a few dependences observed when studying the uniformity of the energy scale and energy resolution for converted photons. The energy scale varies following an almost step-wise function where the energy (for 25 GeV) is overestimated by 2 % for $\eta < 2.1$ and it is underestimated by 2 % for $\eta > 2.1$

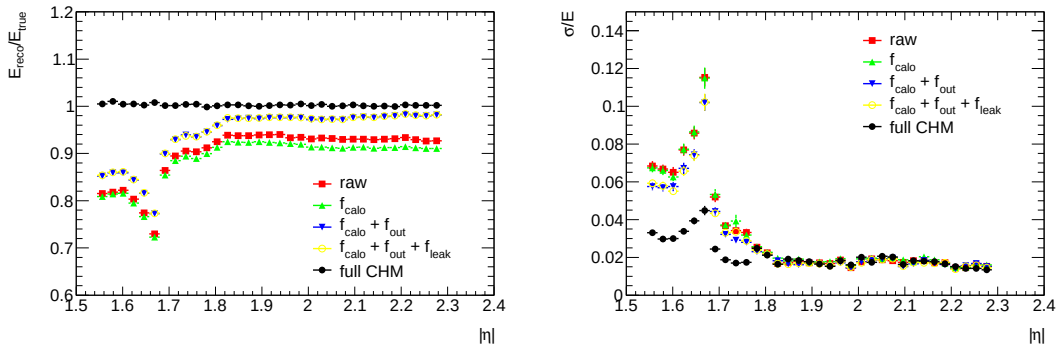

(a) E scale. Electrons

(b) Resolution. Electrons

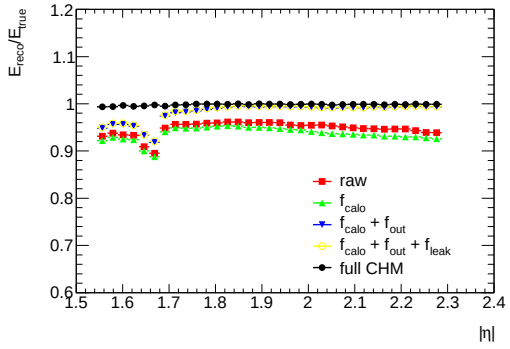

(c) E scale. Unconverted

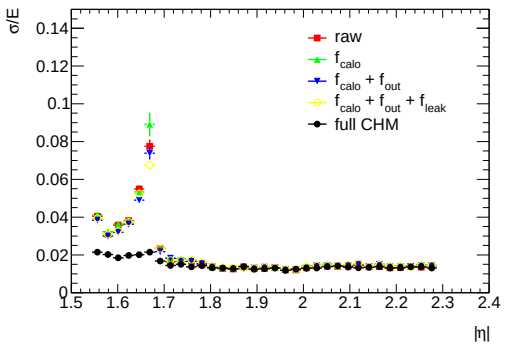

(d) Resolution. Uncenverted

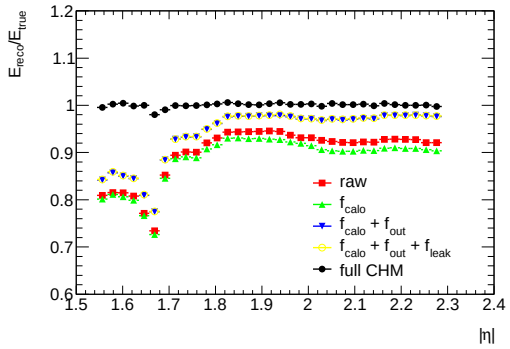

(e) E scale. Converted

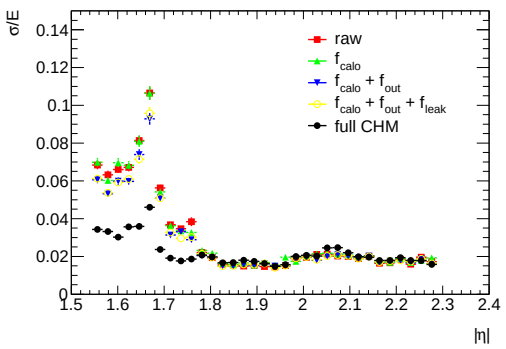

(f) Resolution. Converted

Figure 7.22: *Al different contributions to the resolution and energy scale for 100 GeV particles vs η*

(see Figure 7.14). This coincides with the coverage of the TRT detector. Figure 7.23 represents the distribution of conversion radius [2] for photons traversing the ATLAS detector in different directions. The main difference observed in the peak at around 65 cm which is not present in the two bottom figures, corresponding both of them to $\eta > 2.1$. The bin size $\Delta\eta = 0.1$ has been chosen in order to have enough statistics to divide the converted photon in sub-samples depending on R. Figure 7.24 represent

[2]The conversion radius is defined as the perpendicular (to the beam line) distance from the vertex where the pair e^+e^- is produced

the average R as a function of η with each bin corresponding to the size of a middle calorimeter cell ($\Delta\eta = 0.025$) showing the same step-wise behaviour at 2.1.

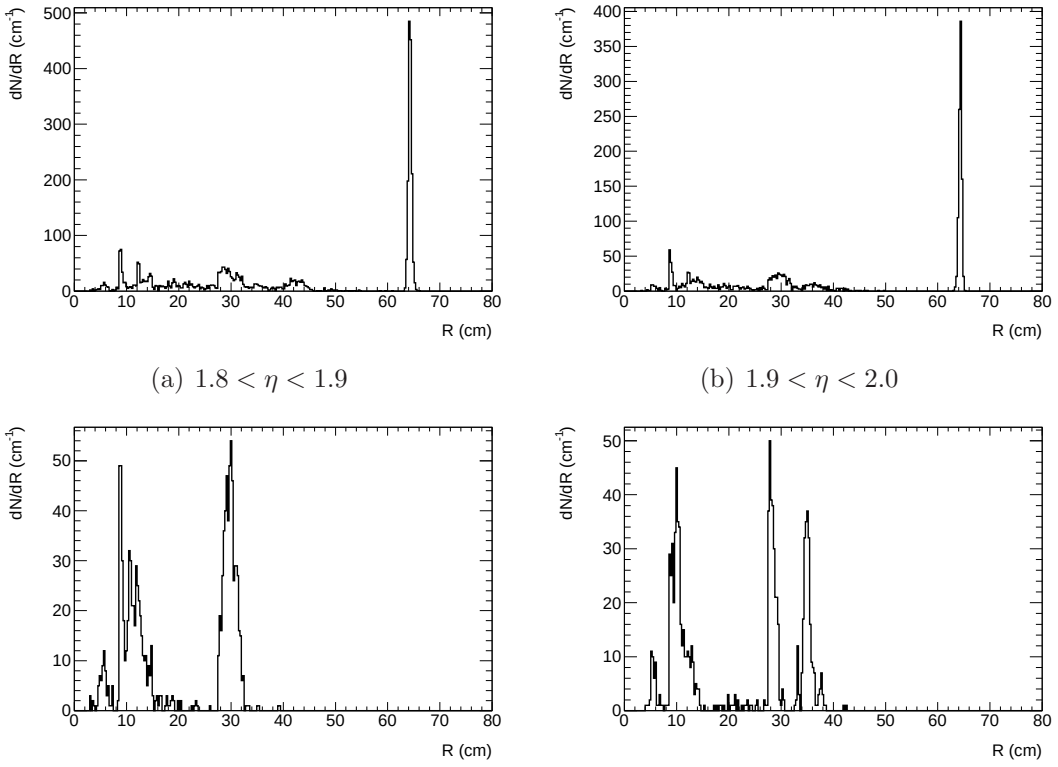

(a) $1.8 < \eta < 1.9$ (b) $1.9 < \eta < 2.0$

(c) $2.1 < \eta < 2.2$ (d) $2.2 < \eta < 2.3$

Figure 7.23: *Distributions of converted radii for different calorimeter η regions*

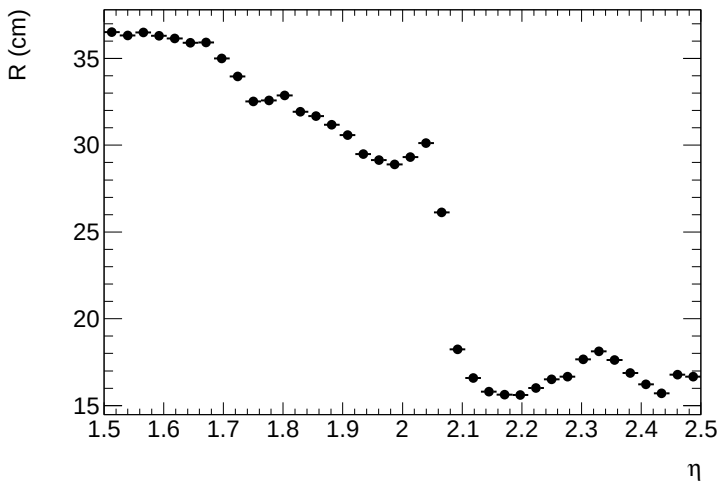

Figure 7.24: *Average conversion radius R vs η.*

Converted photons entering these bins are arranged in three categories, namely: photons converting at a radius lower that 20 cm, converting between 20 and 40 cm

and converting after 40 cm. The number of conversions in each category is given in Table 7.5. Since the correction coefficients are computed in a R average way, none of the sub-samples recover the expected 25 GeV but the mean somewhat averages to 25 GeV. For conversion at $\eta < 2.0$ the resolution is extracted from the peak corresponding to conversions at $R > 40\ cm$, even though the number of conversions at $R < 40\ cm$ is comparable (see Figure 7.25). Hence, σ is low but the energy is overestimated. For photons at $\eta > 2.1$ there are no conversions at $R > 40\ cm$ and the two remaining samples combine to form a wider distribution but more similar to a gaussian. Due to this effect the resolution increases. In this case, the underestimation of the energy showed in previous sections is partially a systematic effect of the asymmetric fit. In both the bottom plots it is clear that the Most probable value of the distribution is not well described by the gaussian fit. Preliminary studies on the application of R dependent coefficients in the reconstruction of converted photons have shown an improvement on the performance of the CHM for this type of particles. However, this approach was postpone until a better description of the detector can be implemented in the Monte Carlo simulations.

	$R < 20\ cm$	$20\ cm < R < 40\ cm$	$R > 40\ cm$
$1.8 < \eta < 1.9$	668	8890	1530
$1.9 < \eta < 2.0$	813	878	1563
$2.1 < \eta < 2.2$	672	631	0
$2.2 < \eta < 2.4$	672	631	0

Table 7.5: *Number of photon conversions with various radii and at different positions*

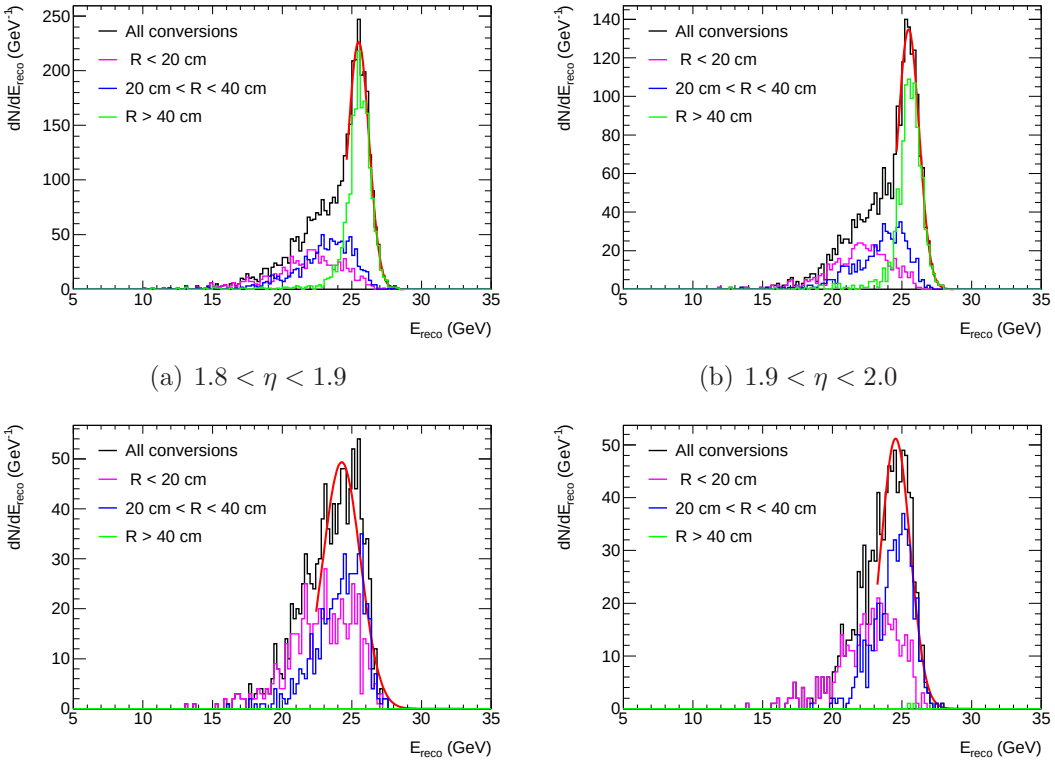

(a) $1.8 < \eta < 1.9$ (b) $1.9 < \eta < 2.0$

(c) $2.1 < \eta < 2.2$ (d) $2.2 < \eta < 2.3$

Figure 7.25: *Energy distributions for converted photons*

7.5 Performance of the CHM at $\eta > 2.375$.

In this section we summarize the performance of the calibration hits method in the last few cells of the EMEC, where a limited tracking information exists from the Inner Detector (no TRT and degraded performance of the Pixel+SCT). Since the "Loose" information of $IsEM$ (see Appendix A) was not available for photons, $IsEm$ selection is not applied in the region $\eta > 2.375$ for both electrons and photons. Figure 7.26 shows the energy distribution for all 7 generated energies and three type of particles. Since there is not a large amount of upstream material in the considered η range the energy distribution are similar for the three type of particles with the most significant difference being the low energy tails.

Comparing figures 7.2 and 7.26 (both correct the energy losses in front of the calorimeter by using the barycentre of the EM shower and both have similar amount of upstream material) we observe that the energy distributions in the later are wider, which reflects on a larger resolution (figure 7.27 a and table 7.6). This is a consequence of not applying quality cuts. The IsEm variable used in previous sections is based on cutting events from shower shapes variables computed using the first and second layer of the calorimeter as well as the fraction of energy leaked on the hadronic calorimeter (see Appendix A). Eliminating events from the edge of those distributions results in excluding events from the tails of the energy distributions as

well, and hence, a better resolution. A fairly higher fraction of events in the low energy tails, 7.27 b, is observed for the same reason.

σ/E	$b(\%)$	$c(\%)$
electrons	18.1913 ± 0.1866	1.1046 ± 0.0228
unconverted	12.0003 ± 0.1157	1.1267 ± 0.0136
converted	19.4290 ± 0.1591	0.8340 ± 0.0258

Table 7.6: *Sampling and constant term at* $\eta > 2.375$ *for the different type of particles*

Finally, the linearity at the per mil level is checked by using the procedure explained in section 7.1.1. The parameter of the fit e_1, related to the energy scale E_{reco}/E_{true}, its better than 0.5 % for all type of particles (see Figure 7.28). The parameter e_2 is again close to zero but not compatible with this value. The highest value is reached for converted photons as expected, since this particles are more affected by the lateral leakage correction which is the dominant in this region. All the values of Δm are within 0.5 %.

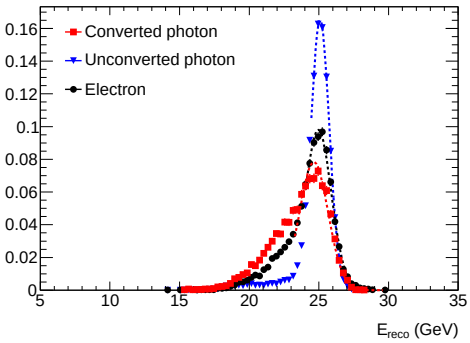

(a) $E = 25GeV$

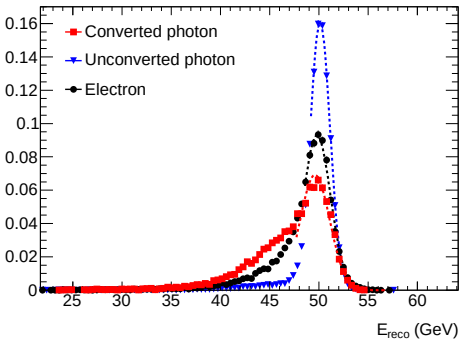

(b) $E = 50GeV$

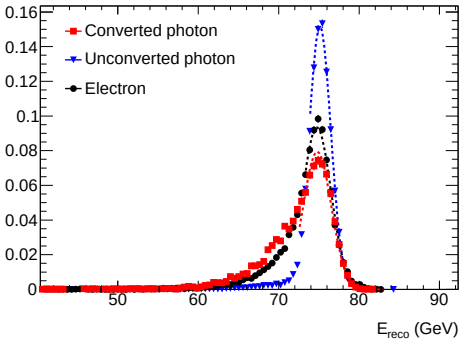

(c) $E = 75GeV$

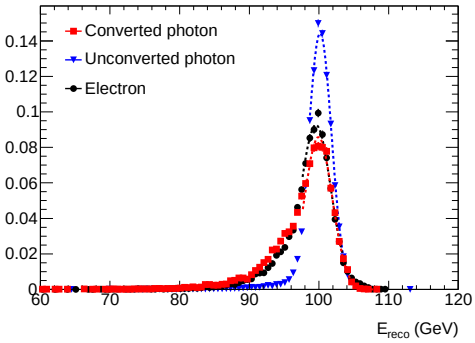

(d) $E = 100GeV$

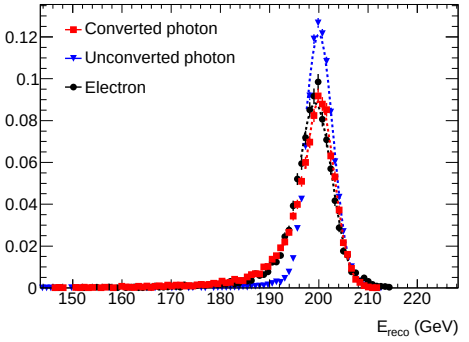

(e) $E = 200GeV$

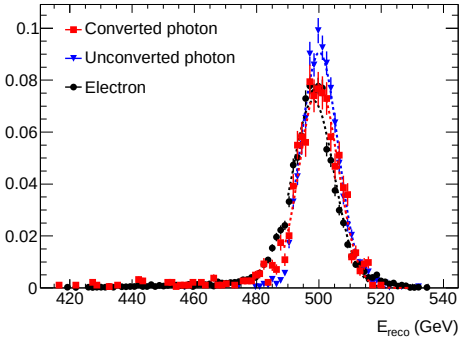

(f) $E = 500GeV$

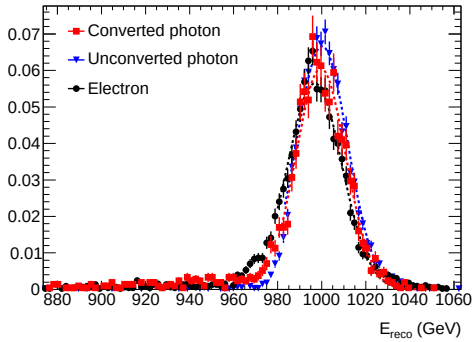

(g) $E = 1000GeV$

Figure 7.26: Reconstructed energies at $\eta > 2.375$. No IsEm cuts are applied

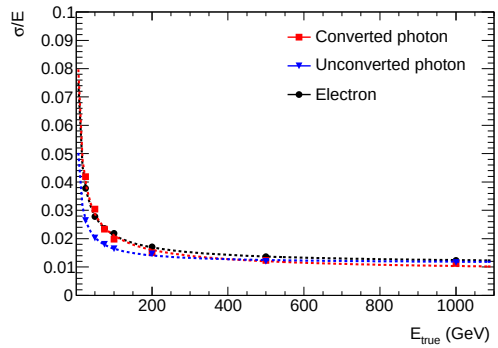

(a) Energy resolution

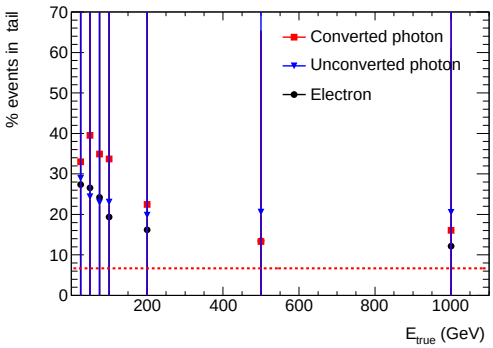

(b) Fraction of events in low energy tails

Figure 7.27: σ/E vs E_{true} and % events in tail vs E_{true} for all three type of particles

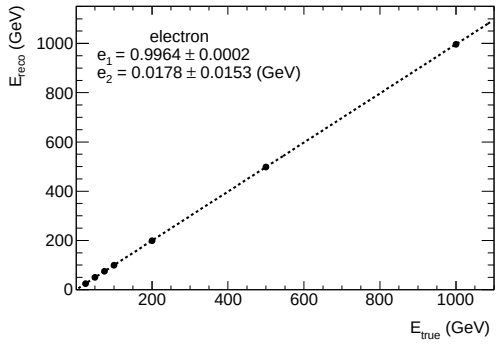

(a) $E = 25GeV$

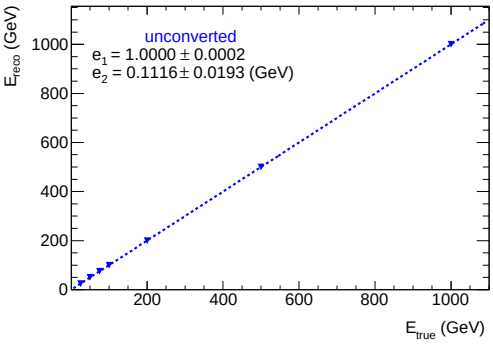

(b) $E = 50GeV$

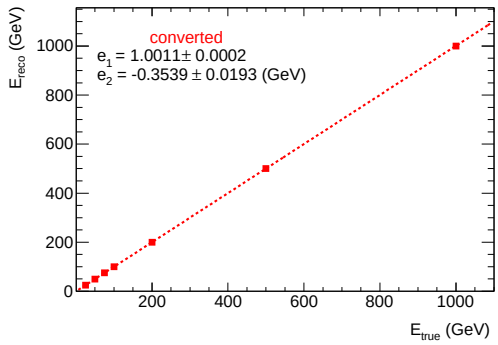

(c) $E = 75GeV$

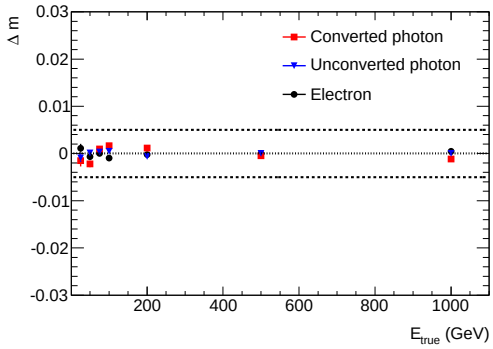

(d) $E = 100GeV$

Figure 7.28: E_{reco} vs E_{true} and Δm vs E_{true} for all three type of particles

7.6 Effect of the fit Limits

The calibration hits method cannot perfectly recover the energy lost due to the combined effect of the the upstream material and the deflection of low energy electrons by the axial magnetic field, present in the tracking detectors. These three effects distort the left side of the distributions producing tails that, as shown in the previous section, for low energies electrons and converted photons could contain up to 40 % of the events. Results in terms of energy scale and resolution are based on a gaussian fit of the distributions using a lower limit. In this section the systematic error introduced by the election of the fit lower limit is studied. For completeness the analysis is also performed for the upper limit.

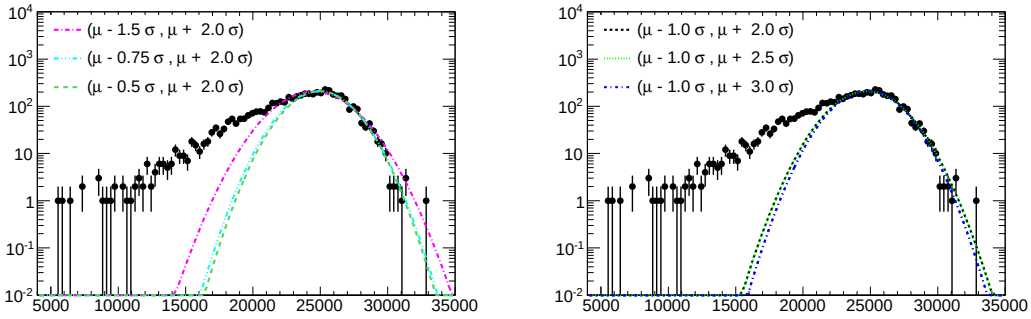

(a) Upper limit fixed to 2σ

(b) Lower limit fixed to 1σ

Figure 7.29: Energy distribution for 25 GeV electrons hitting at $\eta = 1.6375$ superimposed with various gaussian fits

As an example, figure (7.29) represents an energy distribution for 25 GeV electrons hitting a cluster centered at $\eta = 1.6375$ superimposed with six gaussian fits performed between the limits: $(\mu-0.5\sigma, \mu+2.0\sigma)$, $(\mu-0.75\sigma, \mu+2.0\sigma)$, $(\mu-\sigma, \mu+2.0\sigma)$, $(\mu-1.5\sigma, \mu+2.0\sigma)$, $(\mu-\sigma, \mu+2.5\sigma)$ and $(\mu-\sigma, \mu+3.0\sigma)$.

Due to the low energy tail, the mean value of the fitted gaussian moves to lower values as we decrease the left limit of the interval for the fit. In order to prove which fit describes better the energy distribution figure (7.30) shows $\chi^2/N.d.o.f$ versus the energy. Here we see two effects. The value of $\chi^2/N.d.o.f$ decreases as the left part of the interval gets closer to the most probable value of the distribution. The quality of the fit is better at higher energies, since high energy particles are less affected by the distorting effects showing more gaussian-like distributions.

Figures (7.31) and (7.32) show the effect of the different fit intervals on the energy scale and the energy resolution. The variation of the upper limit does not change the results as expected. The modification of the lower limit affects the lowest energies: moving the left limit for the fit from $\mu-1.5\sigma$ to $\mu-0.5\sigma$ leads to a variation in the energy scale up to 2 % at 25 GeV. A similar effect is seen on the energy resolution. High energy points are barely affected whereas for very low energy the resolution varies from ~ 0.095 $(\mu-1.5\sigma)$ up to ~ 0.078 $(\mu-0.5\sigma)$.

Finally, table 7.7 shows sampling and constant term obtained for the different

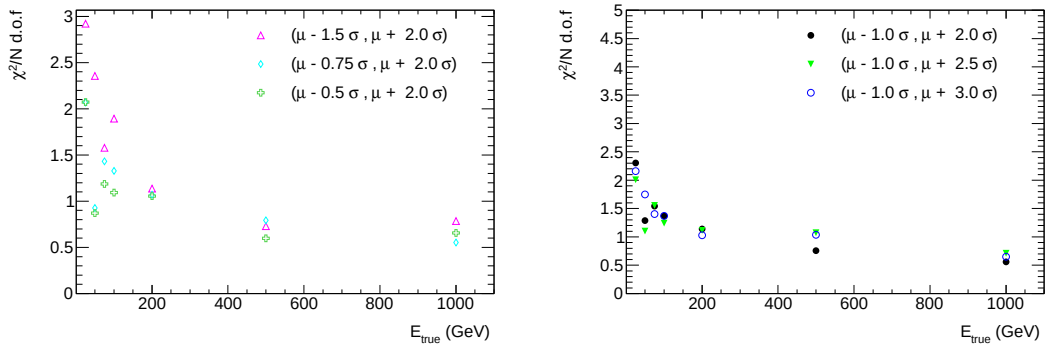

(a) Upper limit fixed to 2σ (b) Lower limit fixed to 1σ

Figure 7.30: *$\chi^2/N.d.o.f$ versus energy for electrons hitting at $\eta = 1.6375$ for the various fits.*

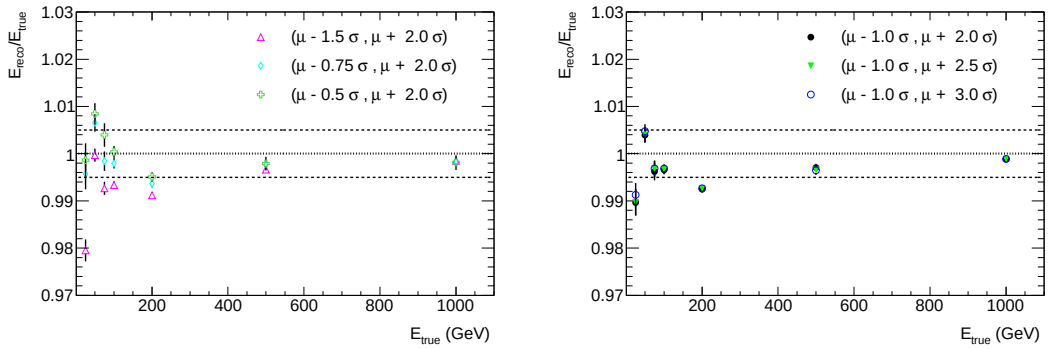

(a) Upper limit fixed to 2σ (b) Lower limit fixed to 1σ

Figure 7.31: *Energy scale versus energy for electrons hitting at $\eta = 1.6375$ for the various fits.*

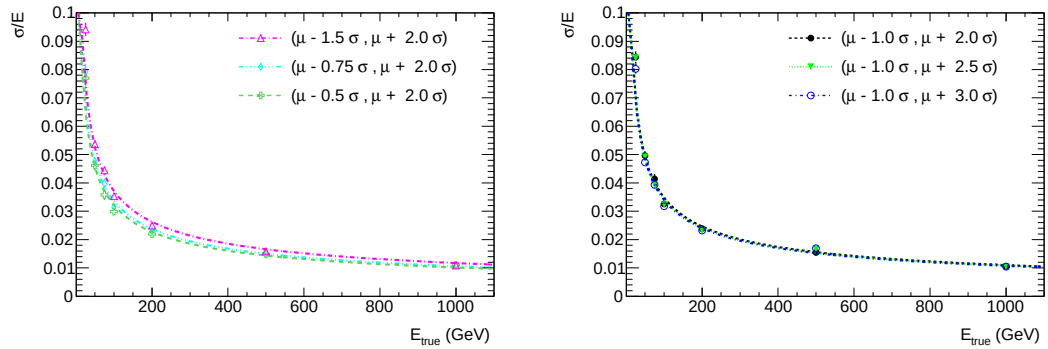

(a) Upper limit fixed to 2σ (b) Lower limit fixed to 1σ

Figure 7.32: *Energy resolution versus energy for electrons hitting at $\eta = 1.6375$ for the various fits.*

fits presented in figure (7.32). Once again, the closer the low limit to the mean value of the gaussian, the better the resolution is described by $\frac{b}{\sqrt{E}} \oplus c$. The decision of studying the performance of the calorimeter by fitting the energy distributions to the range $(\mu - \sigma, \mu + 2\sigma)$ was a compromise between including most part of the distribution and keeping a reasonable gaussian fit quality.

Fitted Interval	b (%)	c (%)	$\chi^2/N.d.o.f$
$(\mu - 0.5\sigma, \mu + 2.0\sigma)$	32.034 ± 0.717	0.073 ± 1.389	4.755
$(\mu - 0.75\sigma, \mu + 2.0\sigma)$	33.606 ± 0.489	0.000 ± 0.393	5.329
$(\mu - \sigma, \mu + 2.0\sigma)$	34.967 ± 0.440	0.000 ± 0.190	10.287
$(\mu - 1.5\sigma, \mu + 2.0\sigma)$	37.224 ± 0.372	0.000 ± 0.119	20.983
$(\mu - \sigma, \mu + 2.5\sigma)$	34.415 ± 0.342	0.000 ± 0.185	15.013
$(\mu - \sigma, \mu + 3.0\sigma)$	34.100 ± 0.300	0.000 ± 0.197	17.181

Table 7.7: *Sampling term, constant term and* $\chi^2/N.d.o.f$ *at* $\eta = 1.6375$ *for various gaussian fits.*

Chapter 8

Calibration Hits Method on physics events

In the previous chapter the Calibratin Hits Method (CHM) has been applied to single electron samples in order to estimate its performance along the EMEC. In this chapter the functioning of the CHM is evaluated using physics events, namely $pp \rightarrow Z \rightarrow ee$. The importance of the CHM becomes clear in figure 8.1, where the invariant mass of the di-electron system in $Z \rightarrow ee$ event is represented for electrons calibrated with CHM (black line) and with no reconstruction method applied (red line). The former case shows a narrower distributions with a peak and width close to the Z mass and width nominal values, whereas the latter is out by more than 6%.

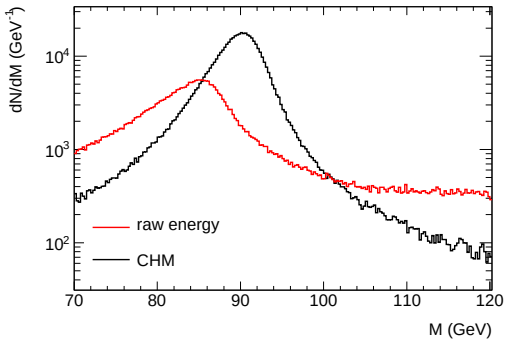

(a) Pythia

Figure 8.1: Di-electron mass distribution for PYTHIA events: before (red) and after (black) applying the CHM.

8.1 Data samples and event selection

The data set used in this section has been centrally produced by the ATLAS collaboration using PYTHIA 6.4 [47]. This generator includes leading order matrix elements, and simulates initial and final state QCD radiation as well as the underline event and

hadronisation. Final state QED radiation is calculated using PHOTOS [49]. The sample consist of 2.5 Million $Z/\gamma^* \rightarrow e^+e^-$, produced on proton-proton collisions at center of mass energy $\sqrt{s} = 10\ TeV$ [1]. The interactions of the particles predicted by Pythia with the atlas detector are simulated via GEANT 4 (both PYTHIA and GEANT are incorporated in ATHENA, the ATLAS software). In order to avoid long CPU time a generator level filter is applied. At least one lepton with $|\eta| < 2.8$, which eliminates events with particles very unlikely to be reconstructed due to the ATLAS acceptance. A lower limit on the invariant mass of the di-electron system ($M_{ee} > 60\ GeV$) is imposed to remove the low mass Drell-Yan component. A second sample with the same characteristics but generated with AlpGen [48] was also included. AlpGen ia a generator dedicated to multiparton hard processes in hadron collisions which also performs leading order matrix calculations. The number of events was one order of magnitude lower in this case. Both QED and QCD radiative corrections are included in this sample as well.

In order to select the interesting events for this analysis the following cuts were applied. Only events with two reconstructed electrons with opposite charges and transverse momentum higher that 20 GeV were considered. Both electrons are required to have $|\eta| < 2.5$ excluding the region not calibrated with the CHM ($1.425 < |\eta| < 1.55$). The electrons were also required to satisfy a Tight IsEm cut (see Appendix A) and the invariant mass of the di-electron system had to be higher than 60 GeV to be consistent with the generated samples. Finally, all events where the two selected electrons could not be matched to a truth electron were removed from the analysis.

8.2 Z Line Shape Modeling

The cross section of the process $q\bar{q} \rightarrow Z/\gamma \rightarrow e^+e^-$ is theoretically well known, as seen in section 2.4. However, in order to describe the Z line shape in proton-proton collisions, a good description of the parton density functions (PDFs) is required.

The pure Z contribution to the line shape (σ_Z in equation 2.8), is given by a relativistic Breit-Wigner:

$$BW(M) = \frac{\Gamma_Z^2 M^2}{(M^2 - M_Z^2)^2 + M^4\Gamma_Z^2/M_Z^2} \tag{8.1}$$

where M_Z is the mass and Γ_Z the total width of the Z boson. This two parameters where very precisely determined at LEP [43] , namely $M_Z = 91.1874 \pm 0.0021\ GeV$ and $\Gamma_Z = 2.4952 \pm 0.0023\ GeV$.

In hadronic collisions, the mass spectrum of the Z boson [45] differs from the Breit-Wigner function of the partonic process. Due to the PDFs, the probability of a $q\bar{q}$ interaction to form an object of mass M decreases with the mass. This effect is taken into account if we multiply the Breit-Wigner by the function:

[1] This was the expected energy for the first year run of the LHC, recently changed to $\sqrt{s} = 7\ TeV$

$$\mathcal{L}(M) = \frac{1}{M^{\beta}} \tag{8.2}$$

where β is known as the parton luminosity parameter.

Figure 8.2 shows the mass distribution for the di-electron system for events generated with Pythia (left) and AlpGen (right). The following function has been used to fit the distribution:

$$k\ BW(M)\ \mathcal{L}(M) \tag{8.3}$$

which has 4 free parameters, namely the global normalization k, the Z mass and width M_Z, Γ_Z and the parton luminosity β (see green curve on Figure 8.2). The values of the fitted parameters are shown in table 8.1. The small deviations from the nominal values of M_Z and Γ_Z, at the level of one in ten thousand, are attributed to the fact that we are not considering the Z/γ^* interference terms in the fit. Since this uncertainty is negligible compared with the one coming from the detector resolution at the reconstruction level (see below), and in order to keep formulas simpler, the interference terms are not taken into account.

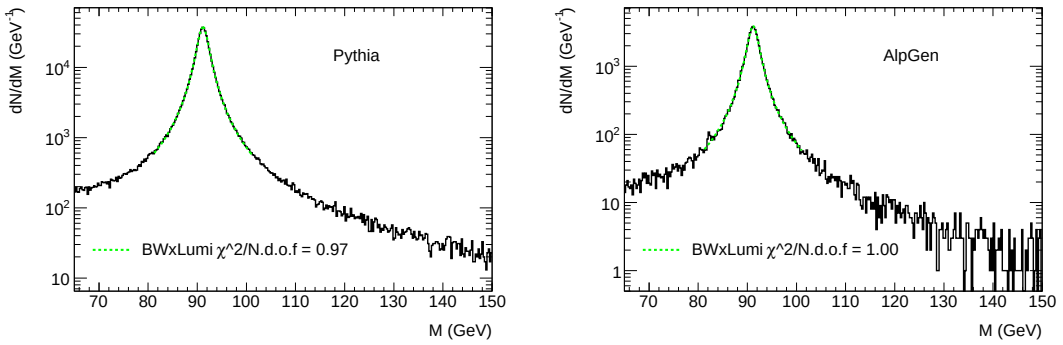

(a) Pythia (b) AlpGen

Figure 8.2: Di-electron mass distribution fitted to a Breit-Wigner luminosity term (green). The fit range is $[80, 100]$.

	M_Z (GeV)	Γ_Z (GeV)	β
Pythia	91.168 ± 0.003	2.506 ± 0.005	0.182 ± 0.057
AlpGen	91.191 ± 0.008	2.474 ± 0.0160	0.192 ± 0.160

Table 8.1: *Parameters obtained from fitting the mass distribution at the generation level to the function 8.3*

The parameter β is represented in figure 8.3 as a function of the Z boson pseudorapidity. Since it depends on the Z boson kinematics, this parameter should be recomputed in case of different kinematic cuts.

Finally, in order to take into account the resolution of the detector, the Z line shape description should be convoluted with a function R(M) modeling this effect:

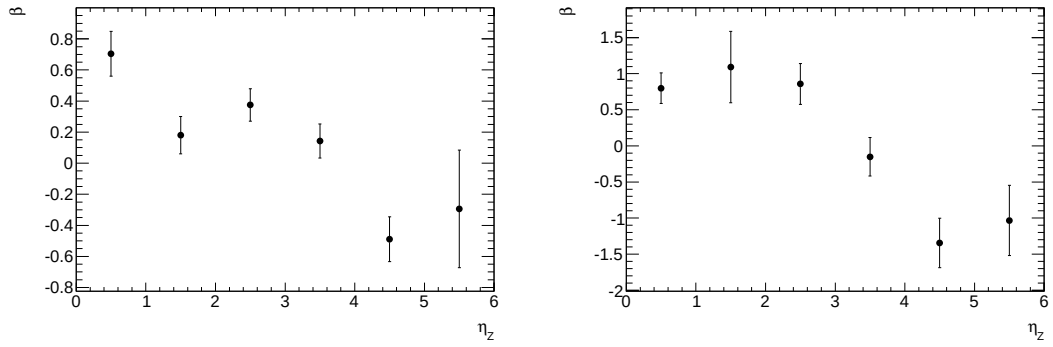

(a) Phythia (b) AlpGen

Figure 8.3: Dependence of β with the Z boson presudorapidity

$$L(M) = \int_0^\infty \mathcal{L}(x) \cdot BW(x) \cdot R(x - M)dx \tag{8.4}$$

As a first approximation, the resolution of the di-electron invariant mass is described by a gaussian:

$$R(M, \sigma) = \frac{e^{-M^2/2\sigma}}{\sqrt{2\pi}\sigma}$$

with σ correlated with the electron energy resolution. However, as discussed in section 7.2, the energy distributions have not only a gaussian core but also show a low energy tail, which means the CHM cannot recover all losses on an event by event basis. In addition, QED radiation of low energy photons by the electrons in the final state also contribute to the appearance of such tails. This feature is taken into account by using a "Cristal Ball" function [44], which consists of a gaussian core portion and a power-law low-end tail below a certain threshold, as a model for the detector resolution:

$$R(M) = \frac{1}{\sqrt{2\pi}\sigma} \begin{cases} exp\left(-\frac{M}{2\sigma}\right)^2 & \frac{M}{\sigma} > -|a| \\ \left(\left(\frac{n}{|a|}\right)^n \cdot e^{-\frac{1}{2}\cdot a^2}\right) / \left(\frac{n}{|a|} - |a| - \frac{M}{\sigma}\right)^n & \frac{M}{\sigma} \leq -|a| \end{cases} \tag{8.5}$$

being a and n correlated to the tails in the energy distributions.

The integral of Equation 8.4 is solved numerically, transforming to a discrete summation in N steps, i.e;

$$L(M) = \sum_{i=0}^{N} \cdot \mathcal{L}(x_i) \cdot BW(x_i) \cdot R(x - M) \cdot \Delta x \tag{8.6}$$

The convolution parameter x_i is limited to take values $-p \cdot \sigma < x_i < p \cdot \sigma$ with p an integer number and σ the standard deviation of the gaussian core in 8.5. Hence,

$\Delta x = 2 \cdot p \cdot \sigma / N$. The values of p and N where chosen to be 20 and 400 respectively since small variations around these values do not affect the result of the fit.

Figure 8.4 shows the reconstructed mass of the di-electron for events that have been passed through the ATLAS detector simulation. As a comparison the same distribution at the generator level is also plotted. A clear increase in the broadness of the distribution is observed when considering the reconstructed mass at the detector level. This effects are taken into account by function R in Equation 8.3. This function needs to be a crystal ball instead of a gaussian, as can be seen in Figure 8.4, otherwise the distribution cannot described properly causing a bias in the Z mass determination.

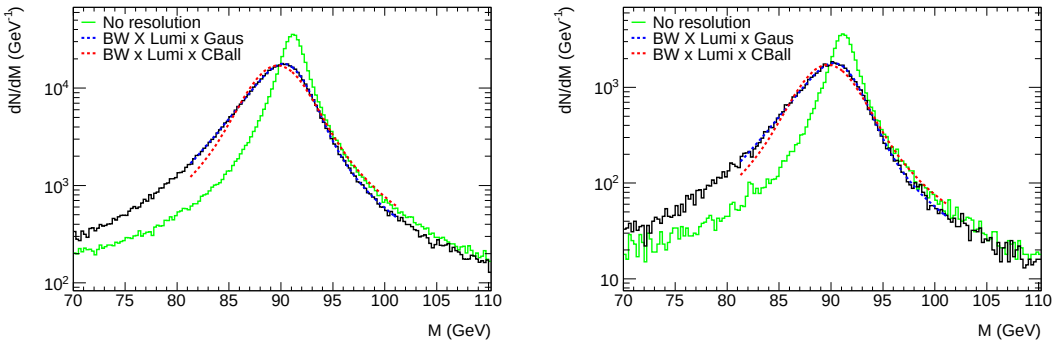

(a) Pythia (b) AlpGen

Figure 8.4: Di-electron mass distribution for reconstructed event The distribution is fitted to equation 8.3 being $R(x)$ a standar gaussian (red) and a cristal Ball function (blue).

8.3 Calorimeter performance regions

As discussed in chapter 7, the performance of the calorimeter has a strong dependence on η mostly due to the upstream material. In the EMEC, at $\eta < 1.8$ the sampling term of the resolution reaches $\sim 40\%$ and the energy scale at very low energy can go up to 3%. In the same way, the resolution of the EMB degrades for $\eta > 0.7$ going up to a sampling term of $\sim 30\%$ [39, 46]. These results were obtained with single electron samples. However, in collision events there are other factors such us underline event or initial and final state radiation, that may affect the behaviour of isolated electrons, in particular those coming from Z boson decays. As an exercise, we try to reproduce the energy resolution and energy scale map of the calorimeter by using the $Z \rightarrow ee$ samples described above. Of course, the energy spectrum of the electron coming from the Z decay is continuous, hence a comparison should be made by averaging the results obtained in section 7. This average has to take into account the energy distribution of the two Z electrons coming from the Z decay. Figure 8.5 shows the energy distribution of the two electron (top) and the average of this energy as a function of η (bottom) for the samples generated with Pythia and

AlpGen (left and right respectively). Electron 1 denotes the electron with highest transverse momentum, hence it shows larger energies than Electron 2 throughout the whole pseudorapidity range.

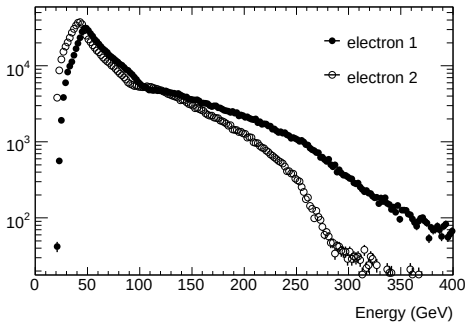

(a) E_1 and E_2 distribution

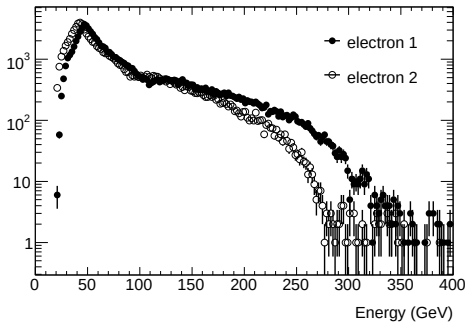

(b) E_1 and E_2 distribution

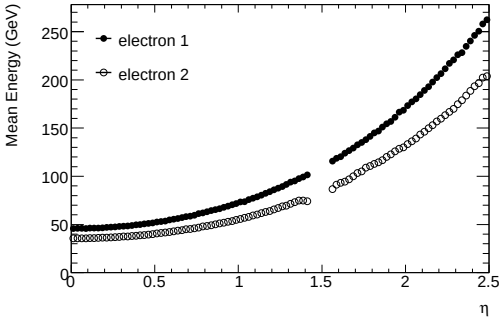

(c) Mean energy versus η

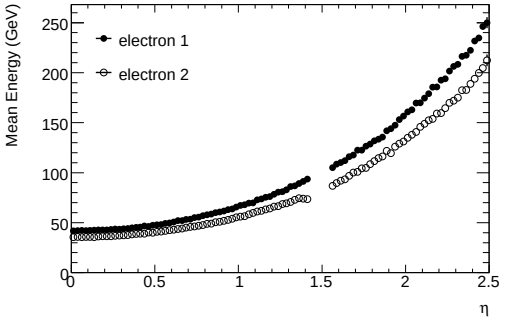

(d) Mean energy versus η

Figure 8.5: Energy distribution and mean energy vs η for the two electrons coming from the Z decay

In order to produce a calorimeter resolution and energy scale map, a reconstructed electron has to be matched with the electron at generator level inmediately decaying from the Z boson. The matching is implemented through the following quantity:

$$\Delta R = \sqrt{(\Delta\eta)^2 + (\Delta\phi)^2}$$

where $\Delta\eta = \eta_{reco} - \eta_{true}$ and $\Delta\phi = \phi_{reco} - \phi_{true}$. If $\Delta R < 0.2$ both reconstructed and generated electrons are linked to each other. With this procedure, the efficiency of matching both electrons (after cuts) is $\sim 100\%$.

Figure 8.6 and 8.7 show distributions of the quantities E_{reco}/E_{true} and $(E_{reco} - E_{true})/\sqrt{E_{true}}$ respectively, the former giving and idea of the energy scale and the latter of the resolution [2]. Since the resolution and energy scale depend on the true energy of the particle, electron 1 and electron 2 are considered separately due to their different average energy. Both distributions are superimposed with an iterative gaussian fit as explained in section 7.1. As expected, longer low energy tails are observed for electron 2, which has smaller energy.

[2]In a perfectly homogeneous calorimeter the standard deviation of this distribution agrees with the stochastic term of the resolution

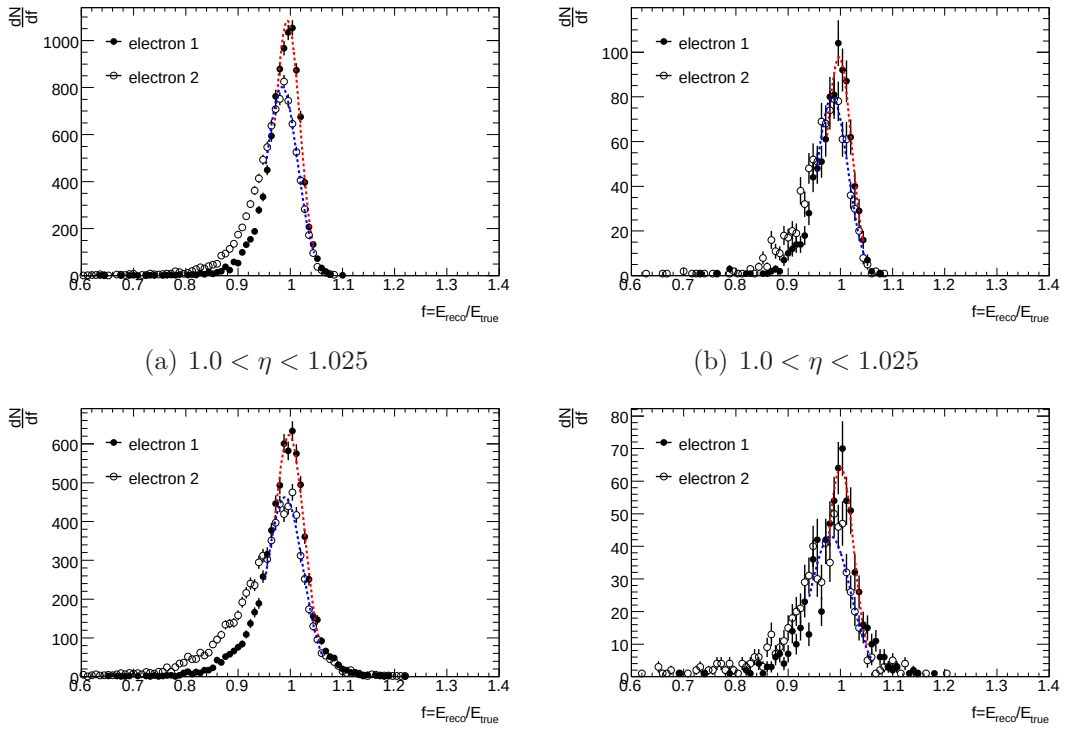

(a) $1.0 < \eta < 1.025$ (b) $1.0 < \eta < 1.025$

(c) $1.7 < \eta < 1.725$ (d) $1.7 < \eta < 1.725$

Figure 8.6: E_{reco}/E_{true} distribution in two different calorimeter cells for samples generated with Pythia (left) and Alpgen (right)

The mean value of E_{reco}/E_{true} and its σ from the gaussian fit are represented in figures 8.8 a and b. Dashed lines indicate the $\pm 0.5\%$ region. Electron 2 has a lower reconstructed energy which can reach up to 3 % deviation in the region where the upstream material is substantially bigger. The QED final state radiation in combination with the material in front of the calorimeter makes the reconstructed energy to decrease. Low energy radiated photons are absorbed in the upstream material wich prevents them to reach the calorimeter cluster. In addition, low energy electrons may be bent by the magnetic field in such a way they also miss the calorimeter cluster. A toy model to study the effect of QED radiation has been developed in Section 8.5.

A similar effect is shown in the guassian σ, from a base line at about 0.015 the standard deviation increasing following the profile of upstream material. Note again that σ for electron 2 is slightly larger due to the lower average energy. Figures 8.8 e and f give an approximation to the sampling term. In this case the energy average approach could be considered, obtaining the same results for electrons 1 and 2. The sampling term at low η is the nominal 10 % increasing again with the upstream material. Note that, except for the low eta region, the sampling term gets slightly larger values than what it was presented in section 7.1. This is attibuted to the fact that a constant term in the resolution is not considered for these electrons coming from the Z decay. Note that the profiles obtained for samples generated with Pythia and AlpGen agree qualitatively. Small differences are shown in the E_{reco}/E_{true} and

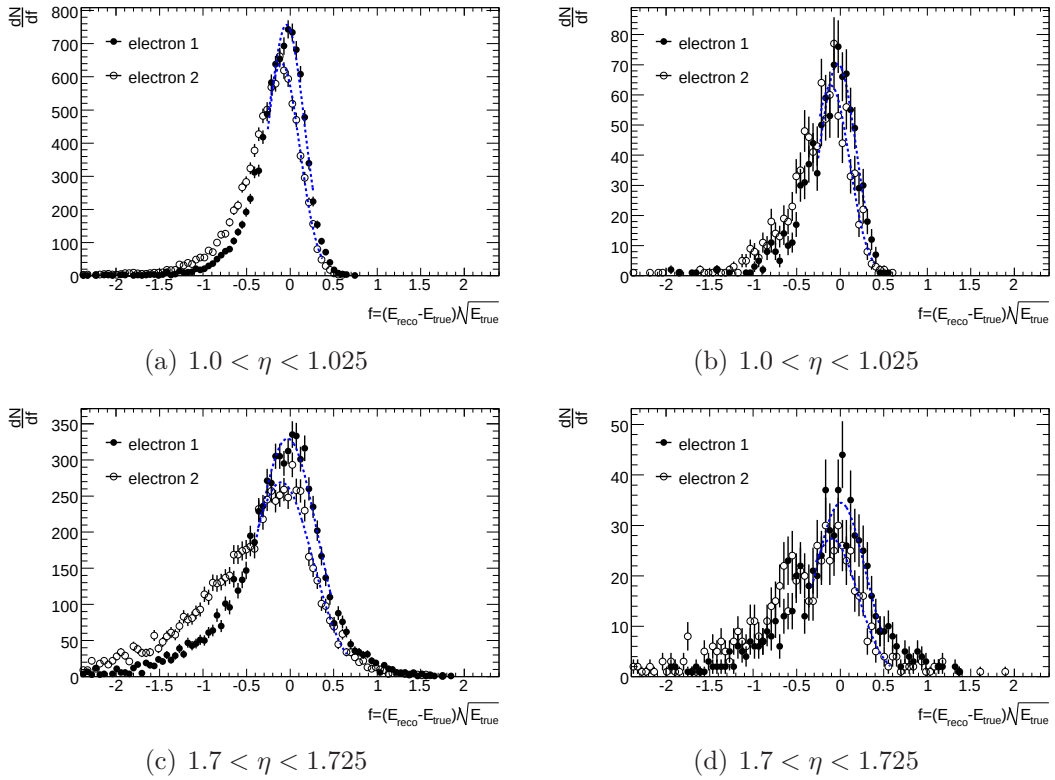

(a) $1.0 < \eta < 1.025$ (b) $1.0 < \eta < 1.025$

(c) $1.7 < \eta < 1.725$ (d) $1.7 < \eta < 1.725$

Figure 8.7: $(E_{reco} - E_{true})/\sqrt{(E_{true})}$ distribution in two different calorimeter cells for samples generated with Pythia (left) and Alpgen (right)

σ for electron 2 in the region $0.7 < |\eta| < 1.8$, which seems to be slightly better for the AlpGen sample, indicating a small difference in the final electron kinematics.

Once we have a resolution and energy scale map of the calorimeter we can define different regions depending on how far is the performance of the calorimeter from the ATLAS requirements. Hence, we define two regions that we will be denoted as *not ideal* and *ideal*. The former goes from $\eta = 0.7$ up to $\eta = 1.8$ (excluding $1.425 < \eta < 1.55$ since those cells are not calibrated using the CHM) and the latter covers the rest of the calorimeter with limit $|\eta| = 2.5$. The idea is to quantify the effect of an electron hitting in the *not ideal* part of the calorimeter on both the mass and width of the Z boson. In order to study this effect we have separated all the $Z \rightarrow ee$ events selected according to section 8.1 in three different sub-samples , namely: both electrons going to the ideal region (2 ideal), both electrons going to the not ideal region and one electron going to the ideal and the other to the not ideal region.

Figure 8.9 shows the invariant mass distributions of the two electrons for the three defined sub-samples. The distributions are normalized to the number of events in the sub-sample. The mass distribution is narrower and shows a less pronounced low mass tail in the case of two electrons going to ideal regions as expected. Each distribution is plotted separately in Figure 8.10 as well as the one will all events combined. The fit using the function of Equation 8.3 is also shown. It describes the

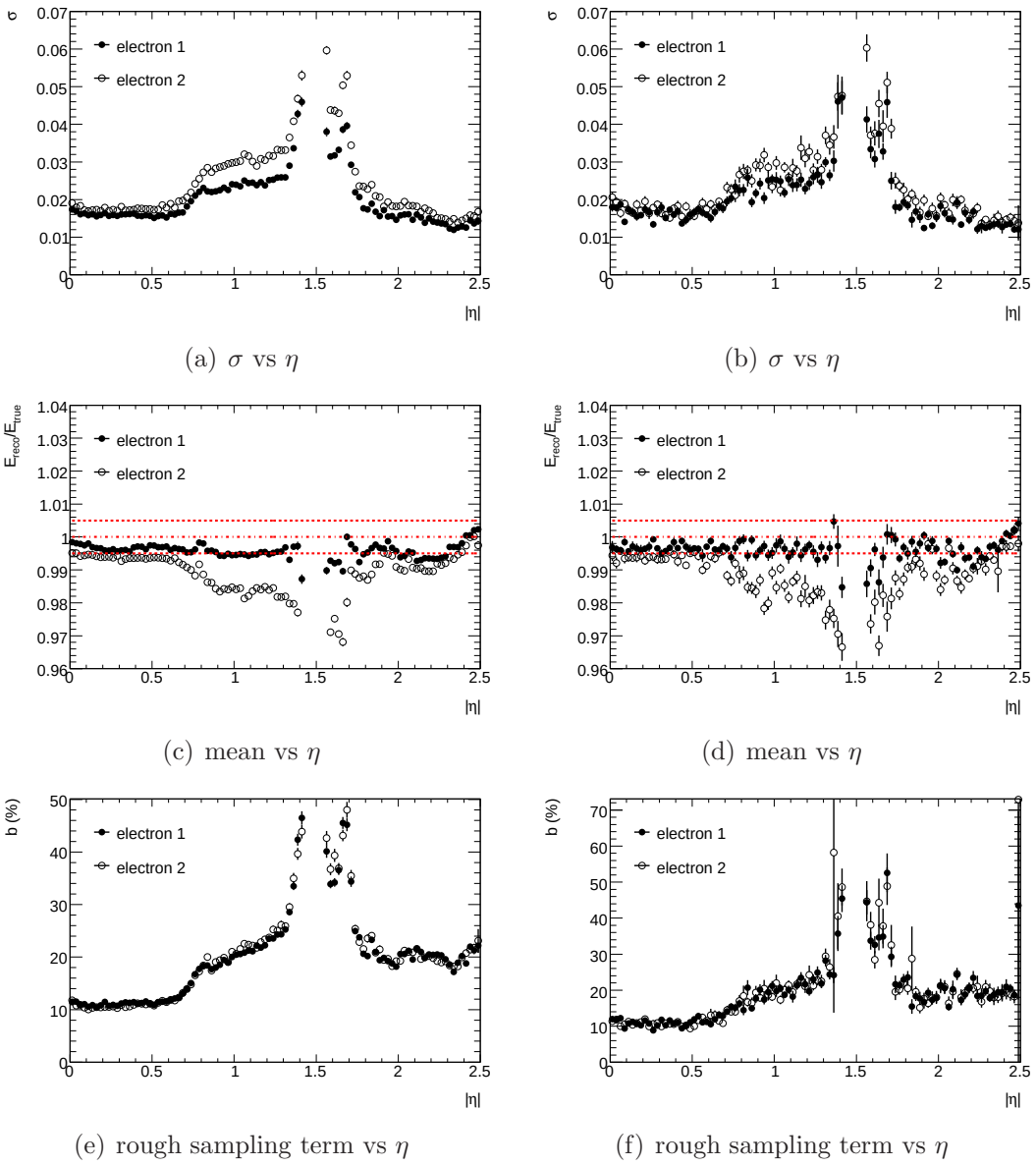

(a) σ vs η

(b) σ vs η

(c) mean vs η

(d) mean vs η

(e) rough sampling term vs η

(f) rough sampling term vs η

Figure 8.8: Energy scale and resolution map of the calorimeter

distributions well as indicated by the χ^2 values. The parameters of the eight fits are presented in tables 8.2 and 8.3 for the two samples Pythia and Alpgen respectively. Their values agree well within errors for the two samples.

In the most favorable case (2 ideal) the Z mass is understimated by 0.7%. This is attributed to the enegy lost in the upstream material by the QED final state radiation (see Section 8.5). We would like to recall that no radiation was considered in the Calibration Hits Method, where single isolated electrons were used. to obtaine the correction weights. The Z width is a bit overstimated, although the value lies at about two standard deviations of the nominal LEP measurement, hence it could still be a statistical fluctuation.

As the electrons enter the *not ideal* region the Z mass and width are affected

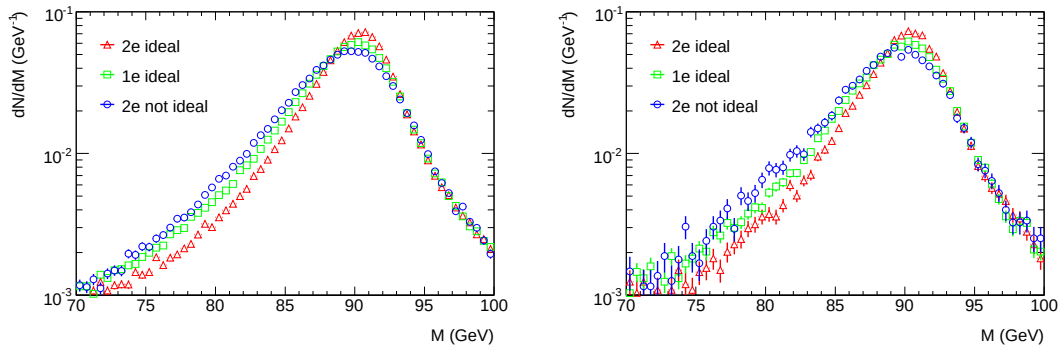

(a) Pythia (b) AlpGen

Figure 8.9: Zoom to the peak of the mass distribution for the different sub-samples and the combination.

P	All events	2 ideal	1 ideal	2 not ideal
Events	562127	189357	279178	93592
M_Z	90.364 ± 0.019	90.544 ± 0.029	90.225 ± 0.027	89.872 ± 0.049
Γ_Z	2.672 ± 0.024	2.565 ± 0.030	2.633 ± 0.037	2.717 ± 0.076
σ	1.421 ± 0.022	1.153 ± 0.008	1.592 ± 0.032	1.995 ± 0.059
n	12.756 ± 0.023	9.122 ± 1.702	16.353 ± 5.086	39.266 ± 59.156
α	0.675 ± 0.020	0.735 ± 0.095	0.703 ± 0.028	0.720 ± 0.049

Table 8.2: *Results of the fit to the mass distribution of the various sub-samples and the combination of all events to function PYTHIA*

P	All events	2 ideal	1 ideal	2 not ideal
Events	56836	19242	28085	9509
M_Z	90.371 ± 0.056	90.568 ± 0.080	90.243 ± 0.060	89.716 ± 0.117
Γ_Z	2.520 ± 0.076	2.475 ± 0.108	2.397 ± 0.126	2.570 ± 0.240
σ	1.513 ± 0.065	1.215 ± 0.096	1.724 ± 0.088	2.124 ± 0.156
n	15.693 ± 10.114	11.216 ± 7.964	126.369 ± 248.207	3.700 ± 2.420
α	0.684 ± 0.058	0.738 ± 0.110	0.690 ± 0.040	0.968 ± 0.192

Table 8.3: *Results of the fit to the mass distribution of the various sub-samples and the combination of all events to function ALPGEN*

significantly. The mass decreases by 1.0 % (1.4 %) with respect to the LEP measurement for the case one (two) of the electrons enter the *not ideal* region. The width of the distribution (Γ_Z) seems to be more sensitive than the global scale, increasing by a 5 % in the 1 ideal case and 8 % in the fully not ideal.

The parameters related with the detector resolution, σ, n and α, grow when proceeding from the ideal to the fully not ideal case reflecting the presence of extra upstream material.

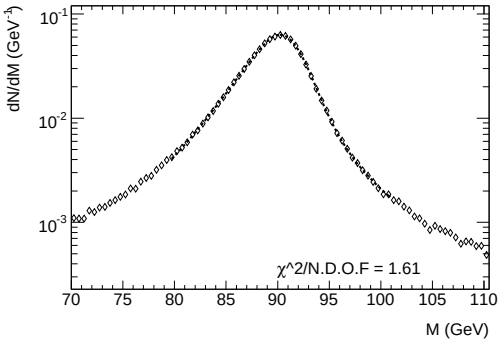

(a) All

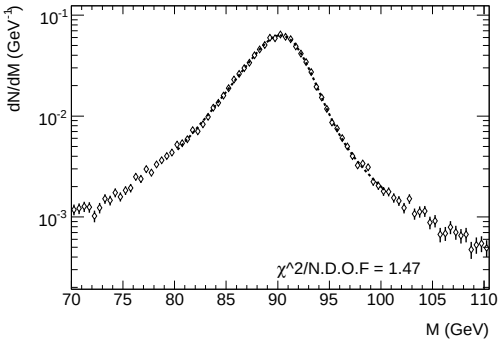

(b) All

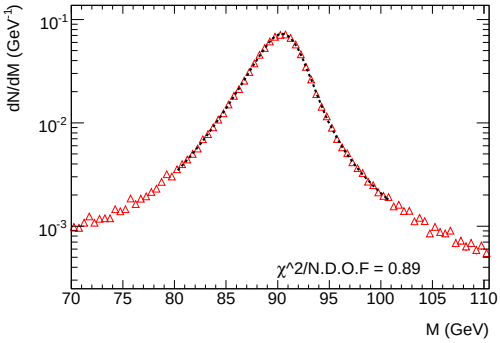

(c) 2 ideal

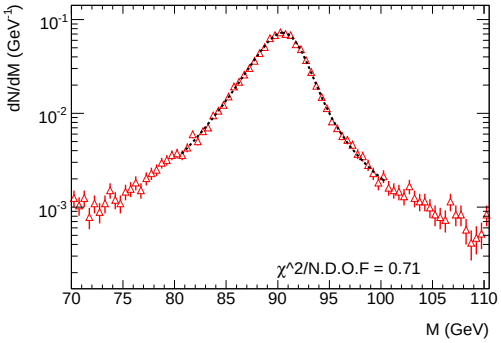

(d) 2 ideal

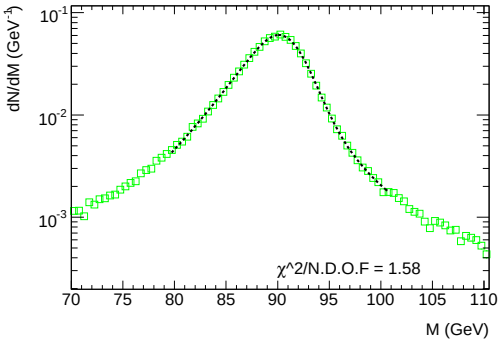

(e) 1 ideal

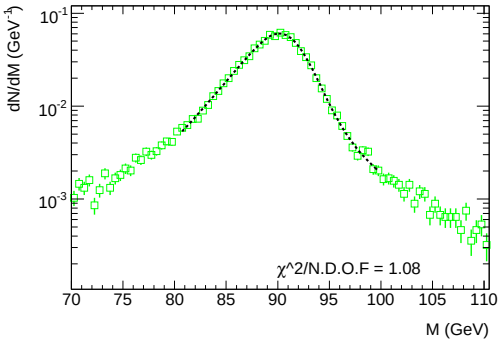

(f) 1 ideal

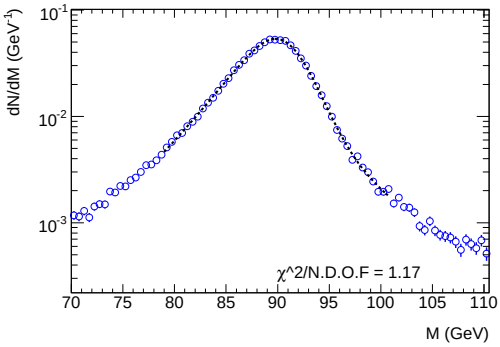

(g) 2 not ideal

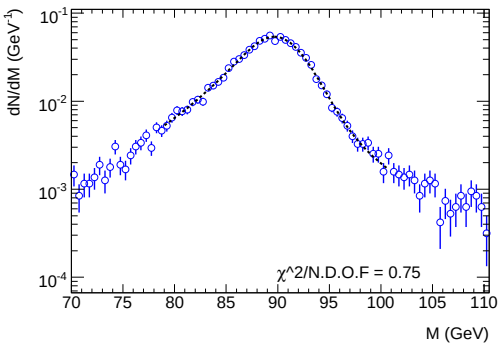

(h) 2 not ideal

Figure 8.10: Invariant mass distribution for events corresponding to the three defined sub-samples and all events. The left (right) row corresponds to events generated with Pythia (AlpGen)

8.4 Effect of tails

The presence of low energy tails in the reconstructed energy distributions was shown in Section 7.2, which indicates that the CHM cannot recover the lost energy totally, specially at the lowest energies. Events with a reconstructed energy below a certain threshold, $E_{reco} < E_{threshold}$, were considered part of the tail, where $E_{threshold} = \mu - 1.5\sigma$, being μ and σ the mean and standard deviation of the gaussian core of the distribution. In this section we try to quantify the effect of these events on the M_{ee} spectrum. With this purpose the electrons coming from Z decays will be divided in two categories, core and tail, depending on wether the fraction E_{reco}/E_{true} is higher (core) or lower (tail) than $E_{threshold}/E_{true}$. As discussed in the previous section an energy averaged approach is followed in this study. However, the two electrons coming from the Z are treated independently in order to account for the different average energy. Hence the values of μ and σ are different for electrons 1 and 2 (see Figure 8.8). Figure 8.11 shows the fraction of events in the tails for electron 1 and electron 2 as a function of η. It is about 20% and 25% for electrons 1 and 2 respectively, which represents a sample of enough statistics for the present study.

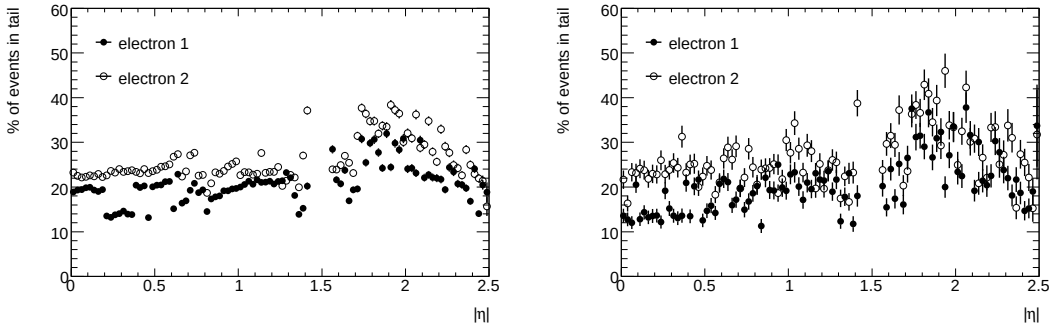

(a) Pythia (b) AlpGen

Figure 8.11: *Percentage of event in tail vs* $|\eta|$

Events are divided in three different sub-samples, namely: two electrons belonging to the gaussian core (core-core), one electron belonging to the gaussian core (core-tail) and two electron belonging to the tails (tail-tail). The corresponding mass distributions are shown in figure 8.12. By construction the effect of tails is larger than the effect of region discussed in previous section, since it reflects the worse situation in the CHM method. The Z peaks shifts to lower values as we include more electrons in the low energy tail. Figure 8.13 shows the individual mass distribution with the corresponding fits using the function of Equation 8.3. The distribution with all events combined is also plotted.

The randomness of the distribution is partially compromised by the selection criteria. However, it is possible to compared the degradation of the Z mass, taken the case "core-core" as the reference value. The degradation of M_Z in the case "core-tail" is about -2.5% while in the case "tail-tail" reaches -5.5%. This result does not depend on the Monte Carlo generator, Pythia or Alpgen.

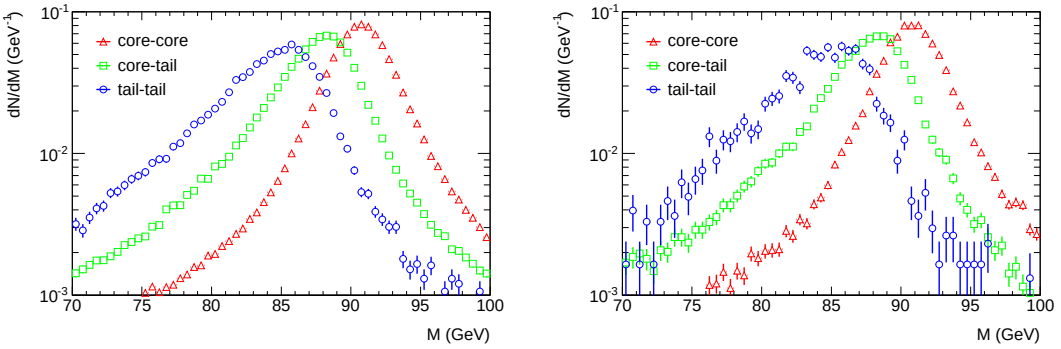

(a) Pythia (b) AlpGen

Figure 8.12: Mass distributions for the core-core, core-tail and tail-tail samples compared with the total sample

8.5 Final state radiation.

In this section we try to prove that the underestimation observed on the Z boson mass is not a failure of the CHM, which was proved to work within the ATLAS requirements for the energies involved in this process, but mainly a consequence of the final state radiation. The decay products of the Z boson are simulated to radiate via PHOTOS producing a "cascade" of electrons and photons, some of them of very low energy and very unlikely to reach the calorimeter. Thus some underestimation of the energy of the original electron is expected.

In the Z rest frame, the radiated photon emission show a collinear and infrared divergence feature. Hence, most of the radiated photons are expected to be of low energy. However, when moving to the laboratory frame the photon spectrum depends strongly on the direction of the original electron. In order to quantify the effect of this dependence we assume that the final photons of the cascade will not reach the calorimeter if their energy is lower than a certain threshold E_{thres}. The value of this threshold is chosen in accordance with the amount of material in front of the calorimeter. It can be extrapolated, for photons [3] , from equation 6.12 setting $E_{calo} = 0$. In a region with $\sim 3X_0$ of upstream material $E_{thres} = 100\ MeV$, while in the case $\sim 5X_0$ we have $E_{thres} = 300\ MeV$. A new threshod for electrons in the cascade is chosen to be $E^{ele}_{thres} = 9/7 \cdot E_{thres} + 600MeV$ where the factor 9/7 tries to account for the difference on the mean free path (see chapter 4) and the 600 MeV offset accounts for the effect of the magnetic field: a 600 MeV electron misses the calorimeter cluster due to its bend in the magnetic field.

The visible energy in the calorimeter E_{vis} is estimated to be the sum of the energies of the final particles of the cascade above the defined thresholds. As an example, figure 8.14 shows the fraction E_{vis}/E_{true}, where E_{true} is the energy of the original electron and $E_{thres} = 200MeV$, for events generated with Pythia (left) and AlpGen (right). The distributions show a peak at around 1 and a tail for lower

[3] In principle the extrapolation for electrons is not valid due to the effect of the magnetic field on very low energy electrons

values. Events in the low energy tail will distort the Breig-Wigner nature of the final mass distribution whereas the peak will produce deviations in the central value.

In order to compute how the Most Probable Value (MPV) of the distribution is affected by radiation as a function of pseudorapitiy, an average around the bin (b_{max}) with max number of entries is performed, using the following bins: $b_{max} \pm \delta b$, where δb is the number of bins, with at least one entry, on the right of b_{max}. Figure 8.15 shows the dependence of the averaged E_{vis}/E_{true} as a function of η for three different values of E_{thres} : 100, 200 and 300 MeV. The behaviour qualitatively agrees with figures 8.8 c and d with a general shift of the energy for electron 1. For electron 2 there is a roughly constant shift for $\eta < 0.7$ and $\eta > 1.9$, however a more pronounced shift with a sharp transition in the region $0.7 < \eta < 1.9$.

Finally, figure 8.16 shows the mass distributions computed using E_{vis} and assuming that the original electron does not change its direction after radiation, which is a valid approximation in most cases. The distributions become less symmetric as we increase the value of E_{thres} and the maximum is shifted towards lower values. Since the average upstream material in region $0.7 < \eta < 1.9$ is about $5X_0$, the threshold of $E_{thres} = 300MeV$ corresponds to such region. The value of the Z mass for this threshold is 90.1 which compares relatively well with the case *not ideal* of Table 8.2. Similarly, the material in front of the calorimeter in the region $\eta < 0.7$, $\eta > 1.9$ is on average about $3X_0$, which corresponds to $E_{thres} = 100MeV$. A fit of the Z mass to the distribution corresponding to this threshold gives $M_Z \sim 90.6$ in good agreement with the 2*ideal* case of Table 8.2, considering the assumptions of the present toy model for the radiation lost.

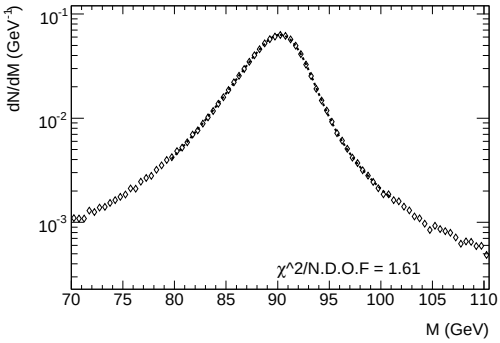

(a) All

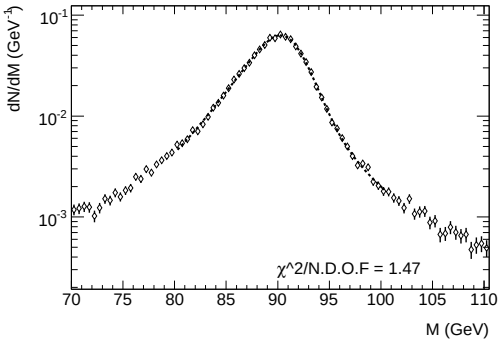

(b) All

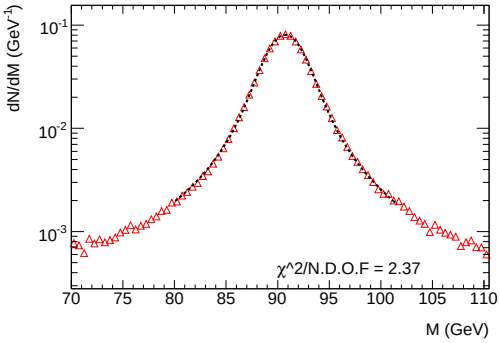

(c) core-core

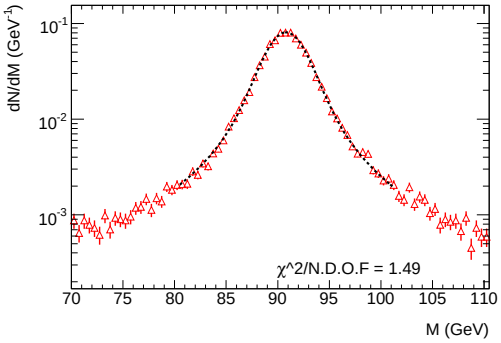

(d) core-core

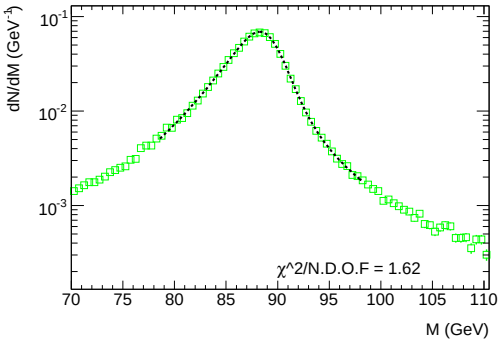

(e) core-tail

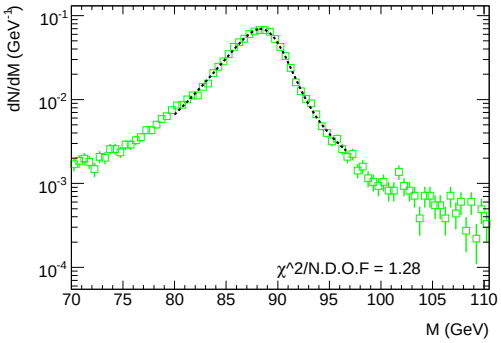

(f) core-tail

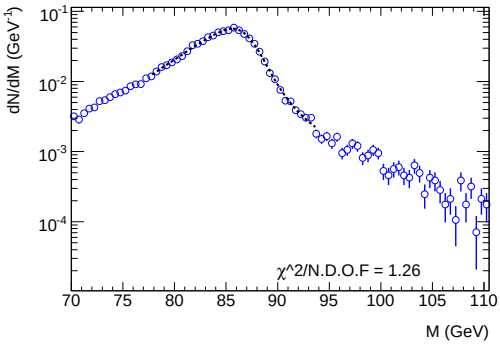

(g) tail-tail

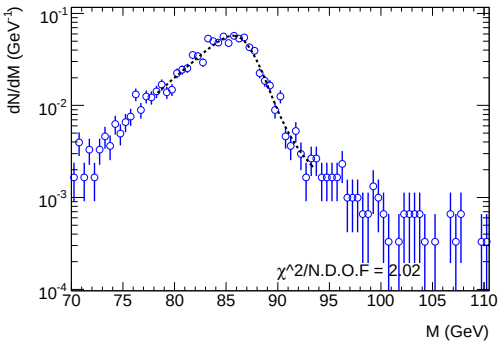

(h) tail-tail

Figure 8.13: Invariant mass distribution for events corresponding to the three defined sub-samples and all events. The left (right) row corresponds to events generated with Pythia (AlpGen)

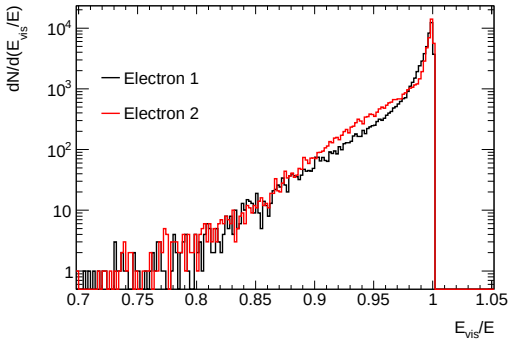

(a) $0.3 < \eta < 0.4$

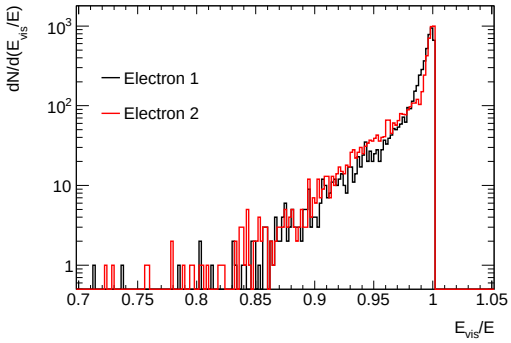

(b) $0.3 < \eta < 0.4$

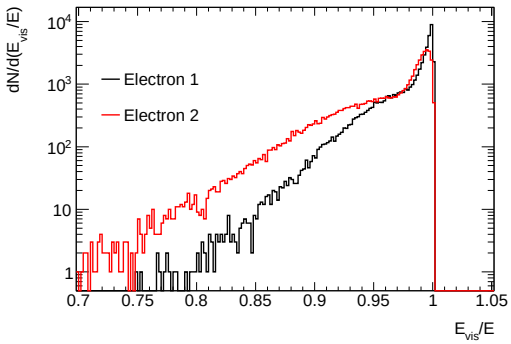

(c) $1.1 < \eta < 1.2$

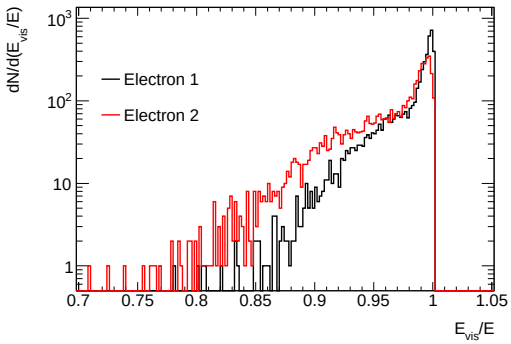

(d) $1.1 < \eta < 1.2$

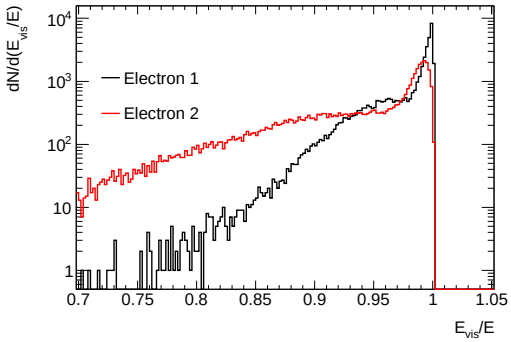

(e) $1.5 < \eta < 1.6$

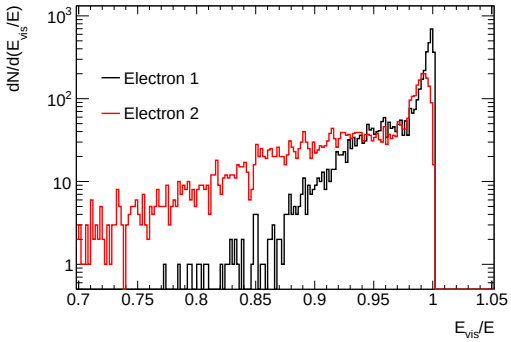

(f) $1.5 < \eta < 1.6$

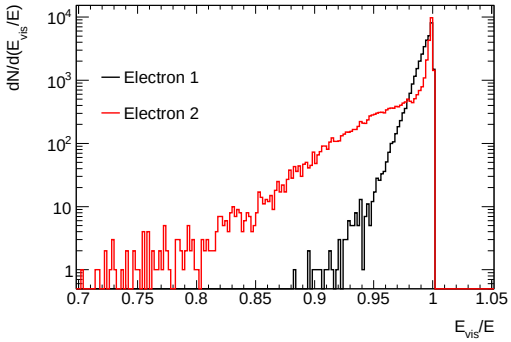

(g) $2.1 < \eta < 2.2$

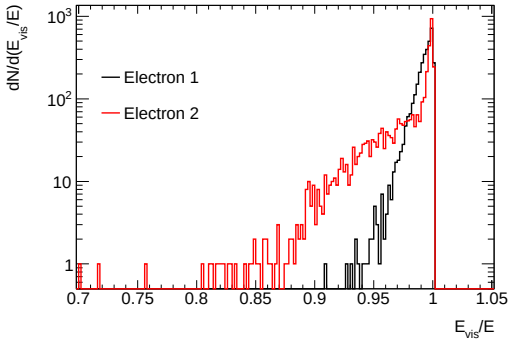

(h) $2.1 < \eta < 2.2$

Figure 8.14: E_{vis}/E distribution for $E_{thres} = 200MeV$ in four different η intervals.The left (right) row corresponds to events generated with Pythia (AlpGen)

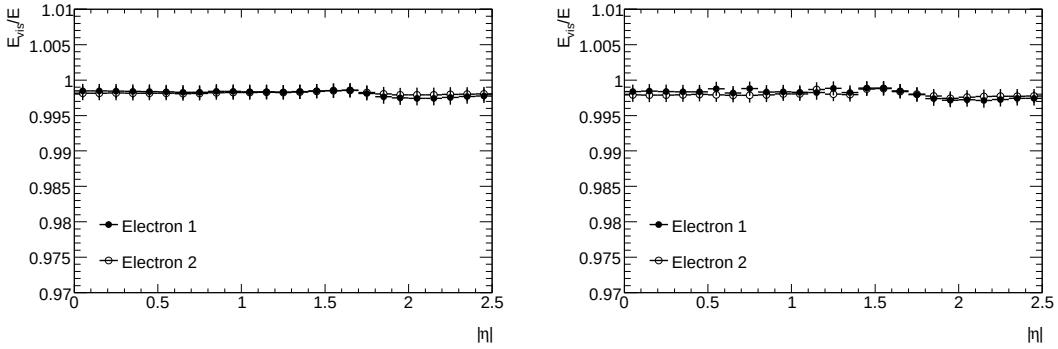

(a) $E_{thresh} = 100MeV$ (b) $E_{thresh} = 100MeV$

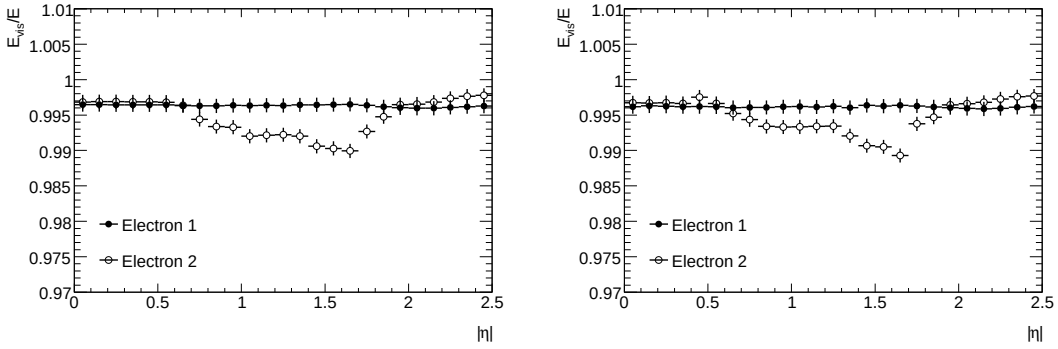

(c) $E_{thresh} = 200MeV$ (d) $E_{thresh} = 200MeV$

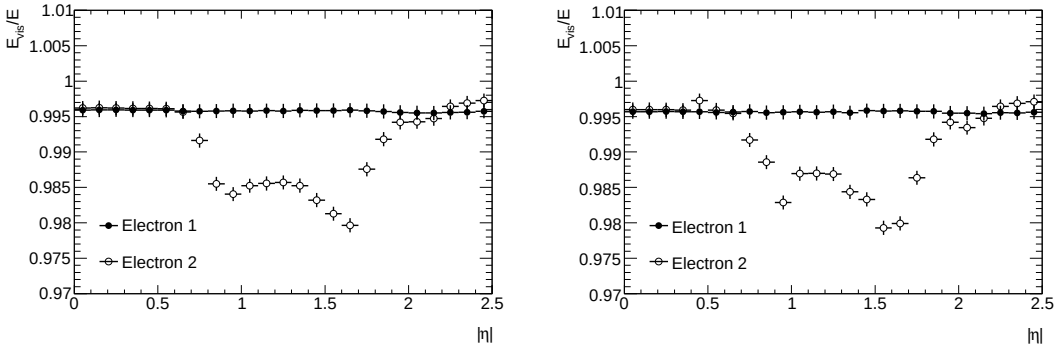

(e) $E_{thresh} = 300MeV$ (f) $E_{thresh} = 300MeV$

Figure 8.15: Average E_{vis}/E vs η for three different values of E_{thres}. The left (right) column correspond to even generater with Pythia (AlpGen)

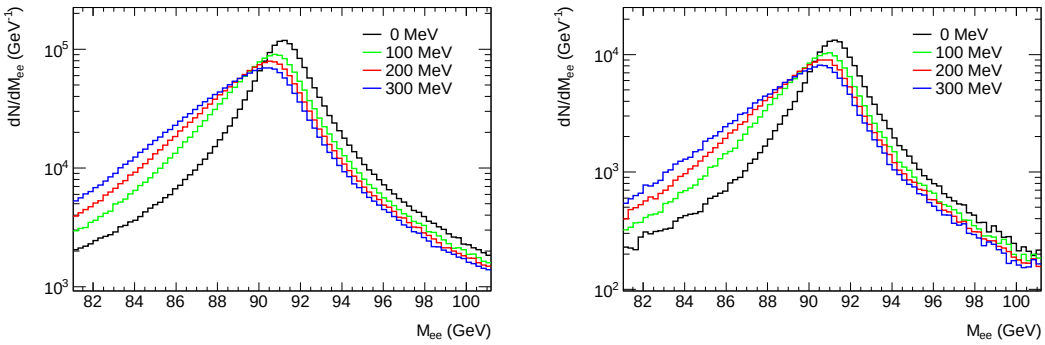

(a) Pythia (b) AlpGen

Figure 8.16: Invariant mass of the dielectron system computed with E_{vis} estimated with various E_{thres}. The left (right) plotcorrespond to even generater with Pythia (AlpGen)

Chapter 9

Conclusions

A new method to reconstruct the energy of electrons and photons, called Calibration Hits Method (CHM), applied sometime ago to the ATLAS Electromagnetic Barrel Calorimeter, has been adapted and tested with the Electromagnetic End-Cap Calorimeter. Some further developments to the method had to be done due to some peculiarities of the EMEC not present in the Barrel. The CHM corrects for the energy losses in material in front of the calorimeter as well as leakage, both transverse out of cell cluster definition and longitudinal behind the calorimeter.

To obtain these energy losses a special Monte Carlo simulation of the ATLAS response to single electrons and photons has been used, where the particles are produced at the nominal interaction point with 7 different energies ranging from 25 GeV to 1 TeV. The simulation included the nominal ATLAS geometry, taking into account the effect of the magnetic field as well as the vertex spread at the interaction point.

The 17 parameters of the CHM are obtained as functions of measurable quantities, namely: the energy in presampler, front, middle and back calorimeter compartments and the pseudorapidity (η) of the particle impact point. Corrections are applied at the cell cluster level, i.e. to the cluster energy, where several cluster sizes have been studied.

The energy reconstructed using the CHM method is checked in terms of linearity and energy resolution. Two clearly different regions have been found. In the most ideal case for $\eta > 1.8$ the deviation from linearity is better than 0.5% for electrons and unconverted photons but reaches up to 2 % for unconverted photons (more complicated parametrization not adopted at the very beginning of data taking have shown to substantially improve this result) at very low energies (25 GeV). The energy resolution is constant in this area with a sampling term of $\sim$ 10% for unconverted photons and $\sim$ 16% for both electrons and converted photons. The region $|\eta| < 1.8$ is mostly dominated by the presence of a large amount of upstream material. The resolution reaches values of up to $\sim$ 40% and the energy scale can reach 3% for both electrons and converted photon. Unconverted photons are closer to the ATLAS nominal requirements since they are not affected by the presence of dead material. Note that even though both resolution and energy scale are large, the CHM improves the former by a factor which is 10-30% i for the energy scale and a factor 2-7 in the

resolution for 100GeV particles.

Finally the CHM has been applied to samples of $pp \to Z \to e^- e^+$. If the CHM is not applied the mass distribution of the di-electron system is shifted by 6% with a shape dominated by a very large resolution. After correction, the Z Mass and Width differ from the nominal values due to radiation QED in the final state, which was not considered in the extraction of the CHM coefficients. The Z width was found to be very sensitive to the performance of the calorimeter increasing by a factor up to 7% (w.r.t the nominal value) if the electrons are reconstructed in the not ideal region of the calorimeter. The mass being less sensitive is underestimated by 1.2% in the same conditions. The effect of the tails on the reconstructed energy was also studied. The effect on the Z mass was estimated to be of -2.5% is one electron was found to be on the tail and -5% if both were reconstructed on the tail.

Conclusiones

Un nuevo método para la reconstrucción de la energía de electrones y fotones, aplicado originalmente a la parte Barrel del calorímetro electromagnético de ATLAS (EMB), ha sido adaptado y testeado en el EMEC. Nuevos procedimientos han sido desarrollados debido a las peculiaridades del EMEC respecto al EMB. Dicho método, conocido como *Calibration Hits*, corrige de una forma modular por las pérdidas de energía proporcionando información de la energía depositada en el propio calorímetro asi como delante y detrás del mismo.

Para la determinación de dichas pérdidas se ha empleado una simulación Monte Carlo especial de la respuesta del detector ATLAS a electrones y fotones aislados provenientes del punto de interacción con 7 energías diferentes, variando desde 25 GeV hasta 1 TeV. La simulación incluye la geometría nominal de ATLAS y tiene en cuenta tanto el efecto del campo magnético como las fluctuaciones (en la dirección z) del punto de origen de la partícula incidente respecto al punto de interacción.

Los 17 parámetros del método de Calibration Hits son obtenidos como función de cantidades medibles, a saber: la energía en presampler, front, middle y back y la pseudo-rapidez η. Las correcciones son aplicadas sobre la energía depositada en el cluster habiéndose estudiado varios tamaños.

La respuesta del método se ha estudiado en términos de linearidad, resolución y escala de energía. Se han encontrado dos regiones bien diferenciadas. En el caso mas ideal, $|\eta| < 1.8$, la linearidad está por debajo de 0.5 % para electrones y fotones no convertidos pero alcanza hasta el 2 % para fotones convertidos de baja energía (parametrizaciones mas complejas en función del radio de conversión mejoran este resultado pero no se han adoptado para el inicio de toma de datos). La resolución es constante en esta zona con un término estocástico de $\sim$ 10% para fotones no convertidos y $\sim$ 16% para electrones y fotones convertidos. El funcionamiento del método en la zona $|\eta| < 1.8$ está totalmente dominado por la presencia de de material muerto delante del calorímetro. En este caso el término estocástico de la resolución alcanza un $\sim$ 40% y la escala de energía un 3 % para electrones y fotones convertidos. El funcionamiento para fotones no convertidos es notablemente mejor debido a que estos no se ven tan afectados por la presencia de material. En este caso la resolución es mejor que $\sim$ 20% y la escala energía esta dentro del 0.5 %. Notar que, a pesar de los altos valores obtenidos en esta zona del calorímetro, la escala de energía mejora un 10-30 % y la resolución un factor 2-7 tras la aplicación del método de reconstrucción sobre partículas de 100 GeV.

Finalmente, el método de reconstrucción ha sido aplicado a muestras simuladas de

producción de Zs desintegrandose en pares electrón-positrón. Antes de la aplicación del método Calibration Hits la masa del Z está subestimada un 6 % y el espectro de masa invariante del sistema electrón-positrón ha perdido su naturaleza Breit-Wigner para estar dominado por la resolución del detector. Tras correcciones, las diferencias observadas en la masa y anchura del Z respecto a sus valores nominales se atribulyen a la radiación QED en el estado final (efecto no considerado en la extracción de los pesos Calibration Hits). Se ha encontrado que la anchura del Z (Γ_Z) es muy sensible a la respuesta del calorímetro, pudiendo variar hasta un 7 % (respecto de su valor nominal) si ambos producto de la desintegración son reconstruidos en zonas no ideales del calorímetro ($0.7 < |\eta| < 1.8$). El valor de la masa, siendo menos sensible, es subestimada alrededor de un 1.2 % en un caso de dos electrones no ideales.

El efecto de las colas en las distribuciones de energía tambien ha sido estudiado en muestras con Zs. Sucesos en los que ambos productos de desintegracion del Z han sido reconstruidos con energíias en la cola de la distribución producen una masa subestimada alrededor de un 5 %. Dicho valor disminuye a un 2.5 % en el caso de que solo uno de los productos de desintegración presente un a energía en la cola de la distribución.

Apendix A

in this apendix we try to summarize the $isEM$ flags used in order to identify electrons and photons (different for each type of particle). Such flags are determined in a cut-based procedure over a certain set of variables (information of tracks and shower shape variables). The thresholds for the input variables are independently obtained in (η, p_T) bins in order to maximize both the background rejection and the identification efficiency.

Electrons

A particle is identified as an electron [50] when an electromagnetic tower with transverse energy $E_T > 3GeV$, as defined in section 6.2, is matched to a track, that extrapolated to the calorimeter is within $\Delta\eta \times \Delta\phi = 0.05 \times 0.10$. The ration E/p is required to be lower than 10. Now there are three type of $IsEm$ flags depending on the required identification efficiency and background rejection, namely:

- Loose. Only information from the calorimeter is used such as hadronic leakage (ration between transverse in the first compartment of the hadronic calorimeter and EM transverse energy in a window of $\Delta\eta \times \Delta\phi = 0.24 \times 0.24$) and shower shape variables computed only using the middle layer of the calorimeter, namely: E_{237}/E_{277} (with $E_{2N_\eta N_\phi}$ the energy deposited in the middle layer in a window of $N_\eta \times N_\phi$ cells), E_{233}/E_{237} and $w_2 = \sqrt{\left(\frac{\sum_c E_c \times \eta_c^2}{\sum_c E_c}\right) + \left(\frac{\sum_c E_c \times \eta_c^2}{\sum_c E_c}\right)^2}$ (with E_c the cell energy deposit and η_c the cell η position) which is the shower width in units of η.

- Medium. Includes some tracking information and shower shape variables computed using the front layer of the calorimeter.

  - Shower shapes. In a window of $\Delta\eta \times \Delta\phi = 0.125 \times 0.2$ around the cell with maximum energy a second maximum is search. If found the variable, $\Delta E_s = E_{2max} - E_{min}$ is computed, with E_{2max} the energy of the second maximum and E_{min} the minimum energy found between the two maxima. Other variables are $R_{max2} = 1/(1+9\cdot 10^{-3} \cot E_T)$; w_{stot}, the shower width covering 2.5 cells of the middle layer; w_{s3} shower width in three front cells around the one with maximum energy and F_{side}, the fraction of energy deposited outside of the central layer.

  - Tack variables. Number of hits in pixels, silicon (pixels and SCT) and transverse impact parameter.

- Tight. In this case extra cuts are applied in the number of vertexing layer hits, number of hits in the TRT, ration of high-threshold hits to the number of hits in the TRT. Difference between cluster and extrapolated track η and ϕ and and ration of cluster energy to track momentum.

Photons

In order to identify photons [51] cuts are optimized in terms of the following variables:

- Hadronic leakage.
- Variables using the second compartment of the calorimeter E_{237}/E_{277}, E_{233}/E_{237} and w_2.
- Variables using the first compartment of the calorimeter: ΔE_s, R_{max2}, w_{s3}, w_{stot}, and F_{side}.
- Tack Isolation defined as the sum of the p_T of all tracks with $p_T > 1GeV$ within $\Delta R < 0.3$ (distance between the track at the vertex and the cluster center). In order to not include photon conversions, if $\Delta R < 0.1$ the impact parameter respect to the beam line must be less than 0.1 mm.

Bibliography

[1] W. N Cottingham and D. A. Greenwood *An introduction to the Standard Model of particle physics* Cambridge Univ. Press, 2nd edition, 2007.

[2] S. Weinberg *A model of Leptons* Phys. Rev. Lett., 19:1264-1266, 1967.

[3] A. Salam *Weak and electromagnetic interactions.* Proceedings of The Nobel Symposium Held at Lerum, Sweden, pages 367-377, 1968

[4] S.L. Glashow *Partial symmetries of weak interaction* Nucl. Phys 22:579-588, 1961.

[5] C. Amsler et al. *Review of particle physics.* Phys. Lett B667:1, 2008.

[6] *Massive leptonic pair production in hadron-hadron collisions at high energies*; S.D. Drell and T-M Yan Phys. Rev. Lett., 25:316-230, 1970.

[7] M. Flowerdew *standard Model Z/γ to ee production in early data at ATLAS* ATLAS Thesis. CERN-THESIS-2009-134

[8] http://lhc.web.cern.ch/lhc

[9] L Evans P. Bryant *LHC machine* JINST, 3:S08001, 2008.

[10] R. Adolphi et al. *The CMS Experiment at the LHC* JINST, 3:S08004, 2008.

[11] A. Alves et al. *The LHCb Experiment at the LHC* JINST, 3:S08005, 2008.

[12] K. Aamodt et al. *The ALICE Experiment at the LHC* JINST, 3:S08002, 2008.

[13] O. Adiani et al. *The LHCf Experiment at the LHC* JINST, 3:S08006, 2008.

[14] O. Anellii et al. *The LHCf Experiment at the LHC* JINST, 3:S08007, 2008.

[15] G. Aad et al. *The ATLAS Experiment at the LHC* JINST, 3:S08003, 2008.

[16] Liquid Argon Calorimeter TDR, CERN/LHCC/96-41

[17] Particle Data Group. *http://pdg.web.cern.ch/*

[18] W. R. Leo. *Techniques for Nuclear and particle physics experiments.* Springer-Verlag 1987

[19] R. Wigmans. *Calorimetry. Energy measurement in Particle Physics.* Clarendon Press Oxford 2000.

[20] U. Amaldi, *"Fluctuations in Calorimetry Measurements", Physica Scripta*, Vol. 23 pp.409-424 (1981).

[21] C. Fabjan, *"Experimental techniques in High Energy Physics"*. CERN, Geneva, 1985. CERN-EP/85-84.

[22] *Fast Simulation of Electromagnetic Showers in the ZEUS Calorimeter*; J. del Peso, E. Ros; Nucl.Instrum.Meth.A306:485-499,1991

[23] L. Landau, J. Phys. USSR 8, 201 (1944).

[24] *On the Energy Resolution of Electromagnetic Sampling Calorimeters*; J. del Peso, E. Ros; Nucl.Instrum.Meth.A276:456,1989

[25] C. Fabjan, *"Calorimetry in High Energy Physics"*, *Techniques and Concepts of High Energy Physics-III, T. Ferbel, ed. Plenum Pub. Corp.*, 1985.

[26] B. Aubert et al.; *Performance of the ATLAS electromagnetic calorimeter end-cap module 0;* Nucl.Inst.Meth. A500(2003)178.

[27] F. Hubaut, C. Serfon *Response Uniformity of the Atlas electromagnetic endcap calorimeter* atlas-larg-pub-2004-015

[28] C. Oliver, J. del Peso *Outer Wheel Uniformity of the ElectroMagnetic Endcap Calorimeter* atlas-larg-pub-2005-002

[29] M. Aharrouche et al. *Energy linearity and Resolution of the ATLAS Electromagnetic Barrel Calorimeter in an electron Test-Beam.* NIM A, 568:601-623, 2006.

[30] Graziani. G et al. *Linearity of the response to test beam electrons for EM Barrel module P13.* atl-larg-com-2004-001, 2004.

[31] M. Aharrouche et al. *Response uniformity of the ATLAS Liquid Argon calorimeter.* NIM A, 582:429-455, 2007.

[32] D. Banfi, L. Carminati, L. Mandelli; *Calibration of the ATLAS electromagnetic calorimeter using calibration hits.* larg-pub-2007-012

[33] S. Agostinelli et al. *Geant 4. A simulation Toolkit* NIM A 506 (2003) 250-303

[34] J. del Peso, E. Nebot *Electron energy reconstruction for the EM Endcap Calorimeter using calibration hits.* atl-larg-int-2008-001

[35] W. Lampl et al. *Calorimeter Clustering Algorithms: Description and Performance.* atl-larg-pub-2008-0012

[36] G. Aad et al. *Expected Performance of the ATLAS Experiment: Detector, Trigger and Physics* cern-open-2008-020

[37] E. Nebot . *Electron Energy Reconstruction in the ATLAS Electromagnetic End-Cap Calorimeter using Calibration Hits.* Master of Advanced Studies Thesis, Dept of Theoretical Physics, "Universidad Autónoma de Madrid", 2008.

[38] F. Hubaut et al. *Study of material in front of the EMEC calorimeter with high p_T electron shower shapes and tracks.* ATL-PHYS-INT-2008-026

[39] D. Banfi et al. *The measurement of the energy of electrons and photons in the ATLAS electromagnetic calorimeter* ATLAS Internal Note. Work in progress.

[40] J. Colas, C. La Taille, R. Lafaye, N. Massol, P. Pralavorio, D. Sauvage, L. Serin *Crosstalk in the ATLAS Electromagnetic Calorimeter* atlas-larg-2004-004

[41] W. Verkerke, D. Kirkby *RooFit User Manual V2.07* Document Version 2.07.29, 11 January 2006

[42] R. Devenish and A. Cooper-Sarkar *Deep inelastic scattering* 2004 Oxford Univ. Press.

[43] The ALEPH, DELPHI, L3, OPAL, and SLD Collaborations. *Precision electroweak measurements on the Z resonance* Phys. Rept 427 (2006) 257

[44] W. Verkerke, D. Kirkby *RooFit User Manual V2.07* Document Version 2.07.29, 11 January 2006

[45] N. Makovec *In-Situ Calibration of the Electromagnetic Calorimeter using $Z \rightarrow ee$ Events.* ATL-COM-LARG-2008-008.pdf

[46] D. Banfi *Electron and photon energy reconstruction in the electromagnetic caolimeter of ATLAS* ATLAS Thesis. CERN-THESIS-2008-074

[47] T. Sjostrand et al. *PYTHIA 6.4 physics and manual* JEP 0605 (2006) 026

[48] L. Mangano et al. *ALPGEN, a generator for hard multiparton processes in hadron collisions* JHEP 06 (2003) 01

[49] P. Golonka et al. *PHOTOS Monte Carlo: A precision tool for QED corrections in Z and W decays* Eur. Phys. J. C. 45 (2006) 97

[50] M. Aharrouche et el. *Reconstruction and identification of electrons.* ATL-PHYS-PUB-2009-003.pdf

[51] M. Aharrouche et el. *Reconstruction and identification of photons.* ATL-PHYS-PUB-2009-004.pdf